Delft University of Technology

Monitoring Erosion using Terrestrial Laser Scanning

Ilse Nijensteen

TU Delft

Monitoring Erosion using Terrestrial Laser Scanning

Master Thesis

by

Ilse Nijensteen

Student number: 4536940
Thesis Committee: Dr. R.C. Lindenbergh
Dr. S.M. Alfieri
Dr. T.A. Bogaard
Institution: Delft University of Technology
Faculty: Civil Engineering and Geosciences
Project Duration: March 1, 2022 - December 7, 2022

Cover Image: Illustration by the author based on Google Satellite Imagery and own results

TU Delft

Preface

This thesis marks the end of my time as a student. The last 9 months I worked on this final part of obtaining the master degree in Geoscience and Remote Sensing. During the fieldwork course in June 2021, I worked with the terrestrial laser scanner for the first time. I did not have much prior knowledge, because I initially missed the course where this technique was introduced, but I was fascinated by the enormous possibilities with point clouds. When I found a thesis subject about monitoring erosion using terrestrial laser scanning, it immediately had my attention. Luckily, Roderik gave me the opportunity to pick this topic, despite my lacking knowledge at that time and he also offered the possibility to follow the surveying course during my first month of thesis work.

Of course, this thesis would not have been possible without the members of my committee. Therefore, I want to thank my supervisor Roderik. I really appreciate your positive and encouraging way of supervising by providing new perspectives and thinking along: most times I walked out your office with confidence to continue working on my thesis. Also, a great acknowledgement goes to Silvia, for your valuable contributions and suggestions during our meetings and always providing me with new information from the OPERANDUM project. Furthermore, I want to thank Thom for joining the committee as an external member and for providing some critical notes towards my work and new insights from a more hydrological point of view.

There are a few other people, who also deserve acknowledgements for helping me with my thesis. Thanks to my group members Sofie and Lina of the 3D surveying course for our group work, which gave me a kick start for my thesis. Thanks to Adriaan and Massimo for your time to discuss and help me to progress with my project. You provided some valuable insights. Thanks to the OLRS group for the group meetings which made me feel a bit part of a research group during my thesis. Marjolein, thank you for your proofreading and nitpicking to improve the final version of this thesis.

Furthermore, I am enormously grateful for the opportunity to organise a fieldwork trip to Catterline together with Marijn and Eefje, which turned out to be a really fun experience as well. Marijn helped me a great deal with carrying out the measurements with the Leica ScanStation P40.

Lastly, there are people whose presence in these last months was crucial for me. To those I hold close - my friends and family, thank you for being there and providing the so needed distractions during the past months! Huize Ballenzicht, thanks for all our exchanged words and your kindness. Yuran, thank you for your endless attempts to relieve the stress levels and listening to my weekly thesis struggles. Mama and papa, thank you for your unconditional support and for keeping me motivated and curious.

Ilse Nijensteen
Delft, November 2022

Abstract

The Catterline Bay, located in North East Scotland, is prone to erosion processes. Using Terrestrial Laser Scanning (TLS) two point clouds were obtained in 2019 and 2022 from this area of ca. 0.2 km^2. Here, a methodology was proposed and tested to assess how erosion processes can be monitored from high resolution point clouds in small study areas. Filtering of ground points from the point clouds was done using a full 3D approach. The local dimensionality on multiple scales was used to generate features for the classification, for which Linear Discriminant Analysis was used. The algorithm was able to precisely separate non ground points from ground points with a precision on test data sets of 94.7% on ground points and 94.3% on non-ground points.

The ground points provided a basis for the Digital Terrain Model (DTM) raster. Several geomorphological quantities could be derived from this DTM. Next to these quantities, also information about vegetation height and 3D change detection using the Multi-scale Model to Model Cloud Comparison (M3C2) was extracted.

From a combination of the Terrain Ruggedness Index (TRI), change detection using the Multiscale Model to Model Cloud Comparison (M3C2) technique and photos, erosion zones were derived. Also stable, non-erosion, zones were identified. Various statistics from the geomorphological quantities were analysed for both zone types. Erosion zones have clear edges of high TRI values, indicating the scarps of landslides. The erosion zones also contain groups of negative M3C2 distances, indicating depletion zones. Not only the TRI and M3C2 distances have significantly different statistics for erosion and non-erosion zones, also the slope is steeper in these zones and the Topographic Wetness Index is smaller. The mean slope for erosion zones is 39.3° compared to 30.9° for non-erosion zones. To capture the behaviour of the TRI in the defined zones, p_{TRI} was introduced which gives a rate of how many cells have a high TRI value in a defined zone. The p_{TRI}, the rate of TRI values above 0.06 m, is more than 4 times larger for erosion zones (0.17) than for non-erosion zones (0.04).

Changes in vegetation height could be linked to locations of implemented Nature Based Solutions (NBS). The results were in agreement with changes in NDVI, which were calculated from optical satellite imagery.

In conclusion, the new methodology has great potential to identify erosion zones in complex sloped terrain and monitor changes in vegetation.

Contents

Nomenclature

The next list describes several symbols that are used within the body of the document

ALS	Airborne Laser Scanning
ba	balanced accuracy
CANUPO	CAractérisation de NUages de POints
CSF	Cloth Simulation Filter
DTM	Digital Terrain Model
fdr	Fisher Discriminant Ratio
HMH	Hydrometeorological Hazard
HMR	Hydrometeorological Risk
ICP	Iterative Closest Point
InSAR	Interferometric Synthetic-Aperture Radar
LDA	Linear Discriminant Analysis
LiDAR	Light Detection And Ranging
LoD	Level of Detection
M3C2	Multiscale Model to Model Cloud Comparison
MHC	multi-resolution hierarchical classification method
NBS	Nature Based Solution
NDVI	Normalised Difference Vegetation Index
PC	Principal Component
PCA	Principal Component Analysis
RMSE	Root-Mean-Square Error
ToF	Time of Flight
TPS	Thin Plate Spline
TRI	Terrain Ruggedness Index
TWI	Topographic Wetness Index
UAV	Unmanned Aerial Vehicle
VBS	Voxel Beamlet Superposition

List of Figures

List of Tables

1 Introduction

A large part of the coastlines in Scotland is vulnerable to erosion and with the inevitable further climate change, coastal erosion could put many of Scotland's buildings and infrastructure at risk in near future (Dunkley et al., 2021). Due to climate change, the Scottish coast is not only subjected to sea level rise, but also to increased precipitation frequency and intensity. These expected increases will raise an increased likelihood of landslides. Buildings on top of sea cliffs and close to areas subject to landslides and erosion pose a direct risk to lives and residential properties.

The Catterline Bay, located south of Stonehaven in Aberdeenshire on the north east coast of Scotland, is an area subject to landslides and erosion. At this bay, new techniques are implemented to counteract landslides and erosion. Traditionally, structural engineered built up measures were taken to manage the risks. These man-made structures are constructed using traditional building materials, such as concrete, steel or other long-lasting materials. The structural measures are expensive and lack long-term sustainability (Kumar et al., 2021). Over the last decades, the use of eco-engineered solutions was introduced as a more efficient, cost-effective and sustainable measure to mitigate risks. Vegetation was used to counteract landslides and erosion at the Catterline Bay, provided by their soil-root mechanical reinforcement (Gonzalez-Ollauri & Mickovski, 2016). To monitor the effectiveness of these measures against erosion and the landslide movement, different remote sensing techniques can be used. However, coastal cliffs have challenging geomorphological features for change detection methods, because they usually present a complex surface topography that is the result of numerous processes (erosion and deposition by wave action, mass movements and weathering). Additionally, these changes may happen in any direction, so 3D change detection methods have to be applied (Gómez-Gutiérrez & Gonçalves, 2020). Thus, a 3D data set is required. A terrestrial laser scanner is a platform capable to acquire this kind of data. This remote sensing technique uses Light Detection And Ranging (LiDAR) to create a 3D data set (a point cloud) of its surroundings.

1.1. Problem Definition and Approach

Knowledge about how to define and assess erosion indicators empowers science to reveal and monitor erosion prone zones. A fieldwork campaign with terrestrial laser scanning (TLS) can provide a point cloud (a 3D data set) of the study area, the Catterline Bay in Scotland. After intensive processing, products from the point cloud can be used to monitor the erosion processes. However, there does not yet exist a general accepted workflow to process the TLS data. This thesis proposes such a workflow, built up with already well-established methods. Furthermore, erosion and non-erosion zones are identified. Using these zones, distinctive properties of erosion zones are derived from geomorphological quantities. Lastly, the possibilities of monitoring the effect of nature based solutions using terrestrial laser scanning are explored.

1.2. Research Questions

From the various steps leading to assessment of the erosion patterns, the following research question is addressed:

> **How can terrestrial laser scanning be used to monitor erosion processes on a coastal slope?**

Five subquestions are defined as support to answer the main research question:

1. How to acquire a TLS data set in complex sloped terrain?
A field campaign with terrestrial laser scanning asks for good knowledge of the study area. This question studies how a terrestrial laser scanning fieldwork is conducted and what potential difficulties or limitations of the technique are.

2. How to identify static erosion characteristics from point cloud data?
In order to quantify erosion from TLS data, a basic understanding of erosion processes is needed. Furthermore, finding characteristics of erosion in the point cloud data allows for the identification of erosion zones.

3. How to acquire an accurate temporal change detection map of erosion?
Erosion can be quantified by looking at the development over time: if major changes are detected, then the rate of erosion at that zone is high. To detect changes in the geomorphology of the terrain and to quantify erosion rates, multiple data acquisitions are needed. This question seeks an answer to the question how these changes can be detected.

4. How to identify erosion zones and assess erosion patterns?
This question adresses how the characteristics from subquestion 2 and change detection from subquestion 3 can be used to identify erosion zones. The assessment of erosion patterns in the identified zones can help to develop an understanding of how erosion zones are characterised. If zones are developing patterns similar to those in erosion zones, zones can be detected as erosion zones in an early stage, so that measures can be taken.

5. How to compare results from terrestrial laser scanning data to other remote sensing techniques?
In this thesis, the use of specifically terrestrial laser scanning is researched as a tool to monitor erosion processes. However, there are multiple other remote sensing techniques, which are also able to monitor erosion to some extent. This question compares results from TLS data to results from other remote sensing techniques and examines the added value of the terrestrial laser scan data.

1.3. Outline

In Chapter 2, the mechanisms of erosion, eco-engineered solutions against erosion and the physics behind terrestrial laser scanning are described. Chapter 3 contains information about the structure, handling and processing of point clouds. Chapter 4 presents the workflow and details on the used methods such as filtering of ground points and change detection methods. Chapter 5 describes the study area, the used data sets and the process of data acquisition. The results are presented in Chapter 6 and then discussed in Chapter 7. A brief conclusion and recommendations on further steps are given in Chapter 8.

2

Monitoring Geomorphology

This chapter provides background information and theoretical knowledge related to the processes of landslides and erosion in Section 2.1, eco-engineered solutions to these phenomena in Section 2.2 and the monitoring of these geomorphological processes using notably terrestrial laser scanning in Section 2.3 and Section 2.3.1.

2.1. Erosion

Some fundamental understanding of forcings and characteristics of erosion will provide the necessary tools to develop a methodology for monitoring.

Erosion is defined as processes that loosen sediment and move it from one place to another on the surface (Kenneth Hamblin & Christiansen, 2004). Removal of rock or soil can be physical, chemical or mechanical. Agents of erosion include water, ice, wind and gravity (Kenneth Hamblin & Christiansen, 2004).

On slopes, the most common form of erosion is mass movement. Mass movement is the transfer of material downslope through the direct action of gravity, that 'pulls' materials to a lower gravitational potential (Kenneth Hamblin & Christiansen, 2004). Although mass movement is possible because of gravity on slope systems, there are always triggers or drivers needed that cause the mass movement. Types of mass movement are creep, debris flow and landslides. This study is focused mostly on landslides. A landslide involves movement along a well-defined slippage plane. A landslide moves as a unit along a definite fracture, with most of the material moving as a large slump block (Kenneth Hamblin & Christiansen, 2004), as illustrated in Figure 2.1. Landslides occur when the pore pressure in the soil skeleton results in a reduction of shear strength (Sidle & Bogaard, 2016). Landslides are separated in shallow and deep-seated types. This study focuses on shallow landslides which are less than 2 m deep.

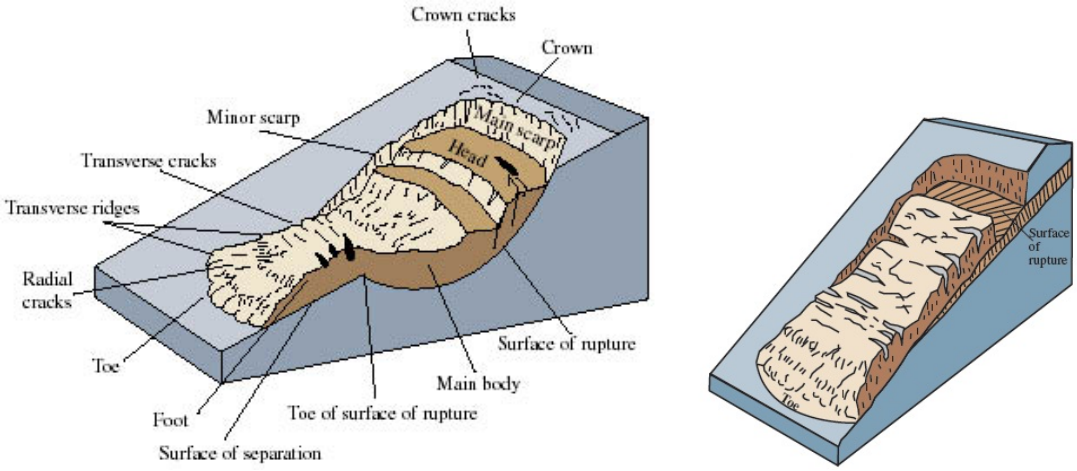

(a) An idealised rotational landslide showing commonly used names for labelling different parts.

(b) An idealised translational landslide

Figure 2.1: 2 types of landslides. Illustrations from Highland and Johnson (2004).

Two major types of landslides are rotational and translational landslides (Highland & Johnson, 2004). In a rotational landslide, the surface of rupture is curved concavely upward and the slide movement is more or less rotational about an axis that is parallel to the ground surface and transverse across the slide (Highland & Johnson, 2004). Figure 2.1**(a)** shows an idealised rotational landslide. For a translational landslide, shown in Figure 2.1**(b)**, the mass moves along an approximately planar surface with only little rotation or tilting. Figure 2.1**(a)** also indicates some characteristic features of landslides. At the upper side of the landslide, the crown shows the 'start' of the landslide and consists of undisplaced material. Another unique indicator of a landslide is a scarp: a steep surface on the undisturbed ground at the upper edge of a landslide, caused by movement of the displayed material away from the undisturbed ground. This is the visible part of the surface of rupture and helps to identify landslide prone zones (Kenneth Hamblin & Christiansen, 2004). The surface of rupture is surface which forms the lower boundary of the displaced material below the original ground surface (Cruden, 1993). Part of the displayed material in the lower part of the slump block may move more like a debris flow.

Landslides occur at many different scales and on small scale, they appear nearly everywhere. Also the time scale has a broad range: there are enormous slides occurring within a few seconds, but also slides gradually moving over a period of weeks or months (Kenneth Hamblin & Christiansen, 2004).

The most important driver causing mass movement is saturation of slope material with water, which leads to weakening of the soil shear strength. The reduction of shear strength is caused by the buoyancy force exerted by water in a saturated soil and soil suction in an unsaturated soil (Bogaard & Greco, 2016). Heavy rainfall, either a heavy single event or prolonged over multiple days, and also snowmelt results in the saturation of the slope material (Gonzalez-Ollauri & Mickovski, 2021). Other sources of water can be pipe leakage and drainage canals. Besides these triggers, slope failures can also be triggered by earthquakes, although their occurrence is much lower (Kenneth Hamblin & Christiansen, 2004; Sidle & Bogaard, 2016).

Vegetation influences the occurrence of landslide via various paths, which include root strength, evaporation, transpiration and root architecture (Sidle & Bogaard, 2016). Most of these factors are linked to the root distribution. When root systems are well developed, i.e. dense and deeply penetrated into the soil, they can affect shallow landslides as a slope stabilising agent (Sidle & Bogaard, 2016). Vegetation depletes soil water moisture and increases soil suction by transpiration and influences the overall hydrology by canopy and litter layer interception (Bogaard & Greco, 2016). Vegetation contributes to the development of pores that act as preferential flow paths, increasing the infiltration and drainage capacity and changing the hydraulic properties of the soil (Bogaard & Greco, 2016). The next section will present some interventions to prevent landslides using this positive influence of vegetation on slope stability.

2.2. Nature Based Solutions

The erosion and landslides as described in the previous section are a form of hydrometeorological hazards (HMHs). A HMH is the result of processes of hydrological, oceanographic or atmospheric origin that can cause socio-economic and environmental losses (Kumar et al., 2021). One branch of measures against these hydrometeorological risks (HMRs) are structural: built-up man-made structures, where traditional building materials, such as steel and concrete are used. Because of these hard structures, the measures are often called 'grey'. Dikes, storm sewers and floodgates are examples of these structural measures. Using hard structures hinders that an ecosystem can develop on the structure. Such structural measures are expensive and often lack long-term sustainability (Kumar et al., 2021).

The drawbacks of traditional measures are taken away by eco-engineered solutions. An example of an effective eco-engineering measure against shallow landslides and erosion is the use of plants, because of the interaction between the soil and roots of the plants. A soil with roots creates a composed material that has enhanced strength providing a similar effect to the soil like that of steel rods to reinforced concrete (Gonzalez-Ollauri & Mickovski, 2016). Eco-engineered solutions are summarised under the heading of Nature Based Solutions. A Nature Based Solution (NBS) is either green (vegetation based), blue (waterbody based) or hybrid (combining either green, blue and grey measures).

Some relevant implementations of NBS in this study are live pole drains, a live ground anchors, high density planting and live cribwalls. In Figure 2.2 an implementation of the live pole drain is shown. A live pole drain consists of cylindrical bundles made of live cuttings of trees such as willows with roots used as drain collectors against the underground seepage rising. The bundles of cuttings are placed in shallow trenches in such a manner that they intersect and collect the moisture (Polster, 2003).

(a) Live pole drains are used to stabilise slumping soils. Illustration from Polster (2003).

(b) Live pole drain implementation in Catterline. Picture taken by the author.

Figure 2.2: Live pole drains. Left: a schematic view. Right: a real life implementation at the Catterline Bay.

A live ground anchor consists of an anchored grid, which is supplemented with natural sustainable materials. The temporary structure supports the vegetation growth for a certain time period. This NBS immediately gives protection against erosion with an anchored grid, which is supplemented with natural sustainable materials.

A live cribwall is a wall built up of timber logs, locally available earth materials and plant cuttings. A live cribwall follows the same engineering principles as a concrete-based retention wall, but it uses natural, organic materials, that will decay over time, such that the wall becomes an element of the natural soil. In Figure 2.3 an example of a cribwall is displayed.

(a) Live ground anchors **(b)** Live cribwall

Figure 2.3: Two examples of Nature Based Solutions. Pictures taken by the author.

Downsides of many NBS are that their effect only becomes significant after quite a while and their implementation can be labour-intensive and thus making them costly. On the other hand, an NBS could need less maintenance and be more cost-effective over time.

The relative performance and efficiency of the NBS with respect to a grey solution is important to consider when choosing between different grey and nature based solutions. The performance of an NBS is assessed using various qualitative and quantitative indicators. Monitoring strategies and techniques for quantifying the effects of NBS depend on how the mitigation measure targets the landslide process. The effectiveness of an NBS designed against hydro-meteorologically driven landslides can be assessed by either monitoring the impacts of a landslide process (e.g. landslide displacement or topographic changes) or the direct effects of the NBS itself (e.g. soil reinforcement and hydrological effects). If derived time series show a trend of reduced landslide activity (e.g. decreasing displacements, lower number of landslides) after the implementation of an NBS, the NBS can be proven to be effective. To assess the movement of a landslide over time at specific points, various techniques are possible: either along profile lines or area-wide. Area-wide measurements usually rely on remote sensing techniques, including terrestrial laser scanning (TLS), airborne laser scanning (ALS), interferometric synthetic aperture radar (InSAR) and photogrammetric techniques (e.g. Structure for Motion).

2.3. Remote Sensing for Monitoring Erosion

In-situ measurements give information on soil reinforcement and hydro-mechanical effects of the vegetation on the sloped soil. Possible experiments are rainfall or scouring simulations. A downside of field experiments is that it lacks a good resolution of spatial information (Gao et al., 2021). This constrains accurate monitoring and understanding of erosion processes. Other drawbacks of these direct measurements is that they are invasive and time consuming.

Remote sensing techniques can complement these in-situ measurements to provide a more area-wide analysis of on-going erosion processes. A number of studies tried to monitor erosion using erosion pins (Barnes et al., 2016), tape measurement (Casalí et al., 2006; Zhu, 2012), total station (Myers et al., 2019), global navigation satellite system (GNSS) (Wu & Cheng, 2005), aerial photogrammetry (D'Oleire-Oltmanns et al., 2012), close-range photogrammetry (Gómez-Gutiérrez et al., 2014), interferometric synthetic aperture radar (Bayer et al., 2017; van Natijne et al., 2022; Yin et al., 2010), optical satellite imagery (King et al., 2005; Travelletti et al., 2012) and terrestrial laser scanning (TLS) (Gao et al., 2021; Longoni et al., 2016; Mukupa et al., 2017; Šašak et al., 2019). In contrast with photogrammetry and TLS, results from erosion pins, tape measurement, total station and GNSS are usually suffering from a low spatial resolution and are therefore unsuitable for a detailed analysis of erosion and change detection. Interferometric synthetic aperture radar (InSAR) is a radar technique, that allows for 3D deformation information using wave phase differences in radar waves and the spatial distance between two synthetic aperture radar images (Yong et al., 2022). A benefit of this technique is that data is obtained all day and is not affected by weather conditions. By continuously tracking deformations, trends

in erosion patterns can be analysed. However, manual calibration is needed and human interventions can cause misjudgement of results (Yong et al., 2022). Optical satellite images are also used to monitor erosion. A benefit is that the coverage is large, but this comes at the cost of low spatial resolution and it also is strongly affected by weather conditions. From the spectral bands of optical satellite images, information on soil surface, temporal changes of surface states, incision and the geometry of possible water pathways on the surface can be extracted (King et al., 2005). Photogrammetric and laser scanning data can either come from ground-based or unmanned aerial vehicle devices. The benefit of photogrammetry is that the equipment is relatively low budget and easy to use. Although, the quality of the results will be significantly lower compared to laser scanning results. The use of an unmanned aerial vehicle (UAV) in combination with laser scanning requires a larger investment in equipment and also more skills (i.e. drone flying) compared to a terrestrial laser scanning campaign. Furthermore, the accuracy depends stronger on the quality and calibration of the system's scanner, IMU and GNSS components. Also, repeatedly completing photogrammetry or LiDAR measurements (either with a drone or a terrestrial scanning station) on the topographic changes is more time-consuming than data from satellites (InSAR, optical imagery, GNSS), as multiple campaigns to the study area are needed. Lastly, a laser scanning campaign using ground based stations, terrestrial laser scanning (TLS), is an often used technique to monitor erosion processes. A vast advantage of TLS compared to other remote sensing techniques is that it is able to acquire very high spatial resolution data with high precision and accuracy (Yong et al., 2022). Furthermore, it gives a 3D data set, which allows to perform 3D change detection. In this study, terrestrial laser scanning is used to monitor erosion processes. The next section will discuss the technique of Terrestrial Laser Scanning in more detail.

2.3.1. Terrestrial Laser Scanning

Laser Scanning, also referred to as LiDAR (Light Detection And Ranging), is a remote sensing technique that determines the distance from the instrument to objects in the surrounding environment by analysing a laser light return from the object's surface (Soudarissanane, 2016). To measure range, two techniques are available: (1) pulse-based or Time-of-Flight (ToF) and (2) continuous wave (CW). With ToF laser scanners, precise timing is used. These scanners use a very accurate clock mechanism to determine the time difference between the transmission and the registration of the laser pulse echo after reflection (Stal et al., 2021). The continuous wave scanners continuously emit a signal of moderate intensity. Based on the difference in phase between emitted and reflected waves, the distances are calculated. This surveying technique allows for a rapid acquisition of large amounts of 3D coordinates of objects' surfaces, with a high level of precision. Most scanners also obtain the reflected intensity of the laser pulse from all points of objects' surfaces. This intensity depends on the range distance, incidence angle, material reflectivity, atmospheric transmittance and the system characteristics of the used scanner (Winiwarter et al., 2021). The scanner device can be placed on different platforms. Possibilities for close to mid-range LiDAR sensors are laser scanning from a drone (or UAV: unmanned aerial vehicle), airborne laser scanning (ALS), mobile laser scanning (MLS) or terrestrial laser scanning (TLS). For MLS, the scanner is situated on a moving platform, such as a boat, train or car. TLS is ground-based and during a scan, the scanner is placed on a stable, stationary platform, such as a tripod. In this study, a Time-of-Flight terrestrial laser scanner is used. An example of such a set up is shown in Figure 2.4. A Terrestrial Laser Scanner (TLS) makes it possible to semi remotely survey areas that are complex or inaccessible to traditional surveying techniques, such as levelling or total station. A TLS consists of a rotating motor and a rotating mirror. In this way, with both components rotating 180° the resulting point cloud covers almost 360° in both horizontal and vertical directions. However, the scanner cannot scan surfaces right underneath itself, since the motor and tripod are obstructing this view.

Figure 2.4: Example of a ToF laser scanner, the Leica ScanStation P40, on a tripod.

As with every measurement devices, measurements from the TLS are subject to noise. The influencing factors can be grouped in four main groups: the scanner mechanism, atmospheric conditions, object properties and scanning geometry (Soudarissanane, 2016):

- **Scanner mechanism**: misalignment of hardware components, calibration, settings and the variations of the emitted laser beam properties and its detection process.
- **Atmospheric conditions**: errors related to the atmospheric conditions (humidity, temperature and pressure variations). Also the presence of ambient lighting is taken into account (total darkness, artificial light or natural sunlight).
- **Object properties**: surface properties (reflectivity, roughness of the surface material with respect to the wavelength of the scanner).
- **Scanning geometry**: the placement of the TLS relative to the location and orientation of the scanned surface, which determines the local incidence angle, the local range and local point density of the laser points sampling the surface.

After a TLS survey, a point cloud is acquired, which is a 3D data set that represent all laser returns from objects in the surroundings of the instrument.

Using the comparison with other remote sensing techniques and the description of working principles of TLS, Table 2.1 summarises advantages and drawbacks of Terrestrial Laser Scanning.

Table 2.1: Advantages and drawbacks of Terrestrial Laser Scanning

Advantage	High spatial resolution (high point density)
	High accuracy
	Full 3D data set
	Possible in complex terrain
Drawback	Limited temporal resolution, compared to satellite data which has daily coverage
	Dependent on weather conditions, not possible in rainy conditions
	Data processing can be complex and computationally intensive
	A labour intensive campaign is needed at the study area, so not fully remotely.

3

Point Clouds: Structure, Handling and Processing

A terrestrial laser scanning campaign results in the acquisition of a point cloud. This chapter explains the basics of point clouds. Also, some well-established methods of processing and analysing point clouds are introduced.

Point clouds are 3D data sets that represent objects or space. The points represent the x, y and z coordinates of a single point on an underlying sampled surface. Point clouds are the collection of these single spatial measurements. Intensity or RGB-values can also be part of the information; in that case a point cloud becomes a 4D (or even higher dimensional) data set. Point clouds are often generated using 3D laser scanners and LiDAR technology. Figure 3.1 visualises an example of a point cloud. The sea water surface is not represented by points, since the water will absorb all the energy, instead of reflecting it. Furthermore, the intensity varies for different objects. For example, bare earth patches give higher intensity than various types of vegetation. Every type of material is characterised by a certain reflectivity.

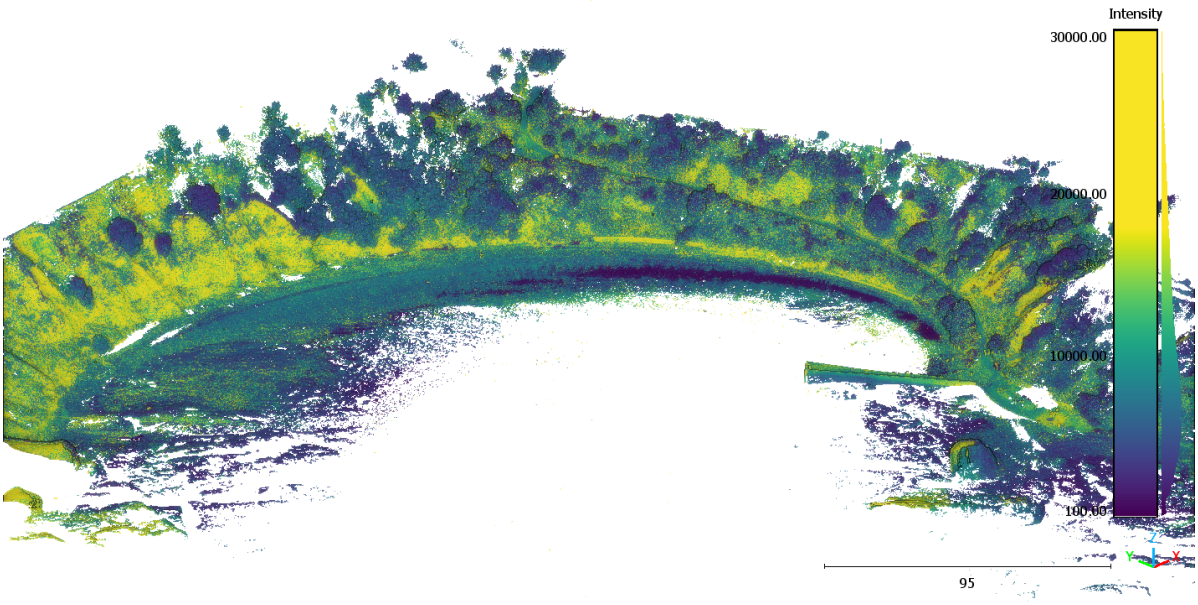

Figure 3.1: The point cloud of the 2022 terrestrial laser scan acquisition of the Catterline Bay, colourised with the intensity. Water surface is not represented with points. Intensity varies for different objects.

For human eyes, the visualisation of this spatial arrangement of points in Figure 3.1 is already sufficiently clear to reason about specific structures in a scene. However, the unstructured and unordered point clouds lack semantic information, which is required to do any kind of interpretation or analysis (Mayr et al., 2017). Due to strongly varying point densities, different types of objects and surveying complex terrain, it is challenging to analyse raw point cloud data (Weinmann et al., 2017). Groups of points in 3D space can represent a 2D surface (i.e. a roof or a wall of a house), which makes interpretation more complicated. Based on the spatial arrangement of 3D points within a local neighbourhood, geometric features can be derived. These features can support what humans already partially see from the spatial arrangement of points, but now based on a neighbourhood calculation.

3.1. Methods and Principles

In this Section, several methods of processing point clouds are introduced. First of all, the widely used technique Principal Component Analysis is shortly summarised. This technique is needed to introduce the computation of geometric features. Then, the terrain models are introduced. Lastly, a wide range of methods to filter ground points is discussed.

3.1.1. Principal Component Analysis

To generate the features, Principal Component Analysis (PCA) is used. PCA aims to transform a set of possibly correlated variables into a set of uncorrelated variables that can be considered as a set of orthogonal linear combinations of variables that maximise the variance of each combination in rank. These uncorrelated variables, representing the reduced dimensions are called Principal Components (PCs) (Nurunnabi et al., 2022). PCs are computed by using the Singular Value Decomposition (SVD) to the covariance matrix, C,

$$C = \frac{1}{n} X^T X \tag{3.1}$$

where X is the mean centred data matrix, having n observations and m variables, $X = x_i - c$ ($i = 1, 2, \ldots, n$), x_i is the ith row of the matrix X and c is the centre (mean) of n observations. PCs are usually sorted in descending order of the non-negative eigenvalues. The first PC then describes the largest proportion of the data variance.

3.1.2. Geometric Features

Next to intrinsic properties of the laser scanner and the resulting point cloud (point coordinates and intensity), certain geometric features can be computed for each point (Nurunnabi et al., 2022). These geometric features are computed based on the local dimensionality of a point and they depend on a user specified local neighbourhood. To get the respective neighbourhood in three dimensions, the k nearest neighbour (kNN) algorithm is used, which avoids problems with point density variation and lack of adequate redundant observations. Geometric features for a point of interest are derived from the covariance matrix of the respective neighbours. To generate the features, PCA is used, which results in 3 PCs (PC1, PC2, PC3) with corresponding eigenvalues λ_1, λ_2 and λ_3 with $\lambda_3 \geq \lambda_2 \geq \lambda_1 \geq 0$. The most common geometric features are: the three eigenvalues from PCA ($\lambda_1, \lambda_2, \lambda_3$), the proportion of variance explained by each eigenvalue (p_1, p_2, p_3) roughness, surface point normal vector (n_x, n_y, n_z), curvature (σ), linearity (L), planarity (P), scattering (S), omnivariance (O), eigentropy (E) and verticality (θ) (Nurunnabi et al., 2022), (Pauly et al., 2002). The proportion explained by each eigenvalue is defined as (Brodu & Lague, 2012):

$$p_i = \frac{\lambda_i}{\lambda_1 + \lambda_2 + \lambda_3} \tag{3.2}$$

The roughness for a certain point is defined as the distance between that point and the best fitting plane computed on its nearest neighbours. In Figure 3.2 roughness, p_1 and p_2, which are the proportion of variance explained by the first and second PCA eigenvalue, are visualised for a small part of the studied area. It can be seen that smooth surfaces, such as the road and the beach, have distinctive other values than parts of the slope with vegetation. Also bare earth patches on the slope can be seen. p_1 and p_2

are also referred to as local dimensionality features, since they reveal whether the cloud in that local neighbourhood appears mostly 1D, 2D or 3D (Brodu & Lague, 2012).

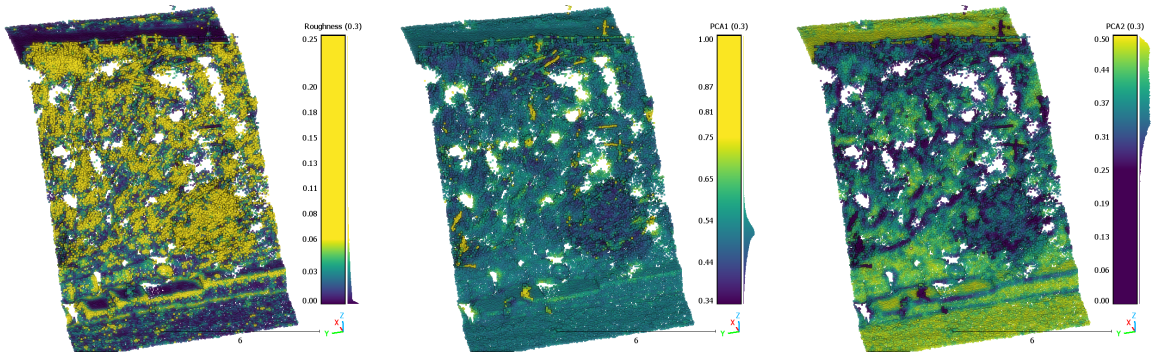

(a) Roughness

(b) Proportion of variance explained by the first PCA eigenvalue

(c) Proportion of variance explained by the second PCA eigenvalue

Figure 3.2: For the computation of the geometric features a neighbourhood of $r = 0.30$m is used.

3.2. Digital Terrain Model

To reveal relevant information about erosion processes from point clouds, it is essential to classify the points in ground and non-ground. From the ground points, the terrain height can be derived. This model of terrain heights is called a Digital Terrain Model (DTM) and includes only the bare-earth, without man-made objects or vegetation. This differs from a Digital Surface Model (DSM), which also includes all objects and structures on the terrain, as shown in Figure 3.3 (Ledoux et al., 2021).

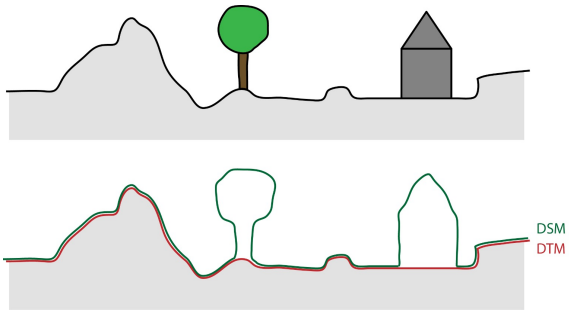

Figure 3.3: Top: A terrain with a mountain, a tree and a building. Bottom: its DSM and DTM. Figure based on illustration from Ledoux et al., 2021.

A DTM can be acquired from LiDAR data, which are 3D point clouds. To generate a DTM from these point clouds, ground an non-ground points have to be separated. This filtering process is a delicate process, for which various types of algorithms have been proposed. The design of an automatic and universally applicable algorithm is still a big challenge (Zhang et al., 2016).

3.3. Ground Filtering

From a LiDAR point cloud, the non-ground points have to be removed in order to create a DTM. Already numerous methods exist to filter non-ground points: iterative interpolation based, slope-based, segmentation-based, cloth simulation, machine learning and mathematical morphological based methods. Each method has its strengths and weaknesses. The optimal choice of method can be hard, because validation of the generated DTM is often complicated. In order to validate the performances of the filtering methods, Sithole and Vosselman (2004) published a comparison study based on 15 reference study sites, representative of different environments, provided by the International Society for Photogrammetry and Remote Sensing (ISPRS). Results indicated that most filters perform well in flat, smooth and uncomplicated landscapes, but landscapes containing steep slopes with vegetation and

abrupt changes are still problematic (Chen et al., 2013). However, it is not possible to blindly use the best method from the paper of Sithole and Vosselman (2004), since the point clouds of that study came from 2.5D airborne laser scanning (ALS). In other words, one cannot apply a 2.5D method one-to-one to dense 3D point clouds obtained from ground based LiDAR data. It could be that a full 3D approach is needed. Furthermore, the terrain in this study contains some steep slopes and complicated vegetation, so this also needs attention. In this section, some methods to be tested in this research are discussed.

3.3.1. Cloth Simulation Filter

An effective ground filtering method is an algorithm called Cloth Simulation Filter (CSF) . This filtering algorithm is capable of approximating the ground surface with a few parameters (Zhang et al., 2016). The algorithm is based on the observation that the lower points are usually forming the ground (assuming that no outliers appear below the ground in the data set). The key idea is to invert (upside-down) the point cloud and to let a piece of cloth fall from the sky. The cloth will fall until it reaches the points forming the ground. During the process, we aim to control the tension (or rigidity) of the cloth, so that areas where there is no sample point or where there are large buildings can be filled realistically. When the process is completed, the surface of the cloth can be used as an approximation of the bare-earth (Ledoux et al., 2021). The CSF algorithm is a simplification of an algorithm in computer graphics to simulate a piece of cloth falling on an object. The cloth is modelled as a surface formed of particles (vertices) that are regularly distributed on a grid, these particles have a mass and they are connected to their neighbours. For terrains the particles are constrained to only move vertically.

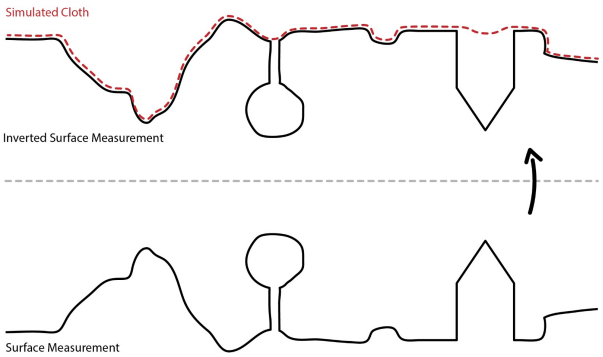

Figure 3.4: Illustration of the Cloth Simulation Filter algorithm. The original point cloud is turned upside down, and then a simulated fabric falls on the inverted surface from above, dividing the point clouds into ground and non-ground parts.

When setting up the Cloth Simulation Filter, some general parameters and advanced parameters need to be set.

- **Scenes**: this setting helps to set the scene type of the point cloud (steep slope, relief and flat). When setting this parameter, the rigidness will be determined.
- **Slope post processing for disconnected terrain**: for steep slopes, the algorithm yields relatively large errors because the simulated cloth is above the steep slopes and does not fit very well with the ground measurements. Using this option, this problem can be partially solved.
- **Cloth resolution**: with this setting, the grid size of the cloth can be tuned, which is used to cover the terrain. A bigger cloth resolution results in a coarser DTM.
- **Max iterations**: this refers to the maximum iteration times of terrain simulation.
- **Classification threshold**: this refers to a threshold to classify the point clouds into ground and non-ground parts based on the distances between points and simulated terrain.

3.3.2. Ray Tracing Voxel Method

Another approach to tackle the filtering of points is by looking at ray tracing. For this method, all possible laser beams of each laser scan location are traced and decomposed. In order to do this, the point cloud is enclosed by the minimum bounding box. This box is divided in 10x10x10 cm voxels and then stored in the memory as a data cube. Each individual scan is traced and written to the cube. The role of each pixel is evaluated: it can either be intersected by a ray, the end point of a ray or neither intersected nor an end point of a ray. This idea is visualised in Figure 3.5. For each role, a specific marker is given to the pixel. Pixels marked as 0 are undefined. Other pixels are a sum of binary markers: 1 for air, 2 for object and 4 for the scanner. Hence, the final sum of 3 can indicate a voxel with a combination of markers: marked both as an object as well as air. From this marking process, true ground voxels can be extracted. In literature, this method is also referred to as Voxel Beamlet Superposition (VBS) framework.

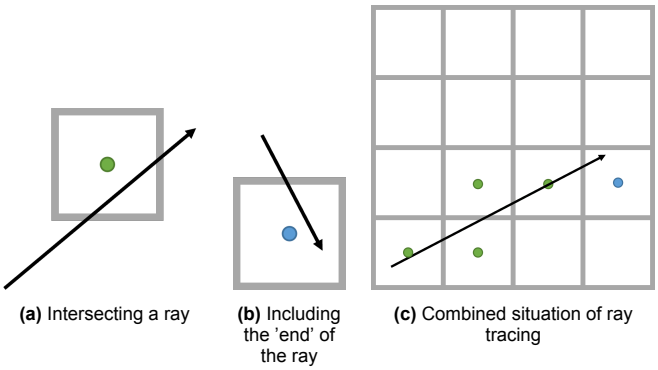

Figure 3.5: (a) is labelled as free (green) and (b) is as occupied (blue). (c) is subdivided into multiple voxels and labelled accordingly. Idea of this illustration comes from Min et al. (2020).

A shortcoming of this model is the assumption that the laser bundle has a very small beam width. In reality the beam width increases for larger distances from the scanner. This means that a laser beam can penetrate two different voxels at a certain distance from the scanner. This is not considered in this simplified model.

3.3.3. Multi-resolution Hierarchical Classification Method

A possible method to extract ground points from raw point clouds is the use of interpolation-based filters. As the name of this type of filter suggests, a critical step here is to construct reference surfaces using interpolation methods. One promising method of this type is the multi-resolution hierarchical classification method (MHC) (Chen et al., 2017). The International Society for Photogrammetry and Remote Sensing (ISPRS) commission provided fifteen benchmark reference samples from seven sites to assess the performances and this MHC had the best overall performance (Chen et al., 2013; Sithole & Vosselman, 2004). However, one important remark is that all data came from airborne laser scanning and all methods are designed towards this type of data. Therefore, this does not give any guarantee that the method will perform well on TLS data.

MHC achieves surface interpolation with a robust finite difference thin plate spline (Chen et al., 2017). Thin plate spline (TPS) with high interpolation accuracy and numerical stability has been commonly adopted. Because analytical TPS has a high computational cost due to its local interpolation of the huge volume of data points for surface construction, the reference surface can be globally and efficiently produced by finite difference TPS in case of gridded data. The method uses a hierarchy of three levels, where the resolution of reference surfaces increases from a low to a high level. The method incorporates existing interpolation methods: analytical TPS and weighted finite difference TPS. The procedure of MHC is extensively explained in the paper of Chen et al. (2017). In Appendix B some results are shown of the MHC method.

The method is tested on the available TLS data, but the performance was not considered high enough.

3.3.4. Filtering based on geometric features

Based on visual inspection of geometric features of the point cloud, it is clear that the distribution for geometric features of ground points differs from that of vegetation or other non-ground points. For example, ground points seem to represent a smoother plane (representing the surface), whereas tree points are arranged more chaotic. On the other hand, the stem of a tree or the wall of a house can also be smooth. Id est, the arrangement of points is assumed to be different for different objects. This assumption is used to filter ground points from non-ground points. Geometric features such as roughness, the proportion of variance explained by each PCA eigenvalue (p_i) or point density could in theory differentiate between different objects. From visual inspection on the behaviour of various geometric features, computed for different values of the neighbourhood radius, it was found that the proportion of variance explained by each PCA eigenvalue, p_1 and p_2, were quite distinctive for ground and non-ground. In Figure 3.6 the proportion of variance explained by the first and second PCA eigenvalues, p_1 and p_2, are plotted against each other. For ground points from the road section and bare soil section, it can be seen that the behaviour is very different from the tree and low vegetation sections.

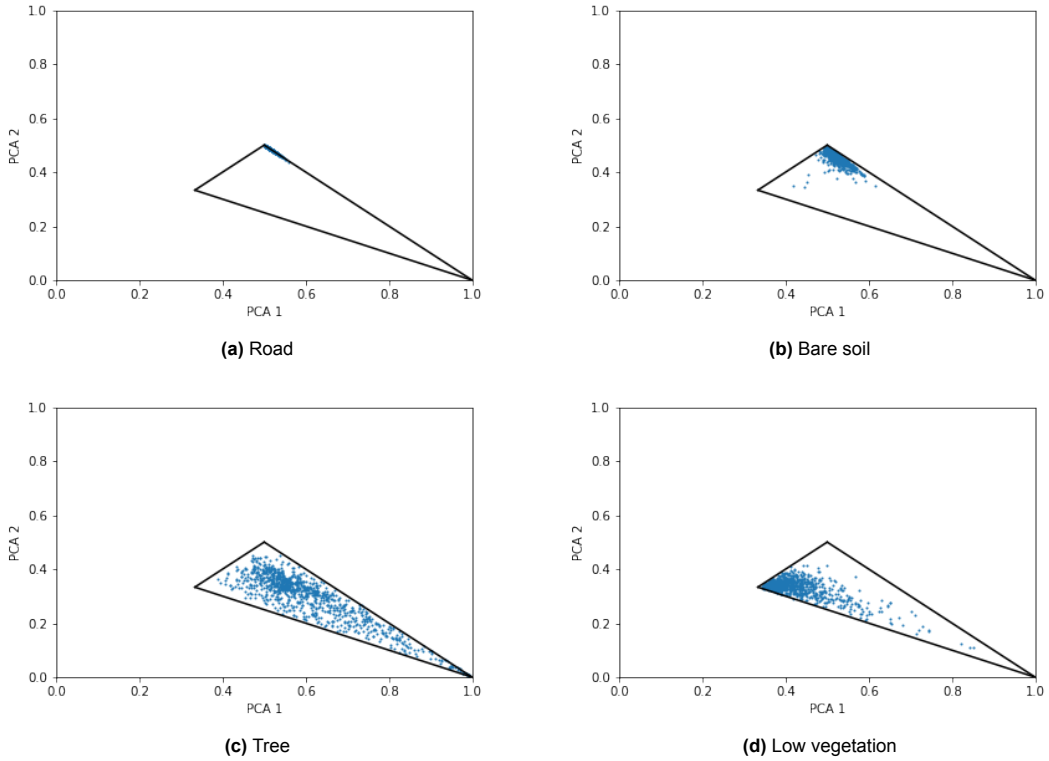

(a) Road **(b)** Bare soil

(c) Tree **(d)** Low vegetation

Figure 3.6: Black lines indicate the domain of possible proportions of eigenvalues for a 3D point cloud PCA.

However, choosing a threshold value manually based on this small analysis would be a bit arbitrary. A possible solution to overcome this arbitrariness is the use of machine learning to fit a decision boundary based on training data. Furthermore, the choice of the neighbourhood radius would strongly influence the filtering. Combining the distribution of geometric features for different neighbourhood radii would be a possible solution for this problem. The next subsection introduces a method which implements these suggested solutions.

3.3.5. Classification with multi-scale local dimensionality features

The CSF and MHC methods are not specifically designed for terrestrial laser scan data, but are more tailored towards airborne laser scanning. Preliminary results from these methods did not give satisfying results. The ray tracing voxel method and the filtering based on geometric features both had potential, but needed a more sophisticated implementation. The latter will be incorporated in a classification algorithm.

In this subsection, a relatively new method developed by Brodu and Lague (2012) is introduced: CANUPO (CAractérisation de NUages de POints). This is a classification algorithm based on separating two classes (for example ground and non-ground), which has given good results in complex cases (steep terrain, specific vegetation) and has a real 3D approach, instead of 2.5D as with most filtering techniques for ALS data.

From the insight that a geometric feature helps to characterise different classes of points, a classifier based on local dimensionality at multiple scales is created. Local dimensionality means how the cloud geometrically looks like at a given location and a given scale: as a line (1D), a plane surface (2D) or as a sphere (3D) if points are distributed in the whole volume around the considered location. For example, at a small scale (few centimeters) a bare-earth patch looks line a 2D surface and the vegetation is a mixture of elements like stems (1D) and leaves (2D). At a larger scale (about 30cm) the bare earth patch still is mostly 2D, whereas the vegetation has become a 3D bush. When the information from different scales is combined, signatures are build to identify different classes (Brodu & Lague, 2012). In the following the multi-scale dimensionality feature is defined and thereafter the classification procedure is described.

Multi-scale local dimensionality features
Since a 3D point cloud is a set of points, a point cloud can be mathematically written as (Brodu & Lague, 2012):

$$C = \{P_i = (x_i, y_i, z_i)\}_{i=1...N} \tag{3.3}$$

Furthermore, the scale s is defined as the diameter of a ball centred on a point of interest. For each point in the scene, the neighbourhood ball is computed at each scale of interest, and a Principal Component Analysis (PCA) is performed on the recentred Cartesian coordinates of the points in that ball. PCA gives the eigenvalues λ_i, $i = 1, 2, 3$, ordered by decreasing magnitude: $\lambda_1 \geqslant \lambda_2 \geqslant \lambda_3$. As introduced in Section 3.1.2, the proportion of variance explained by each eigenvalue is (Brodu & Lague, 2012):

$$p_i = \frac{\lambda_i}{\lambda_1 + \lambda_2 + \lambda_3} \tag{3.4}$$

When only the first eigenvalue λ_1 accounts for the total variance in the neighbourhood ball, the points are distributed in one dimension around the reference scene point. When two eigenvalues are necessary to account for the variance, the cloud is locally mostly two-dimensional. Similarly, a fully 3D cloud is one where all three eigenvalues have the same magnitude. Thus, proportions of eigenvalues define a measure of how much 1D, 2D or 3D the cloud appears locally at a given scale.

Given the constraint $p_1 + p_2 + p_3 = 1$, a two-parameter feature for quantifying how 1D, 2D or 3D a cloud appears can be defined at any given point and scale. Thus, given N_s scales, a feature vector with $2N_s$ values is obtained for each point in the scene.

Combining the local dimensionality characterisation over multiple scales gives discriminating features, which are used to train the classifier. The use of PCA is a simple and common known tool for finding relevant directions in the neighbourhood ball.

The best combination of scales at which the dimensionality is measured, is when the separability of two or more classes is maximum. However, in many cases, because of natural variability in shape and size of objects, this is far from trivial. In the Cloud Compare software, the CANUPO plugin contains an automated construction of a classifier that finds the best combination of scales to maximise the separability.

The treatment described above is repeated at each scale of interest. The vector describes the local dimensionality characteristics of the cloud around that point at multiple scales. In the context of ground based LiDAR data there may be missing scales, especially the smallest ones, because of reduced point density or nearby shadowing. In that case the geometric properties of the closest available larger scale is propagated to the missing one in order to complete $2N_s$ values.

Classification using Linear Discriminant Analysis
The general idea behind the classification procedure is to define the best combination of scales at which the dimensionality is measured, that allows maximum separability of two or more categories. Practically, the user could have an intuitive sense of the range of scales at which the categories will be the most geometrically different, but in many cases, because of natural variability in shape and size of objects, this is not trivial. Therefore, an automated construction of a classifier that finds the best combination of scales is used.

To be able to define a classifier, the $2N_s$ feature space is considered. First, the data is projected in a plane of maximal separability and then the classes can be separated in this new plane. This method allows for an easy supervision of the classification, since visual inspection is intuitive. In this study, the binary linear classifier Linear Discriminant Analysis (LDA) is used (Bishop, 2006). Another possibility is the use of Support Vector Machines (SVM). Brodu and Lague (2012) show that using one or the other of these classifiers has little impact on the results.

In order to describe how LDA works, some mathematical definitions are introduced. The multi-scale feature space with a dimension of $2N_s$ with (x_i, y_i) the coordinates within the feature space can be written as $F = X = (x_0, y_0, x_1, y_1, ..., x_{N_s}, y_{N_s})$. F^+ and F^- are the sets of points labelled respectively with $+1$ and -1 for the two classes to discriminate (e.g. ground vs non-ground). Now, a linear classifier proposes a solution in the form of an hyperplane that separates F^+ from F^- in the best possible way. This hyperplane is defined as $w^T X - b = 0$, where w is a weight vector and b the bias (Brodu & Lague, 2012). Linear Discriminant Analysis proposes to set $w = (\Sigma_1 + \Sigma_2)^{-1}(\mu_1 - \mu_2)$, where Σ_c and μ_c are the covariance matrix and the mean vector of the samples in class c. Originally, LDA is a non-probabilistic classifier, but the bias b is defined such that a probabilistic interpretation is given to the classification. This approach is referred to as Platt scaling (Platt, 1999). The distance d of a sample to the hyperplane corresponds to a classification confidence, estimated by fitting the following logistic function:

$$p(d) = \frac{1}{1 + \exp(-\alpha d)} \tag{3.5}$$

Then, the feature space F is projected on the hyperplane and the distance to the hyperplane $d_1 - w_1^T X - b_1$ is calculated for every point. This is done once more to obtain the second-best direction orthogonal to the first, along with the second distance d_2. Now (d_1, d_2) is used as the coordinates defining the 2D plane of maximal separability. There is a degree in freedom for choosing w and d such that $w^T X - b = 0$, so the axes are rescaled such that $\alpha = 1$ (Brodu & Lague, 2012).

This classification method allows for semi-supervised learning, which means that it combines a small amount of labelled data with a large amount of unlabelled data during the training, using information present in unlabelled points. This is a great feature, because manually segmenting labelled training data takes a lot of time for the large amount of points in the data. The plane of maximal separability is only computed with labelled examples. However, the searched direction in this plane minimises the density of all (labelled and unlabelled) points along that direction, while still separating the labelled examples. When there is no additional unlabelled data, the classes are separated with a line splitting both with equal probability.

One problem or question that may arise from this proposed binary classification method, is the case of a multi-class scenario. In this case, the final classifier is a combination of elementary binary classifiers. So, ”one against one” elementary binary classifiers are trained, which are then combined by a majority rule.

The most time-consuming parts of the algorithm are computing the local neighbourhoods in the point cloud at different scales in order to apply the local PCA transform, as well as the training process. By computing the multi-scale local dimensionality feature on a subsampling of all points, called the core points, the computing time can be reduced enormously. The whole data is still considered for computing the geometric features, but they are only computed at the core points.

In contrast with other ground filtering methods such as MHC and CSF, CANUPO performs well, when it is applied to dense 3D point clouds from TLS data, where a full 3D approach is needed. Because the CANUPO algorithm works in 3D, the method can also be used on 2.5D point clouds from ALS. The

multi-scale analysis distinguishes CANUPO from other methods. Sites with natural surfaces exhibit a large range of characteristic scales and natural objects within one class can have a large range of geometric behaviour. Therefore, it is impossible to find a single scale that can adequately classify an entire scene. Because all scales contribute to a varying degree to the classification process, the method is relatively robust to shadow effects, missing data and irregular point density. By using a probabilistic classifier, user input is minimised, whereas the generalisation ability is good.

3.3.6. Summary and Discussion

All described methods are applied to the available data, which will be introduced in Chapter 5. From these preliminary results and the literature review, an overview with pros and cons for each method is created in the following.

Cloth Simulation Filter

- **Pros**: Based on a physical process, which makes the filter insightful. Repeatedly validated to be an accurate, automatic and easy-to-use algorithm for ALS point clouds.
- **Cons**: Specifically designed for ALS data. Has difficulties with steeps slopes and discontinuous scarps.

Ray Tracing Voxel Method

- **Pros**: In theory a strong mathematical approach of decomposing laser beams.
- **Cons**: Very basic implementation, needs further development. Computationally heavy.

Multi-resolution Hierarchical Classification

- **Pros**: Good overall performance on 15 reference study sites provided by ISPRS.
- **Cons**: Specifically designed for ALS data. Has some input parameters, which are not so insightful to specify for the user. Heavy computations.

Filtering based on geometric features

- **Pros**: Comprehensible and simple to apply. Full 3D approach.
- **Cons**: Strongly depends on the choice of a neighbourhood radius and a threshold value for filtering, which is hard to substantiate and justify.

CANUPO

- **Pros**: Full 3D approach. Acts on multiple scales. Semi-supervised classification which gives the user insight in the process, but minimises the user input. Easy to use, because it is implemented as a plugin in CloudCompare.
- **Cons**: Requires high-quality training samples and is therefore labour intensive. High computing demand and slow computing speed, because of point-wise classification. For multi-class scenarios, a combination of binary classifiers is needed. Limited flexibility, because it is implemented as a plugin in CloudCompare.

In Appendix B some results from these methods are displayed. From literature review and visual inspection of results of all different methods, it is decided to use CANUPO in the further workflow of this thesis.

A point of discussion is the question why the intensity is not used as a criterion for filtering. Using the reflected laser intensity for classification purposes has been attempted in some studies. However, the difficulties are plenty, since the reflected intensity is a complex function of distance from the scanner, incidence angle and surface reflectance. In simple cases, for which the distance and incidence angle are not greatly changing (cliff survey for instance), the laser intensity can be used to distinguish between materials relatively well (Brodu & Lague, 2012). In simple natural environments it can be used to improve the robustness of a classifier based on simple geometrical parameters. However, for complex scenes, the LiDAR intensity is much more difficult to use given the large changes in distances, incidence angles and state of the surface. Because laser reflected intensity is not globally nor temporal consistent on a complex 3D scene, it cannot be used as a primary classifier. In the case of CANUPO, the reflected intensity could be used as an extra attribute in the classification.

4

Methods

In order to identify erosion zones and assess erosion patterns, point clouds from two laser scan acquisitions are used. The process from raw point clouds to the evaluation of erosion patterns is illustrated in Figure 4.1.

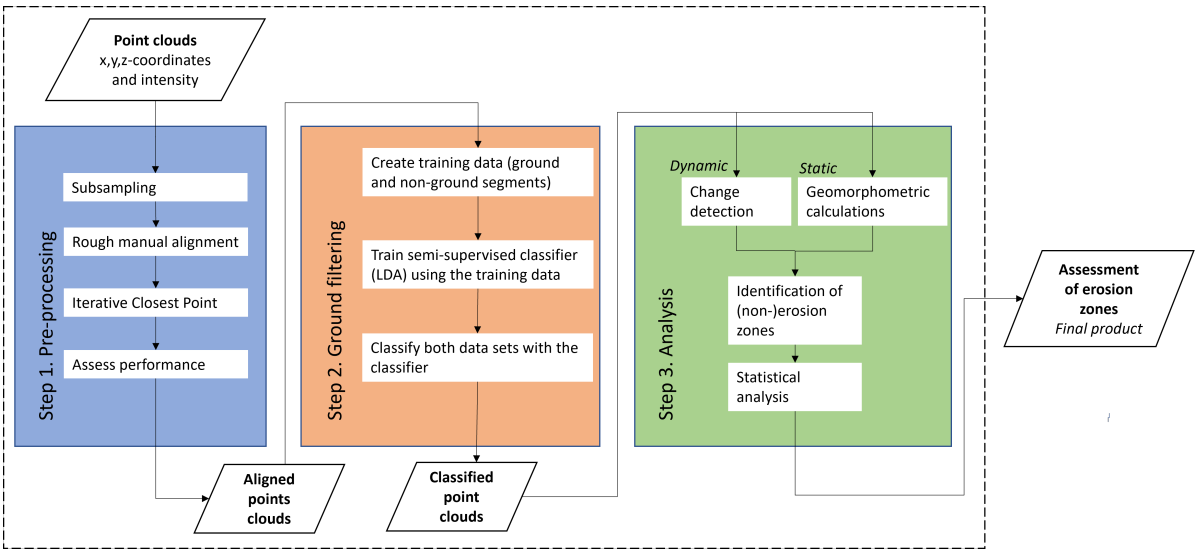

Figure 4.1: Overview of the workflow for alignment, filtering and analysis

From one point cloud acquisition, a static analysis can be performed. Erosion zones can be revealed based on the slope and other geomorphometric calculations, which are introduced in Section 4.3. Furthermore, Section 4.4 explains how distance calculations between vegetation and ground points give information about vegetation heights. If multiple point cloud acquisitions are compared, a dynamic analysis allows to detect changes. Section 4.5 describes a 3D change detection method. Change detection is either point cloud based or by comparing different derived GIS layers.

All elements of this process are discussed in this chapter.

4.1. Pre-processing

All individual scans from one year are registered using the precise coordinates of the reflector targets, which results in a combined point cloud. The original point clouds from 2019 and 2022 are too big to open in the software CloudCompare on a personal laptop, so they are subsampled to 50 mm. This means that the software picks points from the original cloud such that no point in the output cloud is closer to another point than 50 mm.

4.1.1. Registration

To be able to compare multiple laser scan acquisitions, point clouds have to be spatially aligned. The goal is to minimise the difference between two point clouds using a rigid transformation. A rigid transformation is defined as a geometric transformation that preserves the Euclidean distance between every pair of points. Rigid transformations include rotations and translations or any sequence of these. A classic and well-known registration formulation is the Iterative Closest Point algorithm (ICP).

Iterative Closest Point

In the ICP algorithm, the *reference* (also target) is kept fixed, while the other one, the *source*, is transformed to best match the reference. The algorithm repeatedly reconsiders the transformation (combination of translation and rotation) needed to minimise an error metric, which is usually defined as the distance from the source to the reference cloud (sum of squared differences between the coordinates of the matches pairs) (Besl & McKay, 1992). Iterative closest point is a non-linear least squares method. The input data are two point clouds (reference and source) and the output is the transformation matrix to align the source point cloud with the reference point cloud. Furthermore, a final root mean square (RMS) error is computed on 50,000 points. In Figure 4.2 the principle of ICP is illustrated. ICP can only guarantee the convergence to a local minimum, thus the user of the algorithm needs to be aware that the algorithm can get stuck in a local solution (J. Yang et al., 2013). To prevent this, the point cloud is manually aligned, before applying ICP. The most important tuning parameters are the number of iterations or RMS difference and final overlap:

- **Number of iterations** or **RMS difference**: ICP is an iterative process. In this case, it means that the registration error decreases every iteration. To stop the iterations, either a maximum number of iterations can be given as a parameter or as soon as the RMS error difference between two iterations becomes below a given threshold.
- **Final overlap**: This parameter lets the user specify the actual portion of the data in the registered cloud that should overlap the reference cloud if both clouds are registered. In this way, entities with only a partial overlap can be registered.

A RMS difference of 1.0×10^{-5}m is used. For the final overlap, 90% is used, but during iterations of applying the ICP algorithm, the overlap is gradually decreased to 40%. This is done, because the amount of stable objects is assumed to be around this percentage in the complete scene. However, this is only a rough estimate. The main driver in tuning the parameters is decreasing the RMS difference.

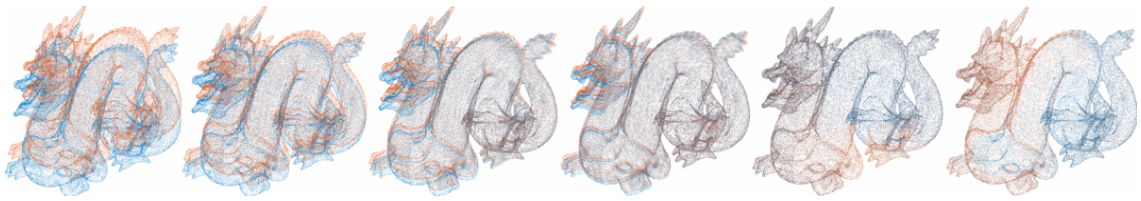

Figure 4.2: An example of ICP, where the source dragon is iteratively transformed to get the best match to the reference dragon. Illustration from Glira and Pfeifer (2015).

4.2. Classification of ground points

After discussing and comparing different methods of filtering ground points in Section 3.3, the semi-supervised method CANUPO seemed the most suitable one in this research. In this section more details are provided to apply this method.

Since CANUPO is a semi-supervised classification method, training data is prepared by manually selecting segments of non-ground and ground. For each class several typical subsets of points should be included. Also, the two subsets should have roughly the same total number of points or the relative quantities are representative of their occurrence in the whole point cloud. After regrouping each class in a single cloud, the classifier can be trained. Two parameters are described below:

- **Maximum number of core points**: these points will be randomly extracted from the input cloud.

- **Scales**: The scales at which the descriptors are calculated, can be specified. The more scales are used, the more discriminative the result can be, but also the longer the computations.

To evaluate the performance of the classifier the balanced accuracy (ba) is used, which is especially useful in case of a different number of points in each class. With tv, tg, fv and fg the number of points truly (t) or falsely (f) classified into vegetation (v) or ground (g), the balanced accuracy is defined as (Brodu & Lague, 2012):

$$ba = \frac{1}{2}(a_v + a_g) \text{ where } a_v = \frac{tv}{tv + fg} \text{ and } a_g = \frac{tg}{tg + fv} \tag{4.1}$$

A large ba value indicates a good recognition rate (0.5 implies random class assignment). Also, the precision is used, which is defined as the fraction of correct predictions for a class:

$$\text{precision} = \frac{tv}{tv + fv} \tag{4.2}$$

In order to assess the class separability, the Fisher Discriminant Ratio (fdr) is used. The classifier assigns to each sample a signed distance d to the separation boundary (negative values for one side and positive for the other). The measure of separability is defined as (Brodu & Lague, 2012):

$$fdr = \frac{(\mu_2 - \mu_1)^2}{v_1 + v_2} \tag{4.3}$$

where μ_c and v_c are the mean and variance of the signed distance d for class c. An important note is that class separability can still be high despite a not so good accuracy. This can indicate a bad training with potential for better separation. A large fdr value indicates that classes are well separated (and that the ba score is robust) (Brodu & Lague, 2012).

The performance of the classification is not only assessed on the training data set. To obtain a better view on the precision, also a test data set is created. The test data set contains points, labelled by the supervisor as ground or non-ground points. A first attempt of creating the test data set in this thesis work resulted in a too positive display of the performance. Because the test data set only contained very clear cases of ground or non-ground points, the test data set was not a good representation of the complete point cloud. Therefore, it is important that the test data set contains all kinds of ground and non-ground points, also points where the class is not directly evident. The final test data also contained less clear cases of ground and non-ground points, to obtain a better representation of the point cloud. However, the test data set will still have some inevitable bias, because it only contains points of which the supervisor was to some degree sure to which class the points belonged.

4.3. Static Analysis: Geomorphological Indicators

As discussed in Section 3.2, a Digital Terrain Model can be created from point clouds. From a DTM, topographical or geomorphometric quantities can be derived. A geomorphometric approach to analyse landslides can help identifying landslide locations. By characterising landslides and related phenomena using quantitative indices, it provides a more objective insight. Furthermore, geomorphometry can reveals 'hidden' topographic features in landslide terrains (Rózycka et al., 2017). These metrics include among others slope angle, the topographic wetness index and topographic ruggedness index. For example, the slope angle is one of the key factors in inducing slope instability (Sarkar & Kanungo, 2004). In this section, the metrics are explained shortly.

From point clouds, topographical maps can be derived. Other resources to create data layers with are geological and environmental parameters (Yilmaz, 2009). However, these data layers often used at larger scales.

4.3.1. Digital Terrain Model

From the classified ground points in the point cloud a raster is created. This raster represents the Digital Terrain Model (DTM). The spatial resolution of 0.05m is used to create the raster, which gives 8947x10288 cells. A finer resolution is not needed, because of the accuracy of the used measurement set up and the previous processing steps. This raster gives the height of the digital terrain model. To visualise the terrain more insightful, hillshade is added to give a shaded relief effect.

4.3.2. Slope Angle

The slope angle for a particular location is computed as the maximum rate of change of elevation between that location and its eight neighbouring cells. Horn's formula is used to compute the slope. In comparison to the other often used formula Zevenbergen & Thorne, Horn's formula is known to perform better on rougher terrain. Horn's method uses the 8 neighbouring cells to calculate the slope. It applies a weight of 1 to the 4 corner cells (the indirect neighbours) and a weight of 2 to the other 4 cells (the direct neighbours) (Horn, 1981).

4.3.3. Topographic Wetness Index

The Topographic Wetness Index (TWI) is a useful model to estimate where water will accumulate in an area with elevation differences and is used to study spatial scale effects on hydrological processes (Ambroise et al., 1996; Sørensen et al., 2006). It is a function of slope and the local upslope contributing area:

$$\mathrm{TWI} = \ln \frac{a}{\tan b} \tag{4.4}$$

where a is the local upslope contributing area draining through a certain point per unit contour length and $\tan b$ the local slope (Sørensen et al., 2006). TWI is a unitless quantity. Low TWI values indicate areas with less 'wetness' and high TWI areas that are bodies of water. When the angle b is large or the local upslope contributing area a small, such that $\frac{a}{\tan b} < e$, then the TWI will be negative, indicating low wetness. On catchment scale, spatial patterns of high TWI values can help to identify lines of preferred drainage of a landslide body (Rózycka et al., 2017). In essence, TWI is an indicator of convexity (plan view) and concavity (cross-section view). At cm-scale, however, it is not completely clear how TWI links to landslides. TWI still gives drainage patterns, but it is unknown if these can be related to erosion zones.

4.3.4. Terrain Ruggedness Index

The Terrain Ruggedness Index is a parameter that quantifies surface roughness through consideration of absolute elevations in the surrounding of a given location (or raster cell). The TRI of a cell is calculated as the squared sum of the squared differences with the eight neighbouring cells ($i = 1, ..., 8$) (Riley & Degloria, 1999):

$$\mathrm{TRI} = \sqrt{\sum_{i=1}^{8} (z_c - z_i)^2} \tag{4.5}$$

where z_c is the elevation of the evaluated cell and z_i the elevation of one of the neighbouring cells. From the formula can be seen that the units of the TRI are meters. The computation of the TRI is sensitive to local differences in elevation, so the presence of a long and steep scarp is likely to increase the average value of the calculated TRI for a landslide (Rózycka et al., 2017). Therefore, outcomes of TRI calculations strongly depend on the used spatial resolution.

Rózycka et al. (2017) concluded that TRI is especially useful to characterise depositional parts of landslides.

4.4. Presence and Height of Vegetation

This section describes a newly developed method to derive vegetation height from classified point clouds. Section 2.1 and Section 2.2 suggest a link between presence of vegetation and occurrence

of landslides. Although the height of the vegetation is not directly linked to landslides, the root system of vegetation does have influence. For example, a soil with roots creates composed material that has enhanced strength (Gonzalez-Ollauri & Mickovski, 2021). Various studies (Guerrero-Campo & Fitter, 2001; Li & Bao, 2015) showed a strong positive correlation between vegetation height and root system size. Because most nature based solutions (NBS) are focused on soil-root reinforcement, the evolution and effectiveness of the NBS can be monitored by the changes in presence and height of vegetation.

From the classified ground points, a mesh is created, representing the DTM. Now, cloud (non-ground points) to mesh (DTM) distances are calculated. Since almost all non-ground points correspond to vegetation, these distances are a good measure for the vegetation height. In the case that points in the non-ground points do not belong to vegetation, either the CANUPO algorithm can be applied to separate two distinct classes or the non-vegetation points can be segmented out manually. In the cloud to mesh distances, it is assumed that the vegetation height is equal to the shortest distance to the ground. In some cases, this assumption may not hold completely.

4.5. Dynamic Analysis: 3D Change Detection Methods

Previous discussed susceptibility indicators are calculated from the DTM from one acquisition in time. Next to these static indicators, the comparison of two or more acquisitions allows for change detection. This change detection can be focused on local distances between two point clouds acquisition, but also on changes in gully or channel locations, changes in objects or volume changes.

After removing non-ground points, 3D change detection is a suitable way to quantify the on-going erosion. However, this can be a complicated task in the context of rough complex topographies without corresponding elements among successive point clouds.

Because of uncertainties and ambiguities, two point clouds will never have the exact same point sampling on the surface and no one-to-one point homology can be established. With no one-to-one point homology, it is meant that one point for a first point cloud can never be matched to one specific point from a second point cloud. Therefore, point-to-point distances cannot be calculated (Winiwarter et al., 2021). Various distance measurement methods without point homologies have been developed, such as DEM of difference (DoD), direct cloud-to-cloud comparison with closest point technique (C2C), cloud-to-mesh distance or cloud-to-model distance (C2M).

The current state-of-the art method in geomorphological point cloud change analysis is Multiscale Model to Model Cloud Comparison (M3C2) (Lague et al., 2013). This latter method is the most sophisticated method, because it is able to operate in complex 3D cases and can also be used as a simpler and more robust alternative to DEM differencing in 2D cases. M3C2 operates directly on point clouds without meshing or gridding and computes the local distance between two point clouds along the normal surface direction, which tracks 3D variation in surface orientation. It also provides an estimation of the confidence interval for each distance measurement depending on point cloud roughness and registration error.

4.5.1. Multiscale Model to Model Cloud Comparison (M3C2)

The starting point of this algorithm is the estimation of a local surface normal vector (**N**) fitting a plane to the points contained in the neighbourhood for any given point i defined by a radius $D/2$. D is named the normal scale and it is a crucial parameter in M3C2 distance analysis, because it determines the normal direction in which changes will be searched (Gómez-Gutiérrez & Gonçalves, 2020). When the normal is defined for a core point i, then it is used to project i onto each cloud at scale d (called projection scale). This amounts to defining the average positions i_1 and i_2 of each cloud in the vicinity of i (Step 1 in Figure 4.3). Then, a cylinder with radius $d/2$ is defined, whose axis goes through i and which is oriented along the normal vector **N**. To speed calculations up, a maximum length of the cylinder is imposed (Lague et al., 2013). The average position of each cloud (i_1 and i_2) is obtained using the location of points within the previously defined cylinder and projecting i_1 and i_2 along the axis of the cylinder (Step 2 in Figure 4.3). So, the distance between i_1 and i_2 in the normal direction is the resulting M3C2 distance and is stored in one of the two point clouds together with an uncertainty measure. The uncertainty measure is derived from a confidence interval, which is used to assess whether a statistically significant change is detected at a prescribed confidence level (Lague et al.,

2013). This confidence interval boundary corresponds to the minimum detectable change, so it is also referred to as the Level of Detection (LoD) at x% ($LOD_{x\%}$). Change below this minimum amount of change is indistinguishable from noise from different sources (Winiwarter et al., 2021). In the paper of Lague et al. (2013) it is derived that:

$$LOD_{95\%}(d) = \pm 1.96 \left(\sqrt{\frac{\sigma_1(d)^2}{n_1} + \frac{\sigma_2(d)^2}{n_2}} + r \right) \tag{4.6}$$

where σ_1 and σ_2 are the independent variances of point positions for each sub-point cloud and r corresponds to the co-registration error between the two compared point clouds.

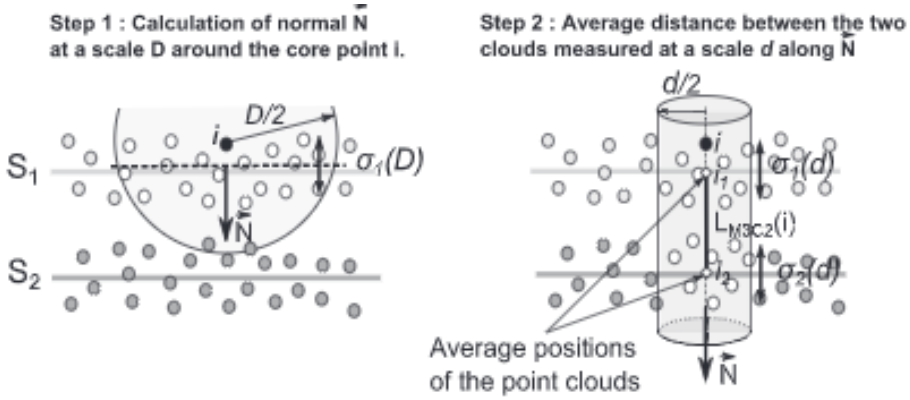

Figure 4.3: Illustration of the M3C2 algorithm with parameters D (normal scale) and d (projection scale). Two steps of the algorithm are visualised. Step 1: The normal is estimated from cloud 1. The scale at which the cloud is most planar will be selected. Step 2: 2 sub-clouds are defined by the intersection of the reference and compared clouds with a cylinder of diameter d and axis $(i, \vec{N})$. Each sub-cloud is projected on the cylinder axis which gives a distribution of distances along the normal direction. These are used to define the mean (or median) position of each cloud i_1 and i_2. Illustration from Lague et al. (2013).

The M3C2 algorithm is integrated as a plug-in in the open-source software CloudCompare. The parameters (D, d and h) can be defined by the user or estimated automatically by the algorithm on the basis of point cloud density and roughness:

- **Normal scale** (D): the diameter of the spherical neighbourhood extracted around each core point to compute a local normal. The normal is used to orient a cylinder inside which equivalent points in the other cloud will be searched for.
- **Projection scale** (d): the diameter of the above cylinder.
- **Max depth**: corresponds to the cylinder height (in both directions).
- **Selection of the core points**: these points will be used for the computations. Since it is not necessary to measure the distance at such a high density, either the whole cloud, a sub-sampled version of the input cloud or a custom set of core points can be chosen as a selection.

The bigger the first two radii are, the less local surface roughness and noise will influence the computation, but also more points will be 'averaged', so the slower the computation will be. Furthermore, some options about the normals can be chosen. In this research, the multi-scale option is used: for all core points, normals are computed at several scale and the most 'flat' one is used. In this research, the following settings are a normal scale of $D = 1.0$m, a projection scale of $d = 0.5$m and a max depth of 15m. For the multiscale option, a range between 0.1m and 2.1m is used with steps of 0.25m.

5

Data and Study Area

This chapter describes the study site in detail. Also, the data availability is discussed and an explanation of how to do a terrestrial laser scan (TLS) survey is given.

5.1. Study Area

The study area is situated at the bay in Catterline, Aberdeenshire, North East Scotland (see Figure 5.1). The small study area of circa 0.2 km^2 has an mean annual temperature of 8.9° C and a mean annual rainfall of 565 mm (Gonzalez-Ollauri & Mickovski, 2016). The precipitation is characterised by frequent, low-intensity rainfall events, whereas heavy storms rarely occur.

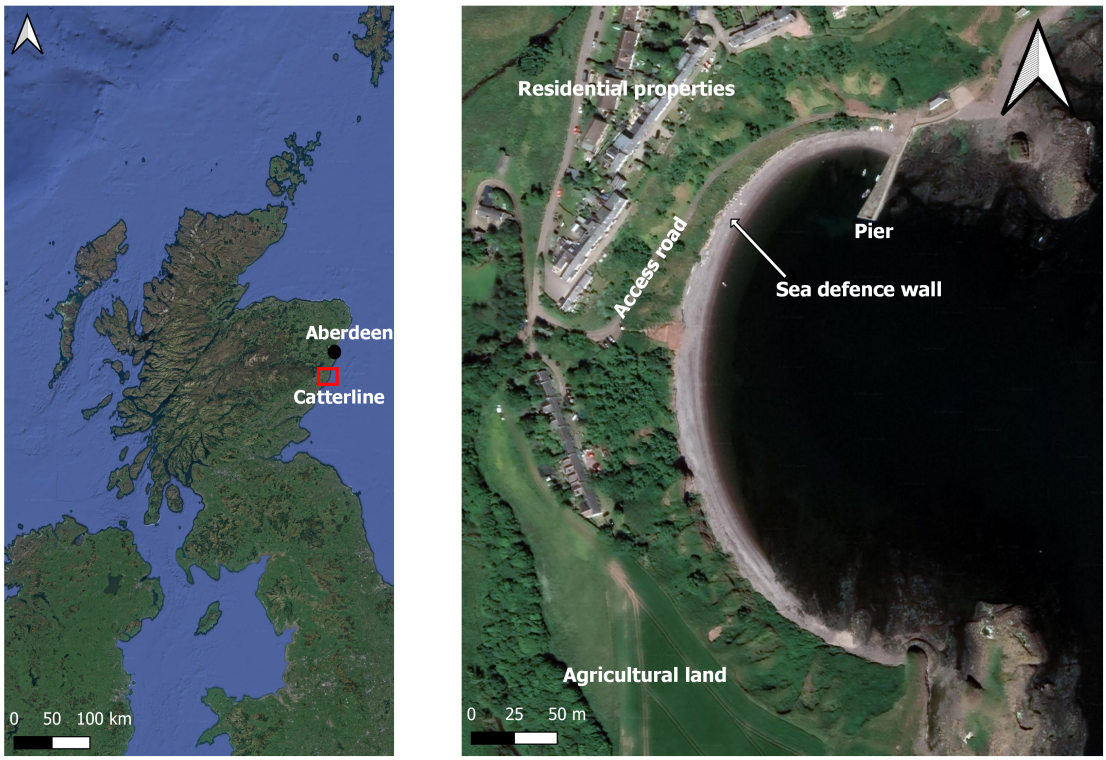

Figure 5.1: The study area, the Catterline Bay, as seen from Google Satellite Imagery.

The topography of the study site is dominated by sloped ($25 - 50°$) terrain and cliffs ending up into the sea, combined with a flatter inland area that is crossed by a small stream that leads to the formation of inclined river banks. Furthermore, the site includes a series of exposed slope sections alternating with gully-outcrop forms with a height between 2 and 10 m (Gonzalez-Ollauri & Mickovski, 2021), which are visible in Figure 5.2. The northern part of the bay has a small tarmac-surfaced access road, which divides the slope in an upper and a lower part there. Along the crest of the slope, twelve houses are located, as well as a grassed public footpath offsetting the houses from the actual slope. A branch of the footpath leads to a mid-slope structure - a former pumping station used in the past to capture water from the slope (Gonzalez-Ollauri & Mickovski, 2021). Figure 5.2 captures the exposed slope sections with outcrops forms well from drone footage.

Shallow (ca 600mm) and well-drained soils can be found within the study area resting on top of sedimentary bedrock. The soil along the slopes is a cohesive mixture of silty sands with contents of clay. It is partly covered by gravel and rock but low vegetational cover and less organic matter which explains the instability of the slopes in heavy rain or high waves (Operandum Project, 2022). The vegetation cover is dominated by herbaceous weeds and grasses, riparian trees and agricultural crops of wheat and barley. The sea has limited influence on the vegetation, because south-westerly winds prevail. Different soil mass wasting episodes (landslides and erosion) have been reported on the site, mainly associated with long periods of rainfall (Gonzalez-Ollauri & Mickovski, 2016). Several properties, the access road to the harbour, plants and wildlife are at risk due to landslide and coastal erosion (Tardío & Mickovski, 2016).

Figure 5.4 **(a)** and **(c)** show failure zones, that are easily identifiable by eye, presenting exposed bare ground or areas of sparse vegetation.

(a) Northern part of the bay

(b) Southern part of the bay

Figure 5.2: Drone footage of the Catterline Bay, taken by Graeme Davidson in May 2016.

At the study site several landslide events occurred, which are revealed by hollows, gullies, outcropping

rock mounds, bulges and areas of ongoing creep. Based on detailed site inspection, some mechanisms of failure are discovered by Gonzalez-Ollauri and Mickovski (2021). Translational slips with 0.5-1.0 m depth are seen at the slope above the access road. On the slope below the access road, deeper slides (1.0 -2.0 m depth) are reported, which may be connected to the stability and retention capacity of the seawall defence (Gonzalez-Ollauri & Mickovski, 2021). In Table 5.1 an overview of historical failure events is given. In Figure 5.1 the location of the sea defence wall is depicted, where the failure in 2013 happened. The failure in 2020 took place mid-slope at the height of where the access road and pier come together. The landslide in 2021 is also shown in Figure 5.4**(c)** with the location at B in Figure 5.3.

Table 5.1: Record of recent failures on the slopes. Information from Gonzalez-Ollauri and Mickovski (2021).

Year	Event	Consequence
2013	Storm surge, erosion of the slope toe	Breached seawall defence
2020	Slope failure initiated mid-slope after a period of continuous rainfall	Road blockage
2021	Slope failure initiated below the road on the southern extent of the access road	Undermined and exposed existing road drainage infrastructure

In Figure 5.3 different layers at the study site are labelled to give an overview of what structures are present. Figure 5.3 also indicates landslide zones as found in the paper of Gonzalez-Ollauri and Mickovski (2021). These zones will later be used in a comparison with erosion zones from this research. Furthermore, the left map shows 4 locations, for which more detailed figures are created.

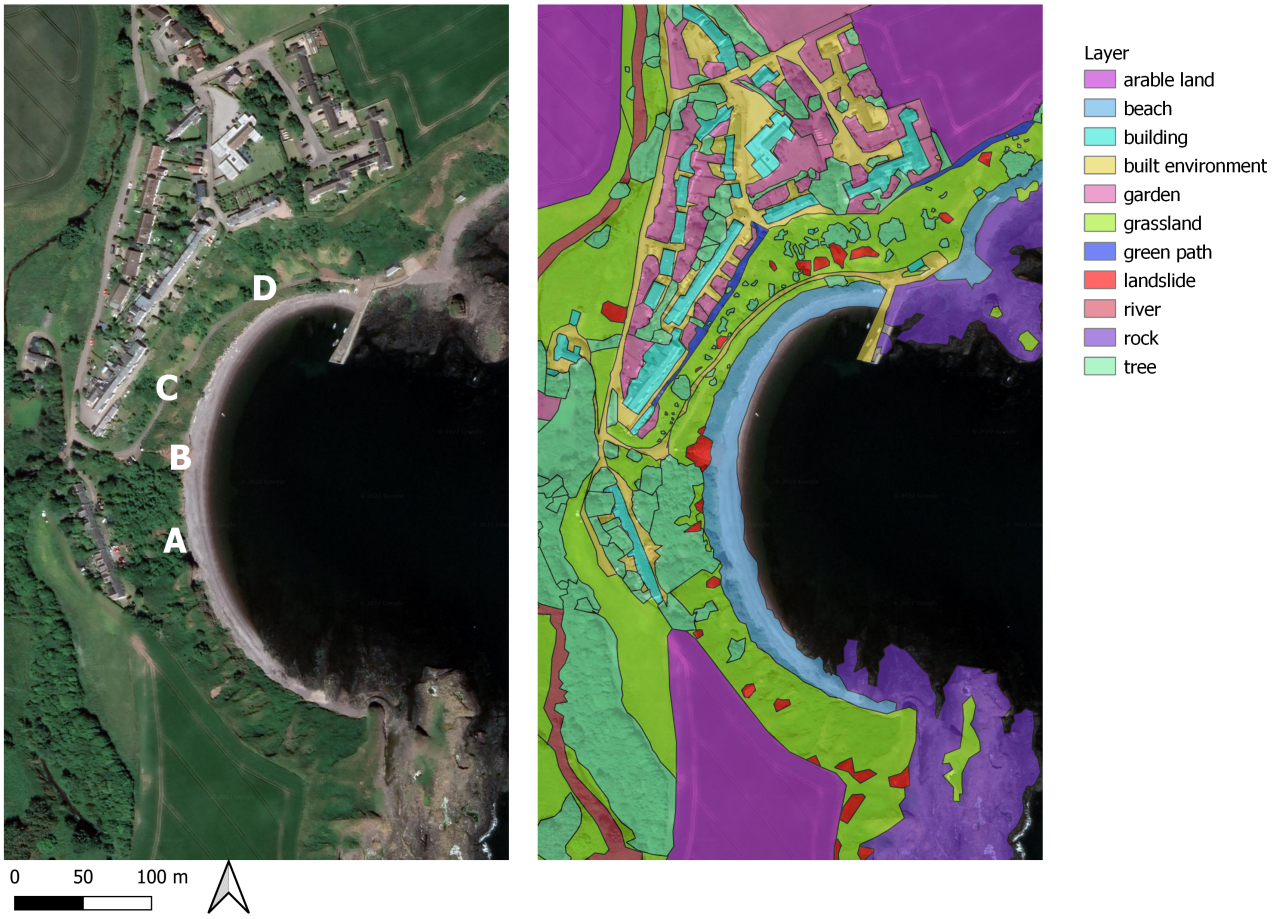

Figure 5.3: Left: 4 locations are highlighted, which are shown as a photograph and as point cloud data (coloured with intensity) in Figure 5.4. Satellite image from Google Satellite. Right: different layers at the Catterline Bay. In red, landslides are highlighted.

(a) An erosion zone, located at A in Figure 5.3

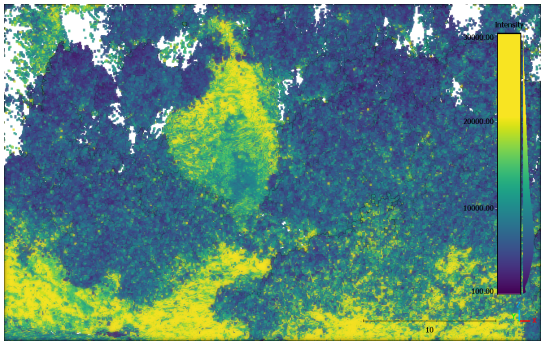

(b) The bare soil is clearly distinguished with higher intensity values, whereas vegetation has much lower intensity values.

(c) A landslide zone, located at B in Figure 5.3.

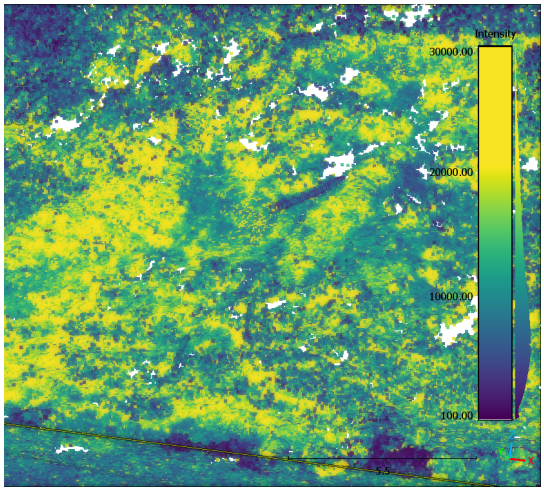

(d) In both figures, the pipe is clearly visible.

(e) Live pole drain, located at D in Figure 5.3

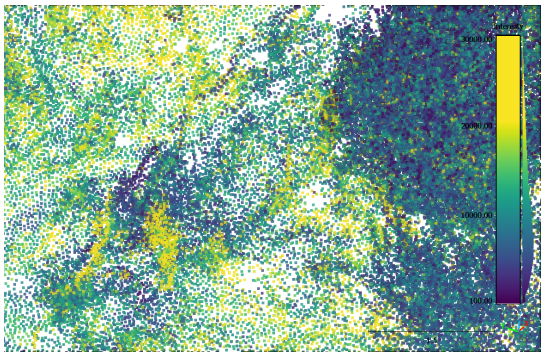

(f) Point cloud snapshot: intensity

(g) Cribwall, located at C in Figure 5.3

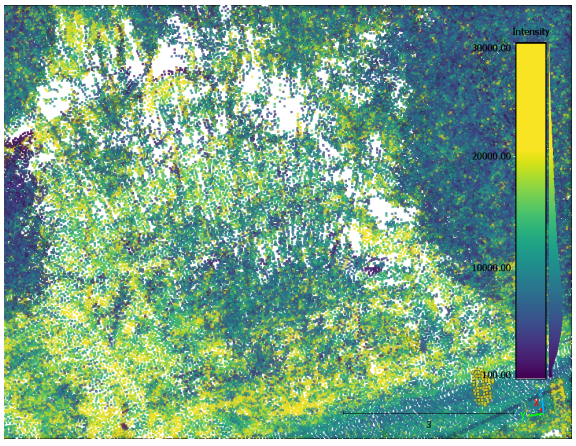

(h) Point cloud snapshot: intensity

Figure 5.4: Left figures: pictures taken by the author in April 2022, right figures: point cloud with intensity. Yellow indicates high intensity, whereas blue indicates low intensity. It can be seen that the ground points have higher intensity than vegetation points.

5.2. Terrestrial Laser Scanning in Catterline

This section introduces the used laser scanner, presents how to carry out a TLS survey and describes the available data from terrestrial laser scanning.

In this particular research, the Leica ScanStation P40 Laser Scanner is used, which is shown in Figure 5.5. This is a Time-of-Flight laser scanner. The operating range of the scanner is up to 270m. The field of view is $360°$ horizontally and $290°$. The scanner has a scan rate up to 1 million points per second. It has an on-board camera, which allows to assign true-colour RGB values to points. The accuracy is 3 mm at a distance of 50m ("Leica ScanStation P30/P40", 2015). In Table 5.2 some relevant specifications are listed.

Figure 5.5: The Leica P40 Laser Scanner on top of a tripod. This specific model is used during the field work acquiring the point clouds. Image from CR Kennedy.

Table 5.2: Specifications and system accuracy of the Leica P40. From "Leica ScanStation P30/P40" (2015). The accuracies are all valid at 78% albedo.

Specification	
Type	Time-of-Flight with WFD Technology
Range	180 m (18% albedo), 270 m (78% albedo)
Field of View	Horizontal: $360°$, vertical: $290°$
Scan rate	Up to 1,000,000,000 points per second
Accuracy of single measurement Range accuracy Angular accuracy 3D position accuracy	 1.2 mm + 10 ppm over full range 8" horizontal; 8" vertical 3 mm at 50m; 6 mm at 100m
Target Acquisition	2mm standard deviation at 50m

When setting up a survey, it is important to start with a clear idea of the area and its possible difficulties, such as obstructions, that may cause occlusions. To ensure a complete coverage of the study area, it is important to select suitable scanning positions with care. In order to minimise the amount of missing data due to occlusion, scans are collected from different angles and heights. Figure 5.6 shows how objects can cause shadowing and how including different scanning positions overcomes this problem.

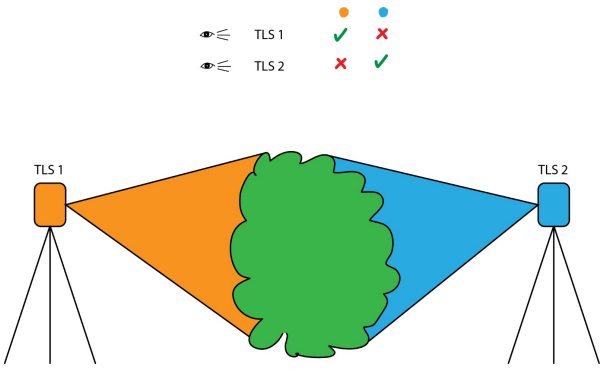

Figure 5.6: Vegetation can cause occlusions. By using multiple scanning stations, occlusions can be prevented.

Overlapping scanning directions are chosen in order to minimise shadows and obstruction by vegetation in the sloped terrain. In order to tie scans accurately together, three reflector targets with known dimensions are placed into the scanned scene. These are used in the post-processing stage as tie points for the geo-referencing process of the combined point cloud (Kuhn & Prüfer, 2014). The targets are placed at various elevations and distributed spatially as evenly as possible in order to obtain a spatially uniform registration error (Lague et al., 2013).

When scanning on the cobble beach in Catterline, the tides are heavily influencing the possible scan locations. During high tide, there is almost no beach left, which is especially a problem on the southern part of the bay. Therefore, scanning on the beach should be planned during low tides. Because the Catterline Bay is too large in dimensions to scan during one day, the scans are done on two or three consecutive days. On the first day, the path down to the beach is used for the scanning locations. On the second day, the scanning locations are located on the beach. These two days can be connected using a few stable targets, which are left in the field during the night. These stable targets were printed on paper, unlike the reflector targets, and taped on the door of the boathouse, a mailbox on the pier and an old pulley used for boats. After scanning at different locations, the point clouds of all scans from these two days (scan-to-scan registration) were registered using the Leica Cyclone software in order to form a combined point cloud for one acquisition timestamp. This scan-to-scan registration can be easily done based on the centre coordinates of the three reflector targets, which are scanned accurately with the Leica P40. The final point clouds are exported from Cyclone to a so-called .E57 file, which can be further processed using the methods from Chapter 4. To be able to work with the two point clouds, both point clouds are subsampled to 50mm. In Figure 5.7, an example of the reflector target is shown, as well as how it looks like in the point cloud, coloured with intensity values.

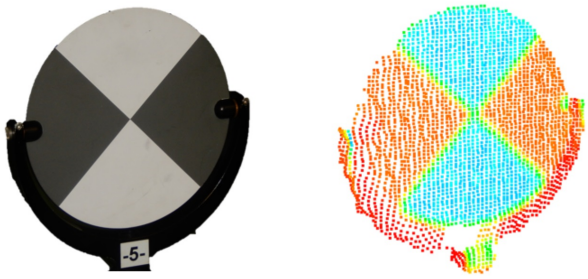

Figure 5.7: Left: image of a black and white target, right: scanned point cloud of the target (intensity coloured). Image from Janßen et al. (2019).

The available field surveys with TLS at the Catterline Bay were carried out in October 2019 and April 2022. In October 2019, a complete and accurate point cloud was acquired. During this survey, some of the NBS were already installed. This point cloud was created from 29 registered scans. Figure 5.8 shows the 29 scan positions in the acquired point cloud. In April 2022, another data acquisition with Leica ScanStation P40 was performed. This resulted in a point cloud created from 41 terrestrial laser

scans. For the 2019 and 2022 point clouds, the scans were taken on two or three consecutive days respectively. Table 5.3 includes some information on the acquired point clouds.

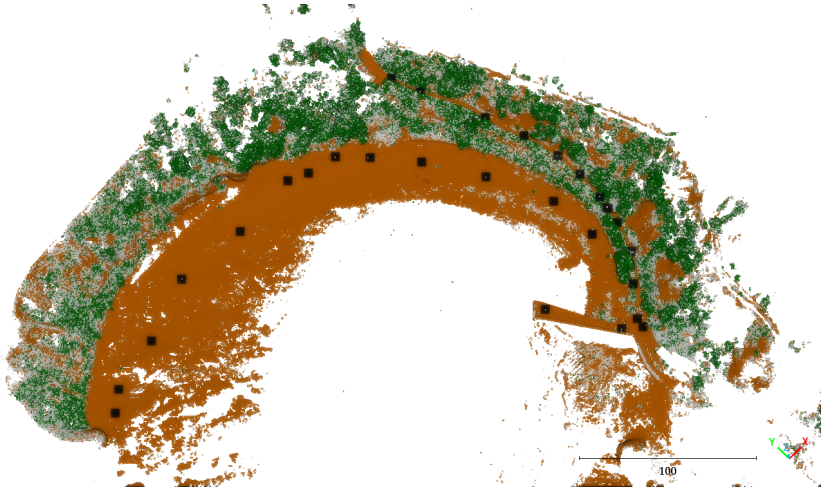

Figure 5.8: The 29 scanning positions in 2019 are shown in black.

Table 5.3: Available point clouds in .E57 format from TLS campaigns

Acquisition date	File Size (GB)	Number of scans	Number of points
2019, October 16 and 17	10.6	29	581,492,611
2022, April 18, 19 and 20	42.4	41	2,298,123,242

Although there was well thought of possible occlusions during the fieldwork, some shadowing could not be prevented, because only limited locations were accessible to use as a scan position. At the access road and on the cobble beach it was possible to set up the laser scanner. The shadowing by vegetation led to gaps in points at some places. Figure 5.9 points out some important spots with black boxes. The occlusions are mainly caused by vegetation in combination with gully-like slope, which makes it difficult to obtain points at the upper part of a gully if vegetation is obstructing the view at the lower part of the slope.

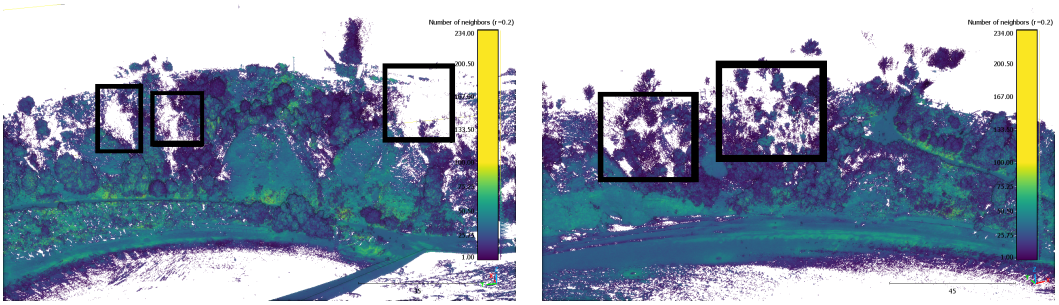

(a) Occlusions above the access road, caused by vegetation

(b) Occlusions in the middle part of the bay. On the right a part of the access road is visible.

Figure 5.9: Occlusions by vegetation on the slope in the 2022 data set are shown within the black boxes. The number of neighbours within a radius of 20cm for each point are visualised with the colourmap.

5.3. Processing Software

To process and analyse all data, the following software is used:

- **Leica Cyclone**: software used to register the point clouds of all individual scan sets (scan-to-scan registration) and to form a combined point cloud.
- **CloudCompare**: an open source 3D point cloud processing software, including many advanced algorithms (registration, resampling, scalar fields handling, statistics computation and classifications). At http://danielgm.net/cc/ more information can be found.
- **QGIS**: an open source geographical information system (GIS) application that supports viewing, editing, printing and analysing geospatial data.
- **Python**: an open source programming language. In the scripts multiple libraries and packages are used.
- **Matlab**: a programming language and numeric computing environment. To be able to use Matlab, a license is needed.

The scan-to-scan registration in Leica Cyclone was performed on a laptop of the TU Delft. All other processing steps and computations were performed on a personal laptop (HP Zbook Studio G5) with an Intel Core i7-9750H (hexa-core) and 16 GB memory.

6

Results

The methods described in Chapter 4 are applied on the point clouds from 2019 and 2022. This chapter contains results from the registration in Section 6.1, ground points classification in Section 6.2 and topographical data layers in Section 6.3. Furthermore, erosion and non-erosion zones are identified and then characterised by some statistics in Section 6.4.

6.1. Registration

To co-register the point clouds from 2019 and 2022, the 2022 point cloud is first manually aligned and then Iterative Closest Point (ICP) is applied. Manual alignment is needed to prevent that the ICP algorithm gets stuck in a local optimum. Sections of the final registration result are shown in Figure 6.1. For various segments with stable points, the root-mean-square error (RMSE) of the registration between the two point cloud acquisitions from 2019 and 2022 is calculated. Over eight segments of chimneys, lampposts, a part of the pier and a wall and a roof, an average RMSE of 0.033 m is found. Because of the relatively large size of the study area, this RMSE is considered acceptable.

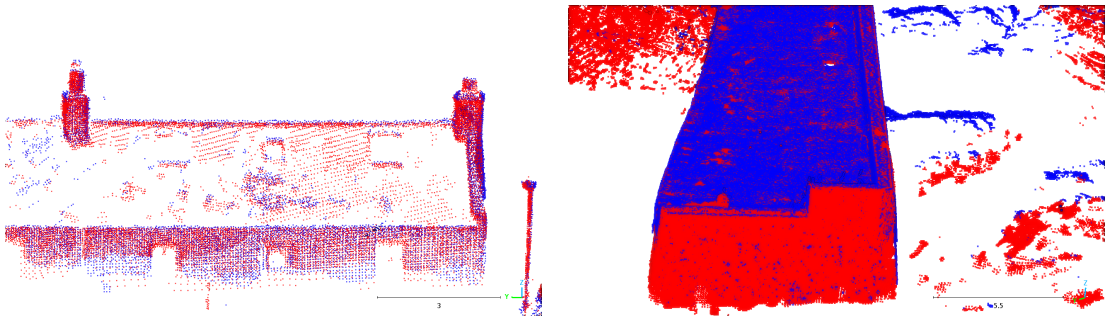

(a) Chimneys from houses and a lamppost

(b) Part of the pier

Figure 6.1: Points that are assumed stable, used to calculated the registration error between the 2019 and 2022 point clouds. In red, the 2019 point cloud. In blue, the 2022 point cloud.

Table 6.1: Registration RMSE for segments with points that are considered stable

	RMSE (m)
Lamppost	0.032
Chimney 1	0.045
Chimney 2	0.042
Chimney 3	0.038
Chimney 4	0.026
Pier	0.031
Roof	0.022
Wall	0.026
Average	0.033

6.2. Ground Classification

The classifier is trained on the training objects from the point cloud from 2022. In Figure 6.2 the training objects are shown. 2,142,977 ground points and 4,068,607 non-ground points are selected in the training data set. In case that appearance frequencies are not equal for the two classes, it will affect accuracy metrics. This problem is solved by applying random subsampling on both data sets to acquire an equal amount of core points for both data sets. Thus, balanced data is used for training the classifier.

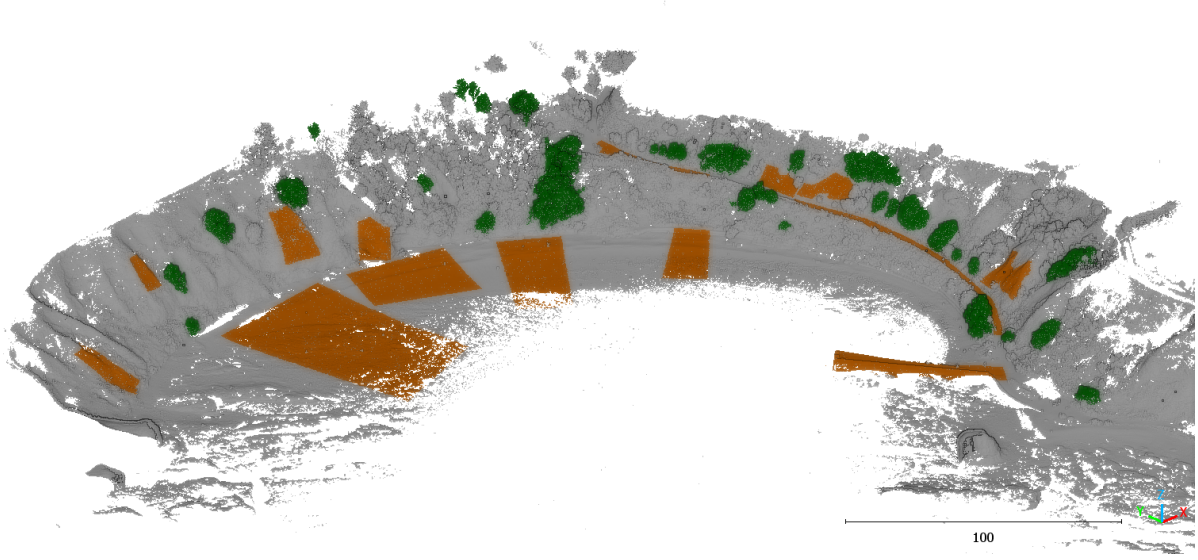

Figure 6.2: CANUPO Training data from the 2022 point cloud. In green all training objects for non-ground points (4,068,607 points). In brown all training objects for ground points (2,142,977 points).

After assessing the balanced accuracy ba and Fisher Discriminant Ratio fdr, which were introduced in Section 4.2, for different sets of scales, the scales $[0.01, 0.26, 0.51, 1.26, 1.51, 1.76, 2.01]$ (a linear ramp with min $= 0.01$, max $= 2.01$, step$= 0.25$) gave the best statistics with $ba = 99.4\%$ and $fdr = 21.9$. All other sets of scales had a lower balanced accuracy and Fisher Discriminant Ratio. The maximum number of core points was set to $100,000$, because Girardeau-Montaut (2019) states that 10,000 should be enough in most of the cases. However, because the scene is larger than scenes classified in examples, the chosen number of core points was set at 100,000. In Table 6.2 quantitative performance results of the classifier are summarised.

Table 6.2: Quantitative results on 2022 data set of separating non-ground from ground using CANUPO.

		Precision (%)	ba (%)	fdr
Training set	Ground	99.5%	99.4%	21.9
	Non-ground	99.3%		
Test set	Ground	94.7%		
	Non-ground	94.3%		

The classifier is used to classify the 2019 and 2022 point clouds. In Figure 6.3 the result of classifying the 2022 point cloud is visualised. Green represents non-ground and brown ground. The grey points in Figure 6.3 are points for which the class confidence was not above 95% and therefore, no class was assigned to these points. In total, 13,174,153 points were classified as ground and 10,241,900 as non-ground.

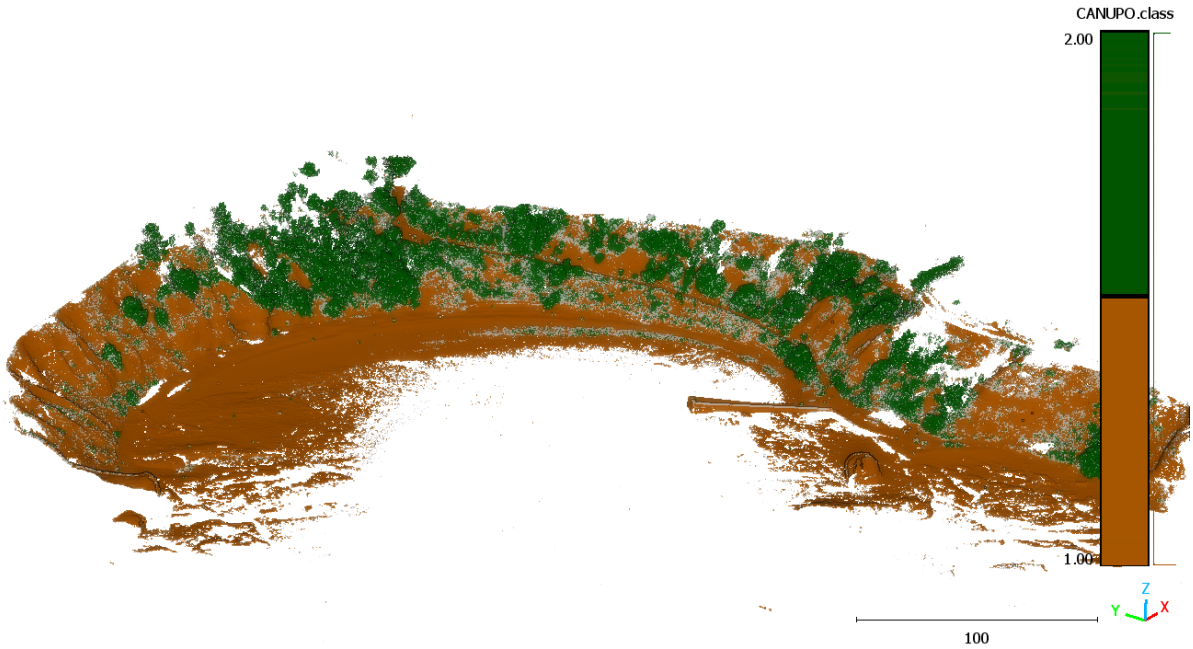

Figure 6.3: CANUPO Classification 2022 data. 1 is given to all points classified as ground, 2 to all points classified as non-ground.

A test data set was created, where ground and non-ground points were manually separated into classes by visual inspection using field knowledge from photos. Although the test data set was created thoroughly as explained in Section 4.2, the test data set will still have some inevitable bias, because it only contains points of which the supervisor was to some degree sure to which class the points belonged. 772,721 non-ground points were selected for the test data set, of which 728,985 points were classified as such by the classifier, yielding a 94.3% accuracy. From the 712,054 ground points in the test data set 673,971 points were correctly classified, which gives a 94.7% accuracy. These statistics are also summarised in Table 6.2.

Figure 6.4 gives a closer look at the classified point cloud, such that some details are visible. Some willows and small vegetation can be distinguished, as well as a tripod and the fence with some poles. From Figure 6.4 it is clear that the classifier has difficulties with transitions from vegetation to ground. The classification result could be refined, when the original unsubsampled point cloud is used.

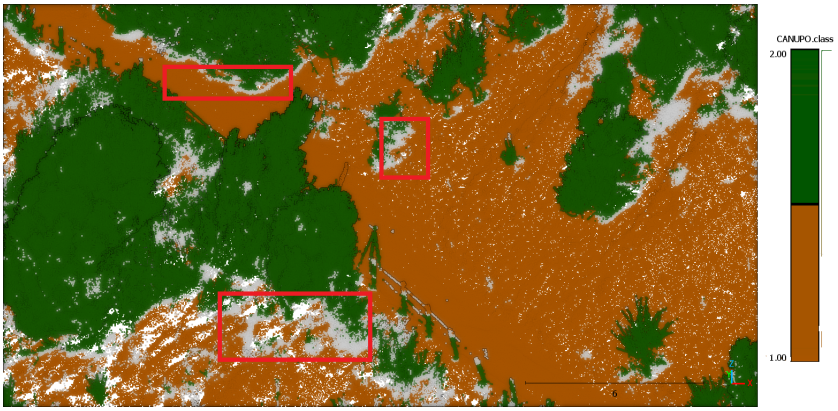

Figure 6.4: CANUPO has difficulties with vegetation near the ground. Grey indicates unclassified points, because their class confidence is lower than 95%. The red boxes indicate difficulties close to the ground.

6.3. Maps

In this section some maps from static quantities are shown. Here only results from 2022 are presented, but in Appendix C also the maps from 2019 are shown. In Figure 6.5 the DTM of 2022 of the full bay is shown. From the classified point cloud, the ground points are extracted. The points are rasterised, such that a DTM is created. The spatial resolution of the raster is 5cm. For all derived layers, the spatial resolution is also 5cm. From the DTM, the slope, aspect, Topographic Wetness Index (TWI) and Terrain Ruggedness Index (TRI) were calculated in QGIS.
In Figure 6.7 a map with the slope is shown. At the left side of the upper part, a bulge can be seen. This is an actual salience in the field (see Figure 6.6**(a)**).

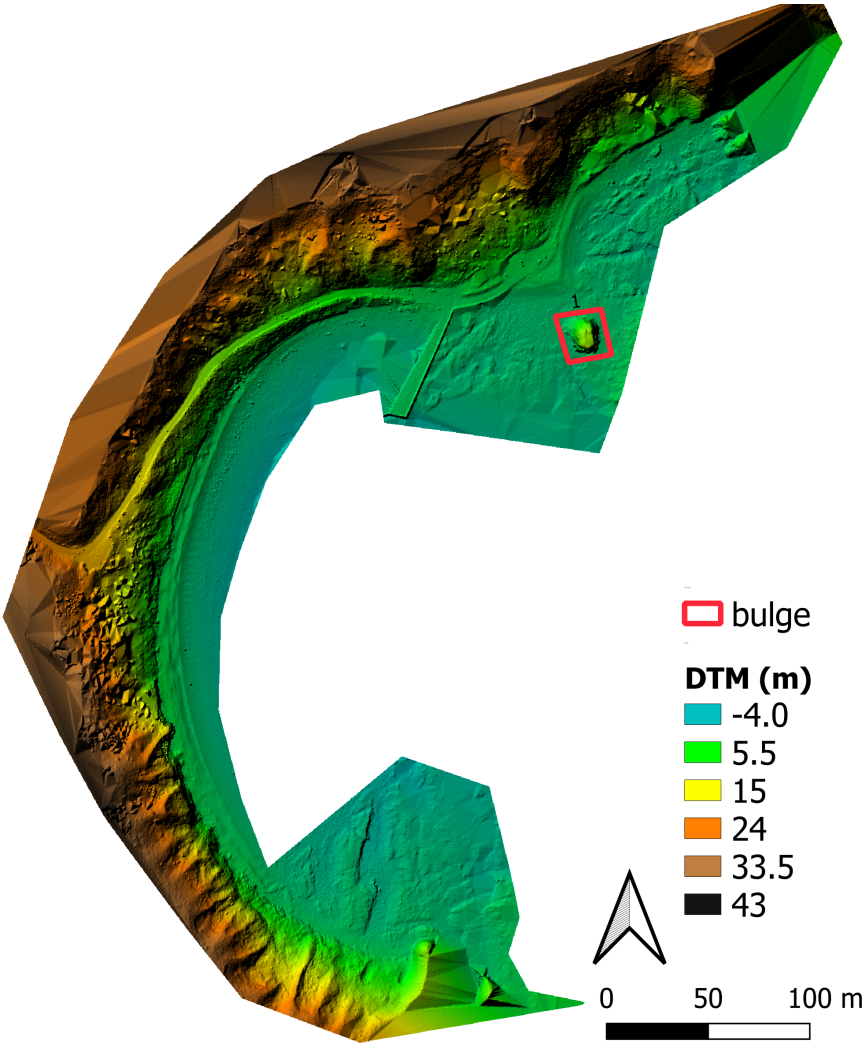

Figure 6.5: Digital Terrain Model 2022. In red, the bulge from Figure 6.6**(a)** is outlined.

(a) The bulge. Photo taken during fieldwork trip in 2019, by A. van Natijne and T. Bisschop.

(b) Outcrop with very steep slopes. This outcrop is indicated in Figure 6.7 with the pink box. Photo by the author, April 2022.

Figure 6.6: Saliences in the scene

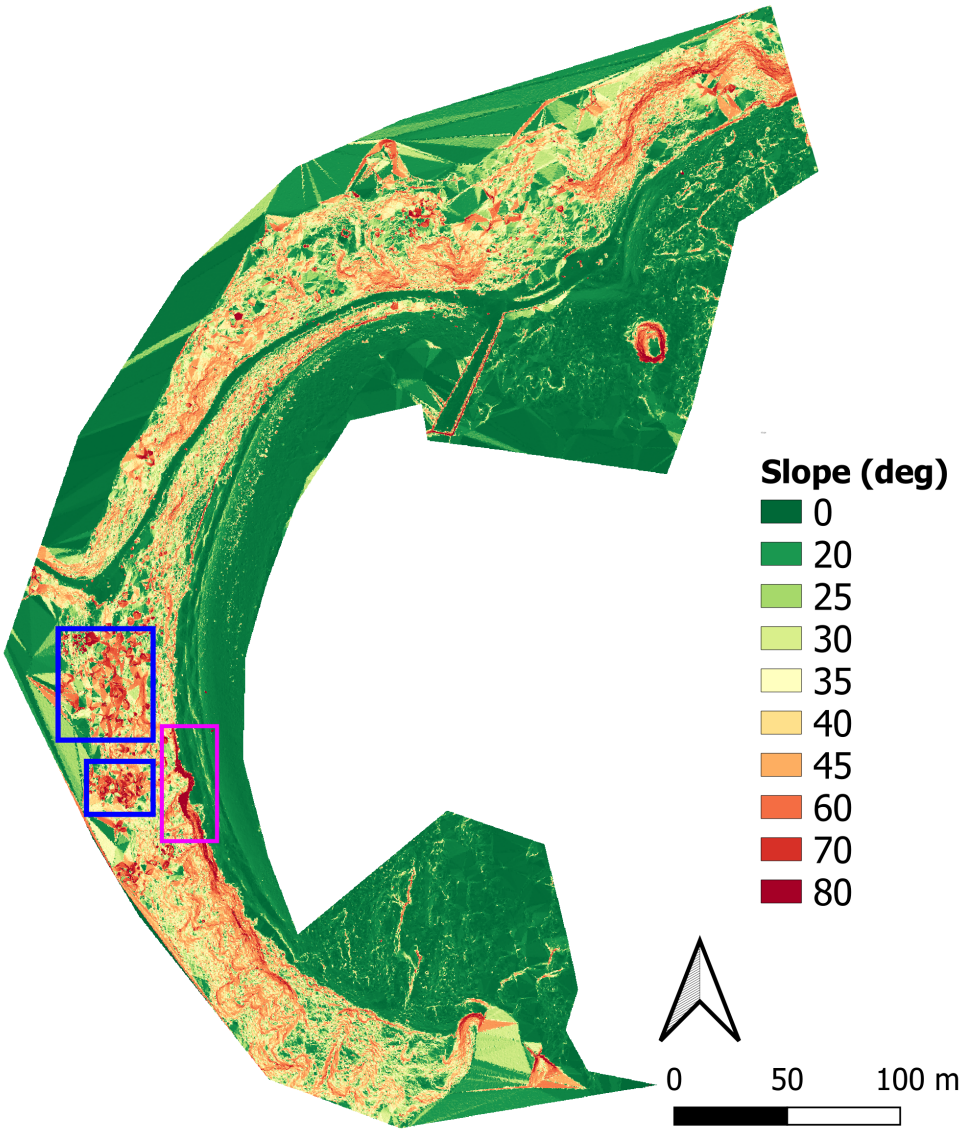

Figure 6.7: Map of the slope, 2022. In pink the outcrop from Figure 6.6**(b)** is outlined. The blue boxes outlines display zones with high uncertainty in the slopes because of dense vegetation.

The slope map for 2022 is displayed in Figure 6.7. In blue, zones with dense vegetation are featured. In these zones it is hard to obtain ground points. Therefore the DTM has a large uncertainty and looks coarse here. In the pink zone, the slope has the highest values. This is in agreement with the actual setting, because an outcrop with very steep slopes is found at this place, shown in Figure 6.6**b**.

In Figure 6.8 a map of the Topographic Wetness Index (TWI) is shown. Some water drainage channels are revealed, indicated with higher values of TWI. The access road is also clearly distinguishable with high values of TWI.

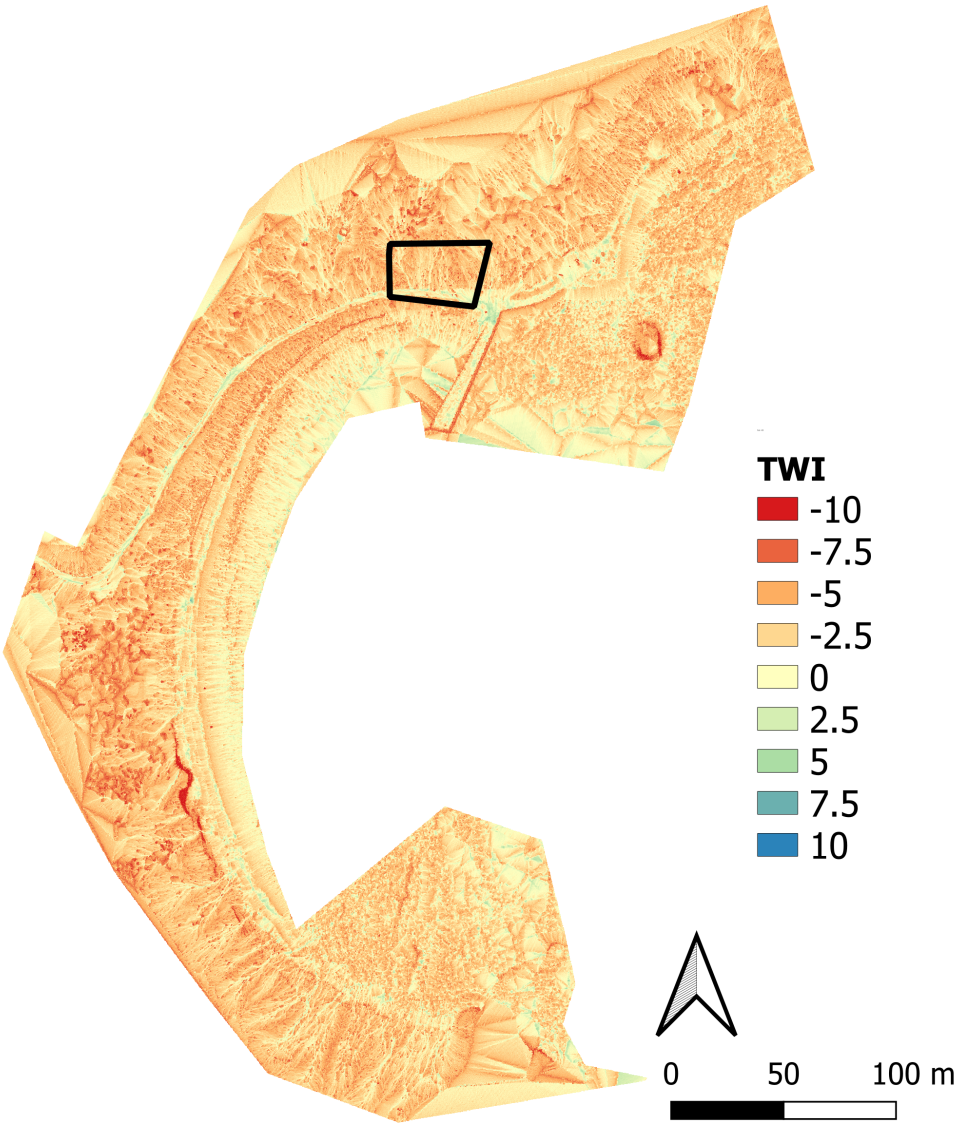

Figure 6.8: Topographic Wetness Index 2022

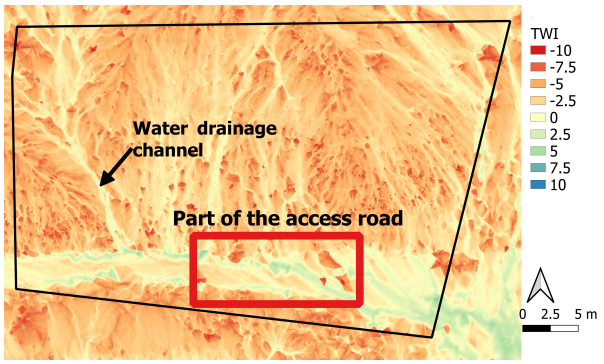

Figure 6.9: A zoomed section of the TWI map: the black box in Figure 6.8. Here a water drainage channel and a part of the access road are clearly indicated with high TWI.

The Terrain Ruggedness Index (TRI) is displayed in Figure 6.10. In this map sudden height differences are indicated with high TRI values. For example, scarps of beginning landslides can be detected by looking at this map. This finding will be highlighted with detailed sections of the TRI map in Section 6.4.

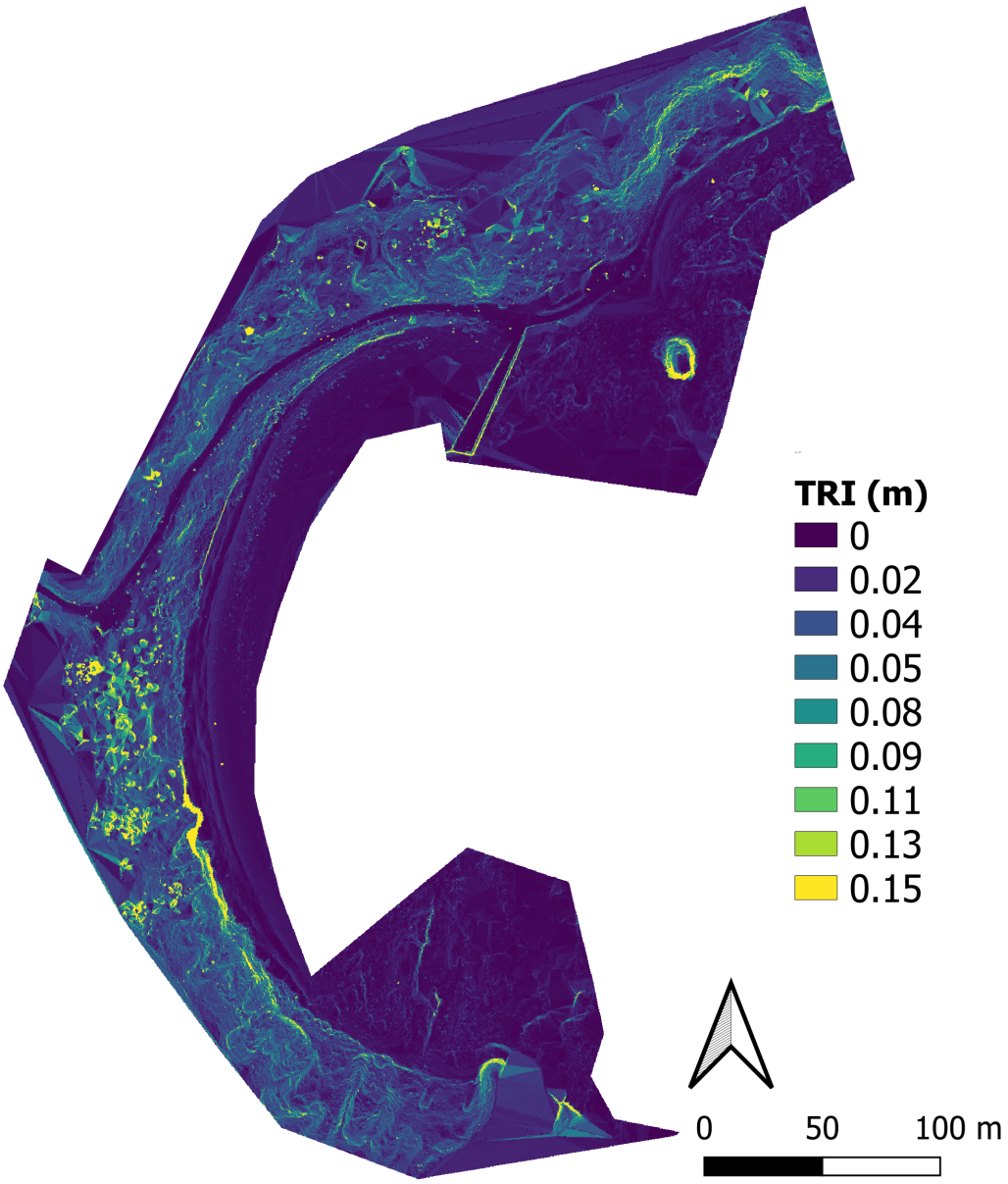

Figure 6.10: Terrain Ruggedness Index 2022

In Figure 6.11 the vegetation height of 2022 is visualised. Also some locations are depicted, which will be discussed in more detail in Section 6.5.

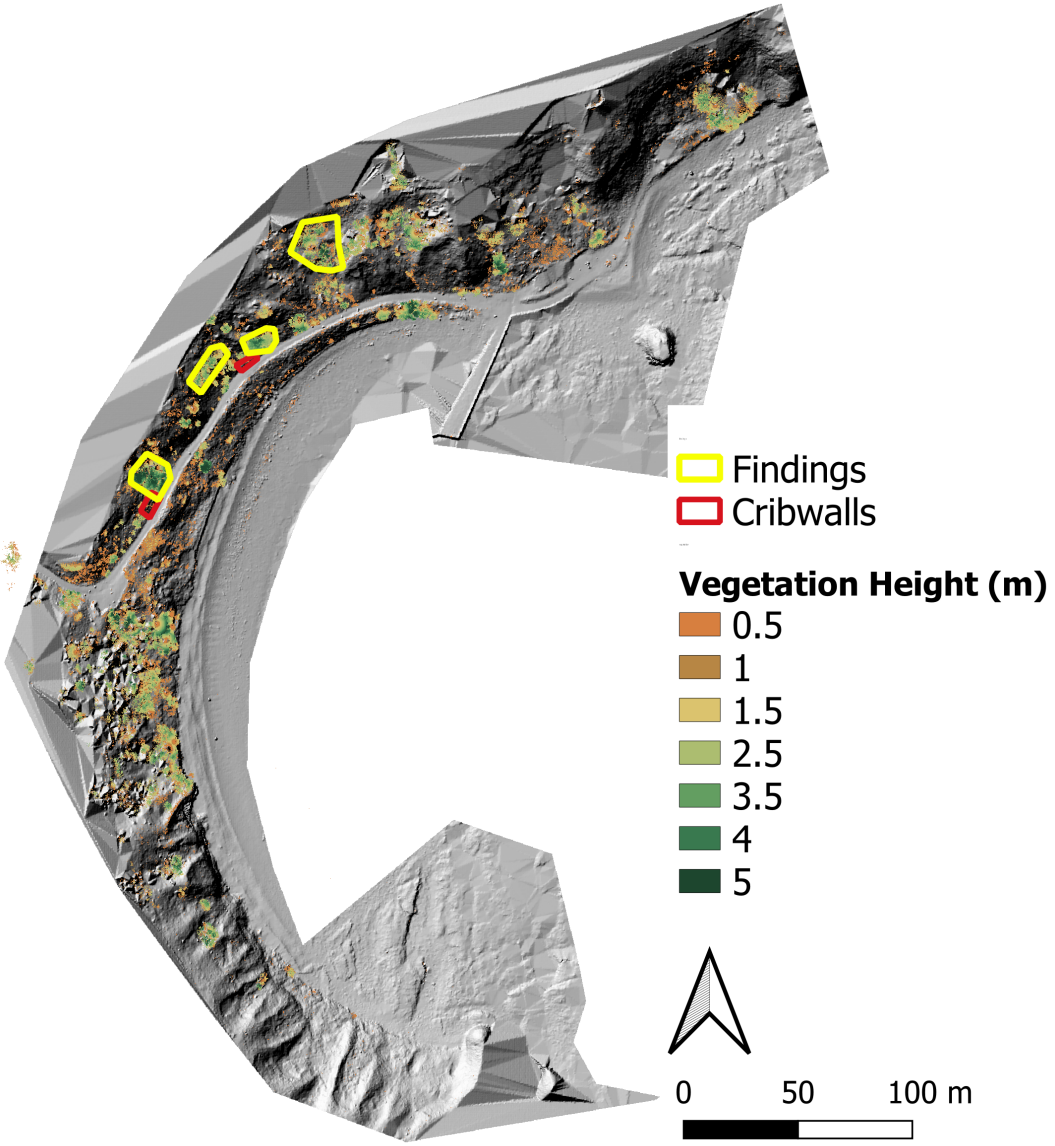

Figure 6.11: Vegetation Height in 2022 with some locations indicated, which are displayed in more detail in Figure 6.24.

The Multiscale Model to Model Cloud Comparison (M3C2) is applied on the ground points from 2019 and the ground points from 2022. Additionally to the proposed settings in Section 4.5, also the global registration error is set to 0.033m, as found in Section 6.1. In Figure 6.12 the M3C2 result is visualised in the 2022 point cloud with ground and non-ground points in brown and green. The result shows only the significant changes, which is based on a Level of Detection at 95% ($LOD_{95\%}$). The Level of Detection can vary spatially. Red points indicate a decrease in height, which can point to a depletion zone, whereas blue points indicate an increase in height, pointing to for example accumulation of material. Each M3C2 distance comes with an uncertainty, which depends among other on the the local point cloud roughness of the two point clouds. Figure 6.13 displays the uncertainty of the M3C2 distances. Most uncertainties vary between 4 and 6cm (95%).

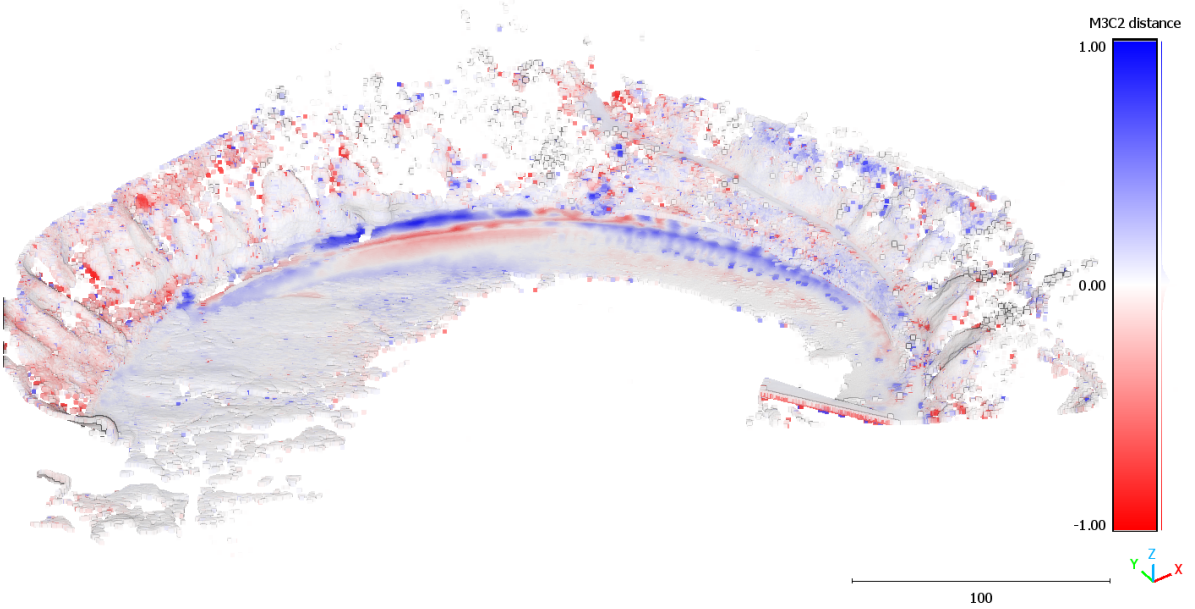

Figure 6.12: M3C2 distances [m] visualised in the point cloud.

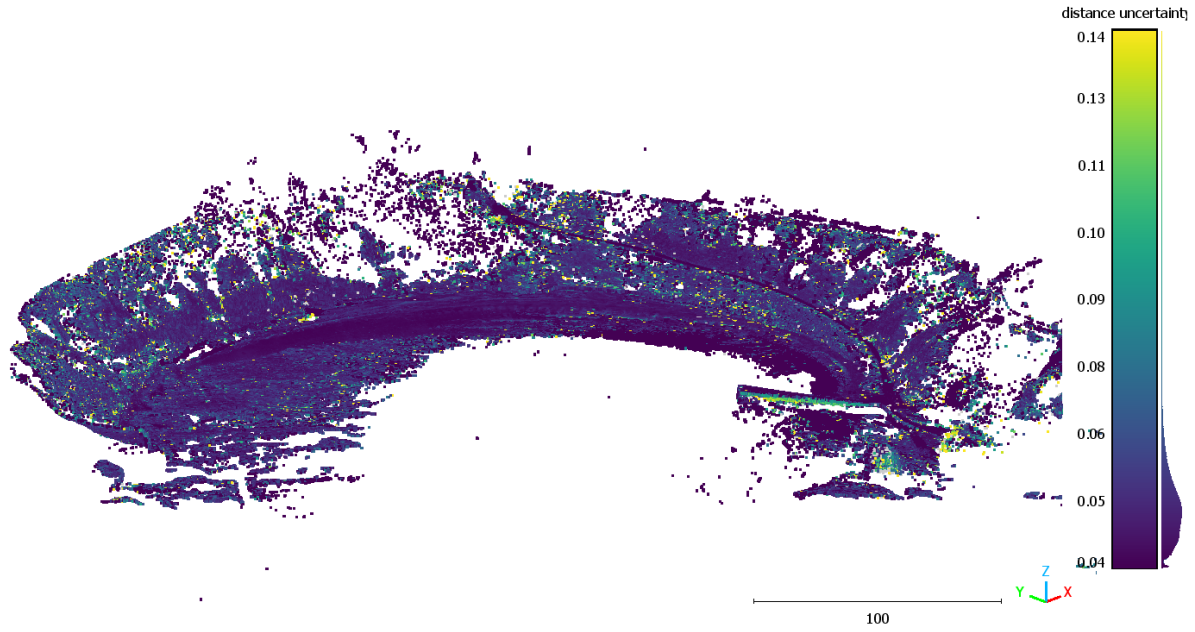

Figure 6.13: The distance uncertainty [m] for the M3C2 distances.

To grasp how these differences between the two point clouds look, a cross section of the landslide zone C from Figure 5.3 is given in Figure 6.14. In the upper part, material is deposed, whereas in the lower part some accumulation of material is seen.

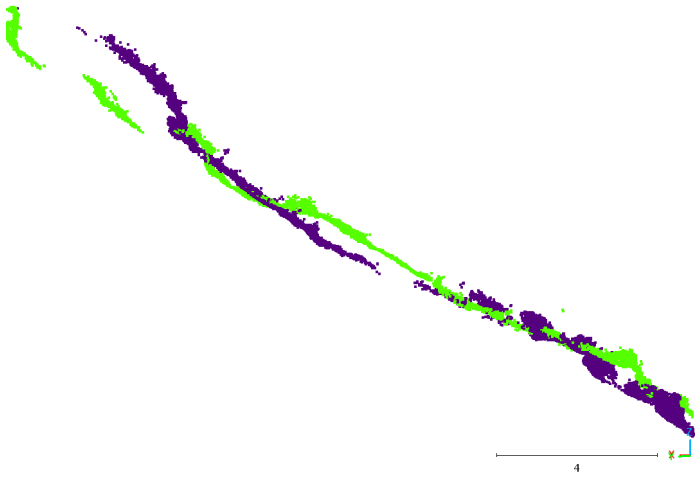

Figure 6.14: Cross section of a landslide zone. This is the landslide zone in Figure 5.4**(c)**. The green points are from the 2022 point cloud and the purple points from the 2019 point cloud.

6.4. Identification of Erosion Zones

From the M3C2 result, zones with a clear change were selected. A clear change is defined as a group of points with high positive or negative M3C2 values. An area with a clear pattern of negative M3C2 distances is marked as a possible erosion zone, because it points to depletion of material. Sometimes, a group with negative M3C2 distances is found together with a group of positive zones nearby, which indicates accumulation of material. These are grouped together into one zone.

Combining this with the terrain ruggedness index (TRI), some clear scarps could also be seen in the erosion zones: a scarp is in most cases indicated with high values of TRI. In Figure 6.15 five erosion zones and one of the four stable zones are visualised with the TRI and the M3C2. Erosion zone 5 is the area of the landslide, that occurred in 2021 (see Table 5.1). Figure 6.17 shows the full area, where the location of each zone is indicated. By comparing photos of the author from April 2022 with these zones in Figure 6.16, the erosion zones are validated: if the selected zones also showed some signs of erosion on the photos, such as visible scarps, then this gave a confirmation.

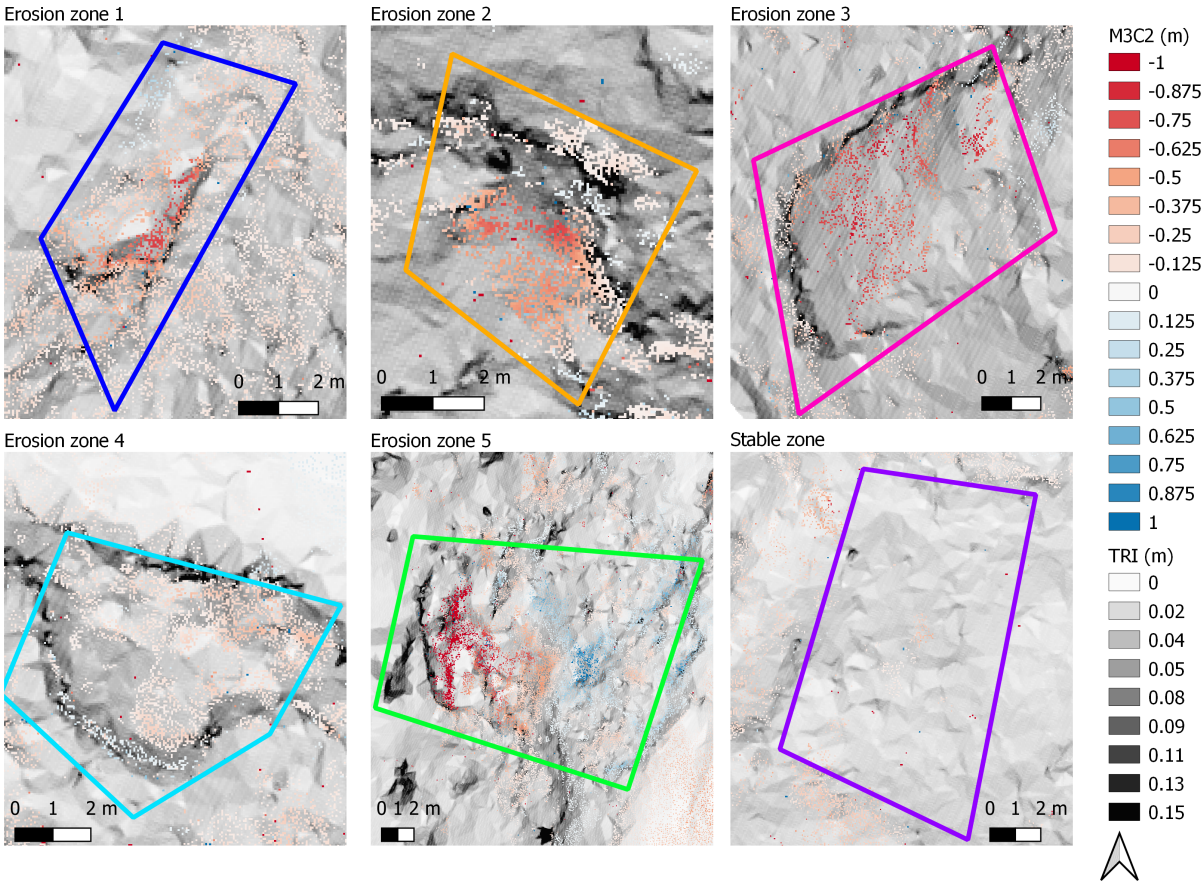

Figure 6.15: M3C2 distances and TRI (2022 data) at 5 erosion zones and one of the 4 stable zones. The TRI is visualised with a grey colourbar, such that the M3C2 distances are clearly visible.

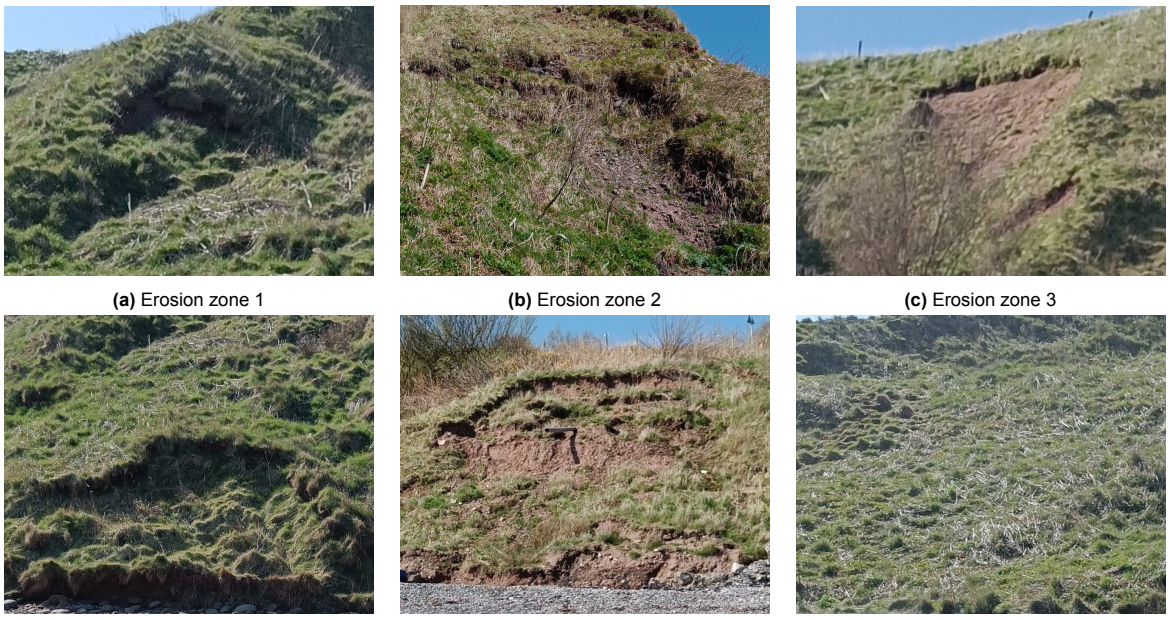

(a) Erosion zone 1 **(b)** Erosion zone 2 **(c)** Erosion zone 3

(d) Erosion zone 4 **(e)** Erosion zone 5 **(f)** Stable zones

Figure 6.16: All zones from photos taken by the author. The orientation of the photos is different than in Figure 6.15.

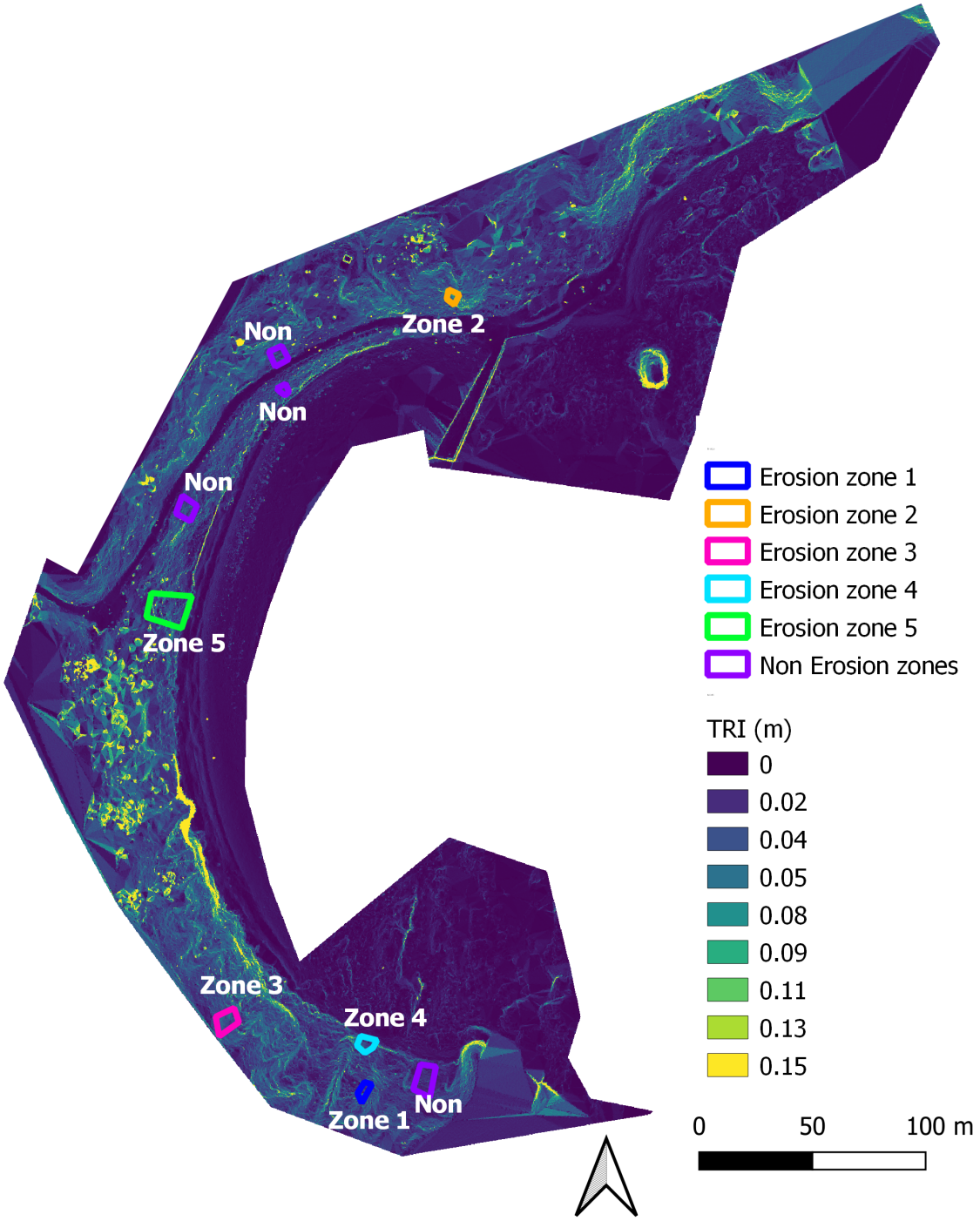

Figure 6.17: Locations of the five erosion zones and four stable zones with TRI (2022 data) visualised.

A closer look at the M3C2 distances for each selected zone is taken by the creation of histograms and calculation of some statistics. From the histograms in Figure 6.18 it is clear that the changes in the erosion zones are mostly between -1 and +1 m. However, most values are negative in these zones. As expected, the four stable zones have mostly M3C2 values close to 0. Erosion zone 5 has a different distribution than the other erosion zones. The spread of M3C2 distances is larger, with values between -2 and 2 m and also positive values occur much more. The positive values indicate the deposition area at the bottom of the area (see Figure 6.16**(e)**). In erosion zone 5, a landslide happened in 2021 (see Table 5.1). In very short time, the movement took place. Here, the erosion is classified as rotational movement. The other erosion zones are very shallow, translational landslides.

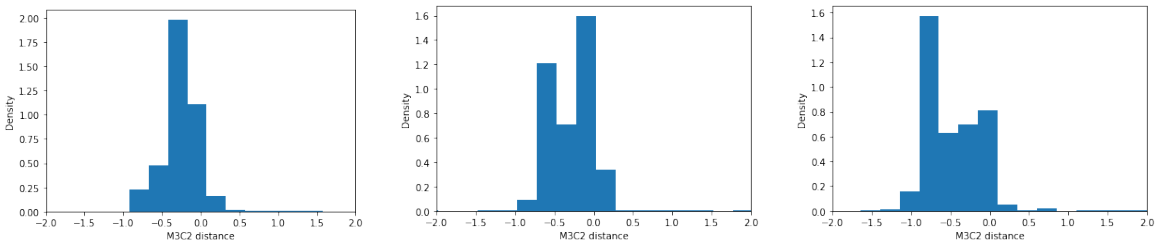

(a) Erosion zone 1. Mean: -0.26m, std: 0.28m

(b) Erosion zone 2. Mean: -0.28m, std: 0.32m

(c) Erosion zone 3. Mean: -0.48m, std: 0.48m

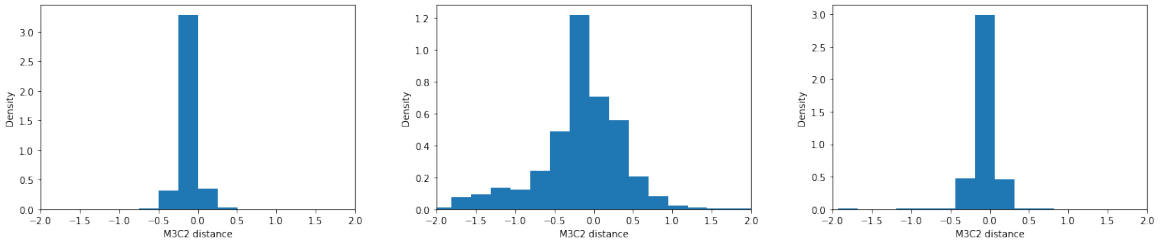

(d) Erosion zone 4. Mean: -0.12m, std: 0.14m

(e) Erosion zone 5. Mean: -0.16m, std: 0.61m

(f) Stable zones. Mean: -0.08m, std: 0.33m

Figure 6.18: Histogram of the M3C2 distances in the depicted zones.

Although, the type of landslide is not completely similar for every erosion zone, the five erosion zones will be grouped together for further analysis instead of treating each zone individually. This gives a more generalised view on erosion zones compared to non-erosion zones. Appendix D presents the analysis of all individual erosion zones. Erosion zone 1 till 5 are referred to as erosion zones. In Figure 6.19 all M3C2 distances of the erosion and non-erosion zones are visualised in a histogram. Table 6.3 summarises the statistics of all M3C2 distances for the zones.

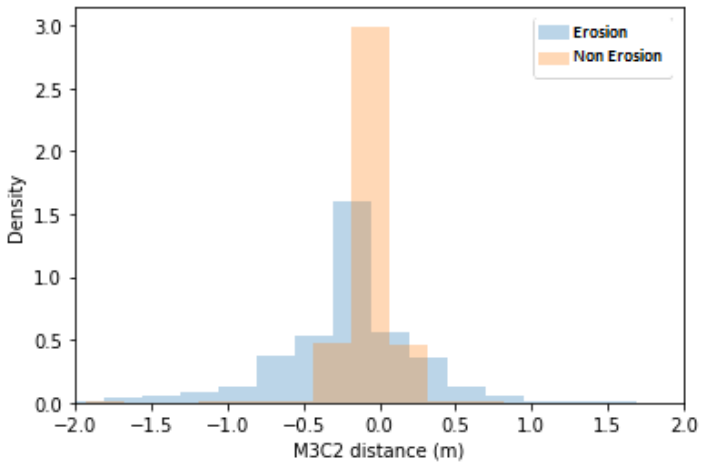

Figure 6.19: Histogram of the M3C2 distances for non-erosion and erosion zones.

Table 6.3: M3C2 distances statistics in erosion and non-erosion zones.

	Mean (m)	Std (m)
Erosion	-0.21	0.53
Non Erosion	-0.08	0.33

In Figure 6.20 a histogram of slope values for the non-erosion and erosion zones is presented for 2019 and 2022. The histograms in Figure 6.20 show that erosion zones have higher slopes than non-erosion

zones. A remarkable note is that erosion zone 5, with the rotational landslide, has a mean slope of $35.8°$, whereas the other erosion zones have mean slopes between $40.0°$ and $49.6°$. This could be expected, based on the deposition area in erosion zone 5 where the slopes are flattened.

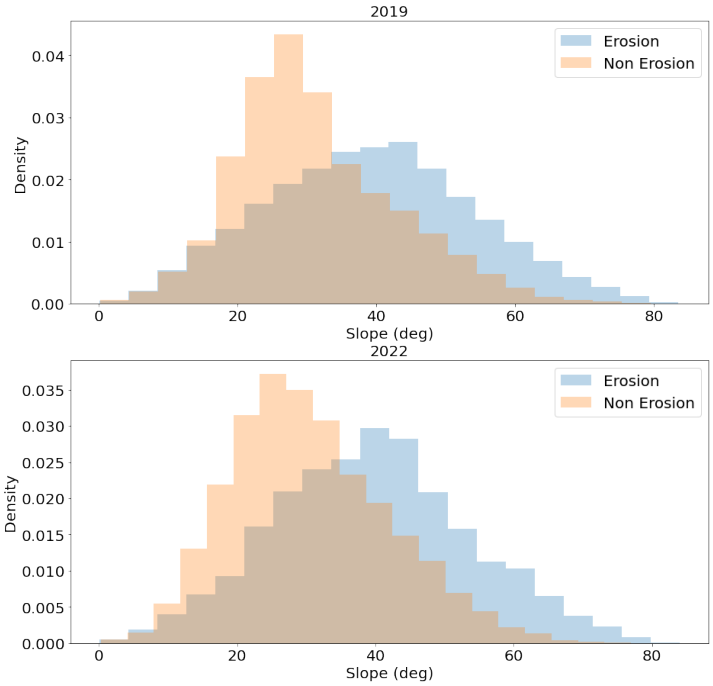

Figure 6.20: Histogram of the slope for erosion and non-erosion zones.

Table 6.4 summarises some statistics. As the histograms show, the mean slope for erosion zones ($39.3°$) is higher than for non-erosion zones ($30.9°$). Furthermore, there is a larger spread in slope values for erosion zones than for non-erosion zones.

Table 6.4: Slope statistics in erosion and non-erosion zones.

		Mean (deg)	Std (deg)
Erosion	2019	39.1	14.9
	2022	39.5	14.1
Non Erosion	2019	31.3	11.6
	2022	30.6	11.4

The values of the TWI for erosion and non-erosion zones in 2019 and 2022 are plotted in histograms in Figure 6.21. From the histograms it seems that erosion zones have lower TWI values than non-erosion zones. This was not initially expected from the knowledge on TWI behaviour on a larger catchment scale, where higher TWI values are expected in landslide prone zones. A possible explanation is that the slope is a dominating factor for erosion prone zones in this small study area, whereas the local upslope contributing area plays a more insignificant role.

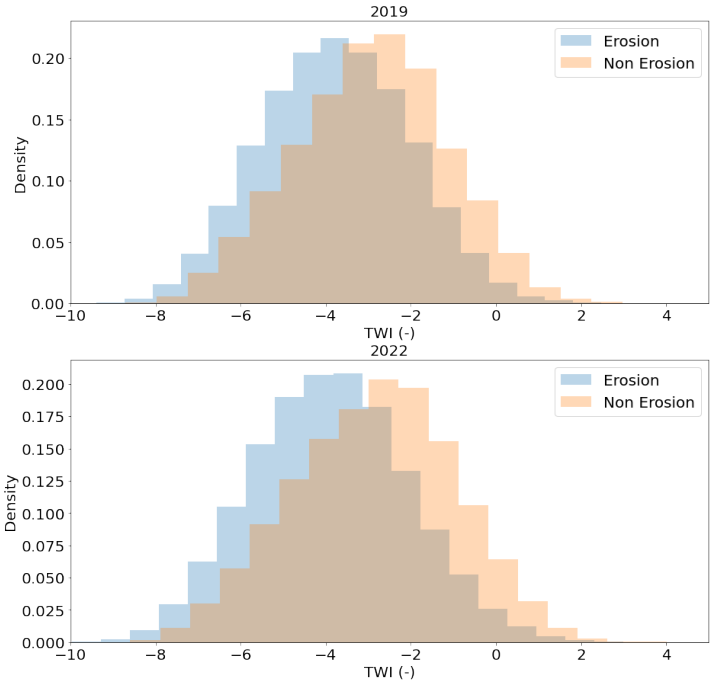

Figure 6.21: Histogram of TWI for erosion and non-erosion zones.

Table 6.5: Statistics for the TWI in erosion and non-erosion zones.

		Mean	Std
Erosion	2019	-3.76	1.73
	2022	-3.89	1.82
Non Erosion	2019	-2.93	1.79
	2022	-2.86	1.90

In Table 6.5 statistics for the Topographic Wetness Index are summarised. As the histograms in Figure 6.21 already indicated, the mean TWI for erosion zones (3.83) is lower than for non-erosion zones (2.90), but the standard deviation is similar for both zone types.

The values of the Terrain Ruggedness Index (TRI) for erosion and non-erosion zones in 2019 and 2022 are plotted in histograms in Figure 6.22. From these histograms, it is not directly clear whether there is distinctive behaviour for erosion from non-erosion zones.

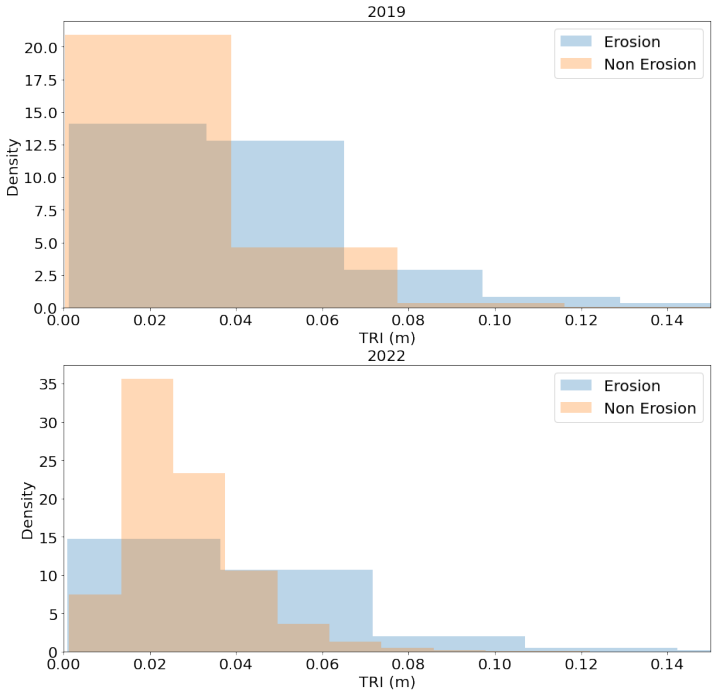

Figure 6.22: Histogram of TRI for erosion, landslide and non-erosion zones.

In Table 6.6 the mean and standard deviation of the TRI for 2019 and 2022 are summarised for the zones. Non-erosion zones have a lower mean TRI (0.029 m) in combination with a smaller standard deviation (0.015 m) compared to erosion zones (mean: 0.042 m, std: 0.029 m). This is in agreement with the photos in Figure 6.16. The slopes in stable zones seem to be continuous without sudden height differences, such as scarps, which results in low TRI values.

Table 6.6: Statistics for the TRI in erosion and non-erosion zones.

		Mean	Std
Erosion	2019	0.042	0.030
	2022	0.041	0.027
Non Erosion	2019	0.029	0.017
	2022	0.028	0.013

The histograms in Figure 6.22 and the statistics in Table 6.6 show some differences in distribution of the TRI for erosion and non-erosion zones, but they do not appear as distinct as from the map with TRI in Figure 6.10, where erosion zones can be easily identified from scarps with high values of TRI. Therefore, a new parameter p_{TRI} is introduced:

$$p_{\text{TRI}} = \frac{\#(\text{TRI} \geq 0.06)}{\#\text{TRI}} \tag{6.1}$$

The threshold of TRI is determined by inspecting the values of TRI at the scarps. The highest values of these scarps are above 0.13, but values above 0.06 are seen at the transition from scarps to other terrain. Therefore, 0.06 is set as a threshold. Table 6.7 summarises p_{TRI} for the erosion and non-erosion zones.

Table 6.7: p_{TRI} in erosion and non-erosion zones.

		p_{TRI}
Erosion	2019	0.17
	2022	0.16
Non Erosion	2019	0.05
	2022	0.03

p_{TRI}, the rate of TRI values above 0.06 m, is more than 4 times larger for erosion zones (mean p_{TRI}: 0.17) than for non-erosion zones (mean p_{TRI}: 0.04). This same comparison for TRI yields that the mean TRI in erosion zones (mean TRI: 0.042) is only 1.5 times larger than in non-erosion zones (mean TRI: 0.029). This large difference in factors shows that p_{TRI} is a good indicator of erosion zones.

This section analysed the slope, TWI, TRI and M3C2 distances for erosion and non-erosion zones. This analysis gave some distinct features. However, it was not yet shown whether the derived mean values are significantly different for the two zone types. Therefore, Welch's t-test is performed on the data. This test is a a two-sample location test to test the null hypothesis that two populations have equal means, but it does not assume equal variances like the Student's t-test. For all discussed quantities, a p-value below 0.001 was found, which indicates that the means of slope, TWI and TRI for erosion and non-erosion zones are statistically significantly different.

6.5. Changes at Nature Based Solutions

Next to the erosion patterns, the evolution of nature based solutions (NBS) and changes in vegetation also stand out from the results. For example, the two live cribwalls were implemented between the 2019 and 2022 TLS acquisitions. Figure 6.25**(a)** shows one of the live cribwalls at various moments. Figure 6.23 shows the M3C2 distances from the point clouds at the location of the two live cribwalls. At the bottom of the slope material is dug away, whereas atop of the live cribwall, the slope is higher after implementation of the live cribwall. Some salient differences in vegetation height between 2019 and 2022 are depicted in Figure 6.24. Some spots near the two live cribwalls show an increase of presence and height of the vegetation. Also at the location of the live ground anchors a large increase of vegetation is seen. These increases are in line with photos in Figure 6.25 from the OPERANDUM deliverable (Zieher et al., 2022), where an increase in vegetation is seen over time. For the live cribwall, the photos in Figure 6.25**(a)** are harder to compare with the found vegetation changes in Figure 6.24, since the found changes are mostly seen next to the live cribwall, instead of on top of these.

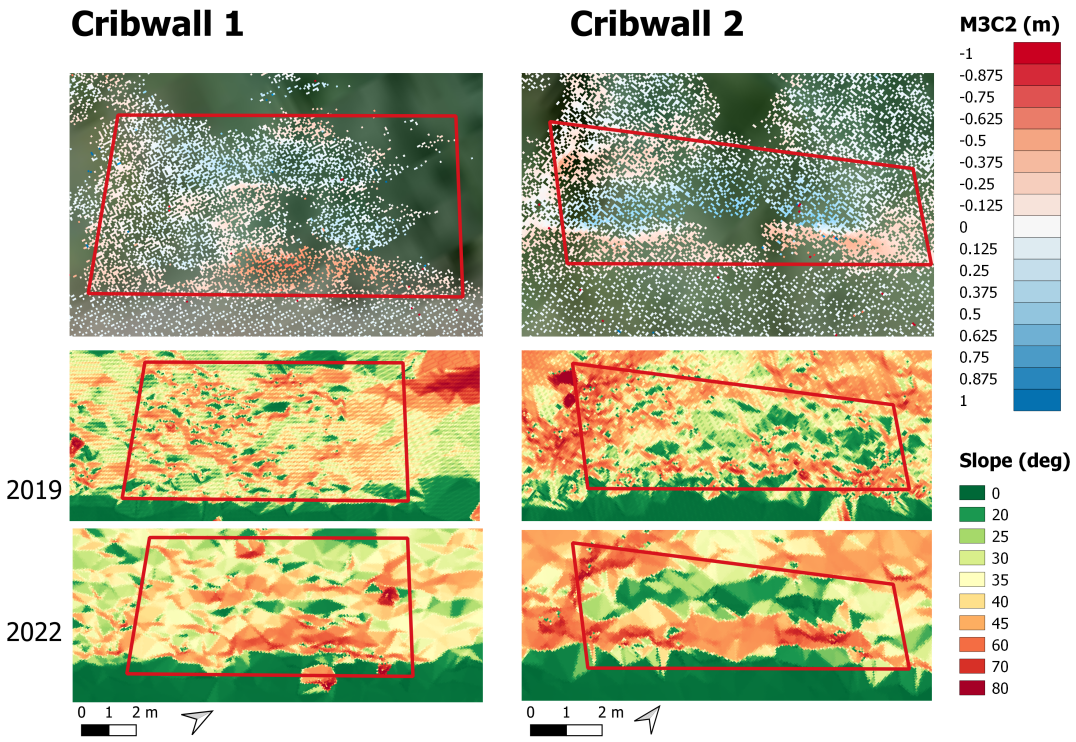

Figure 6.23: M3C2 and slope at the two live cribwalls. The red rectangles show more or less the outline of the live cribwalls. The left side gives the results of the cribwall at the upper part of the access road, the right side the results from the one at the lower part of the access road.

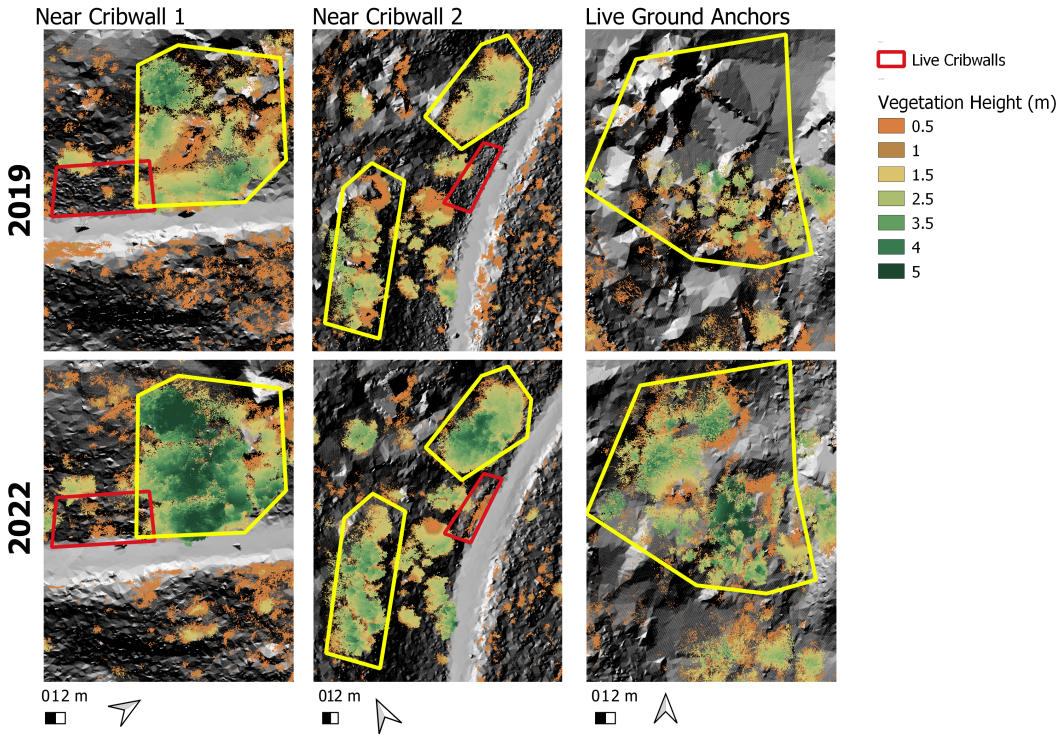

Figure 6.24: Vegetation changes at three locations near Nature Based Solutions. Exact locations are indicated in Figure 6.11.

(a) Live cribwall

(b) Live ground anchors

Figure 6.25: Evolution of the plant cover over time at the two Nature Based Solutions. Photos are from the OPERANDUM deliverable Zieher et al. (2022).

7

Discussion

This chapter provides a discussion around the data acquisition, used methods and the results presented in Chapter 4, Chapter 5 and Chapter 6.

7.1. Data Acquisition

The point clouds from 2019 and 2022 were both acquired in two or three consecutive days. Because of good weather conditions, there were no big issues during the scanning in relation to data acquisition. However, because of limited possibilities of scanning positions, some occlusions occurred caused by vegetation blocking the upper part of a slope. With terrestrial laser scanning (TLS) in complex sloped terrain, this type of occlusions are often inevitable when using a ground based scanning station. Some occlusions can be overcome when an unmanned aerial vehicle (UAV) such as a drone, is used. A drone flies over the terrain and then also acquires data of the slope 'behind' the vegetation, as illustrated in Figure 7.1. A drawback of a UAV set up is that more uncertainty factors come into play. For example, the uncertainties from the orientation (from the IMU sensor) and the positioning (uncertainties from GNSS) of the drone should be taken into account.

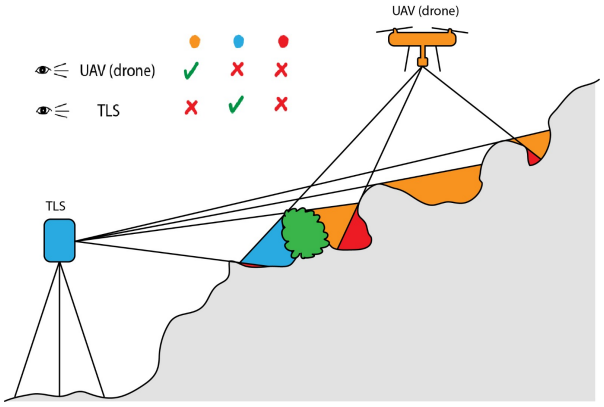

Figure 7.1: Viewing geometry and coverage from terrestrial laser scanning (TLS) and an unmanned aerial vehicle (a drone for example) from single positions in a complex. Illustration based on figure in Šašak et al. (2019).

During both TLS data acquisitions, it was chosen to perform non-colourised scans, because this saves a large amount of time per scan. However, during the data processing, the interpretation of the uncoloured point clouds was experienced as difficult sometimes. Furthermore, the identification of landslide scarps could be improved, if the point cloud was colourised.

7.2. Data Processing

The first pre-processing step was registration. For registration, the Iterative Closest Point (ICP) algorithm was used and validated. However, the Catterline Bay has abundant stable points in the northern part, with houses, a pier and lampposts, but in the southern part those objects are lacking. Therefore, it cannot be guaranteed that the registration error is global for the whole point cloud. The registration is especially important for the change detection. If there is a small tilt in one point cloud compared to the other point cloud, then the change detection will give offsets in certain parts of the point cloud. This problem can be overcome in future studies by placing stable tie points in the study area, such that multiple data acquisitions can be easily aligned.

The next pre-processing step was subsampling. Because the raw point clouds of 2019 and 2022 were too large to open and process on a personal laptop, the point clouds were subsampled to 50mm. As a consequence, some refinement was lost. In some processing steps, the unsubsampled point cloud could give better results. Therefore, if a high performance computing platform would be available, it is recommended to work with the original unsubsampled point clouds.

The filtering of point clouds was the first processing step. After an extensive comparison of different ground filtering methods, the CANUPO algorithm was eventually used, because it uses a full 3D approach and it uses the local dimensionality feature on multiple scales. However, because the classification is supervised and thus requires high-quality training samples, the algorithm is labour intensive. The CANUPO algorithm gave good precision on both the training and test data sets, respectively approximately 99.4% and 94.5%. The algorithm had minor difficulties with separating between vegetation close to the ground. However, the other considered methods in Section 3.3, such as the Cloth Simulation Filter and the Multi-resolution Hierarchical Classification, performed much worse with separating between vegetation and ground, judged by visual inspection. From Figure 3.1, it seemed that intensity could help in classifying ground and non-ground points. However, this was not used in the CANUPO algorithm. At the end of this project, a new version of the CANUPO plugin in CloudCompare was released. The plugin of CANUPO now allowed for adding intensity as a classification feature. A new classifier was trained, using the same settings and training data set, but this time also intensity was added as a feature. This yielded $ba = 99.4$% and $fdr = 18.8$. Compared to the classifier used in this project, the balanced accuracy was exactly the same, but the fdr was lower than the original $fdr = 21.9$, which means that the classes were less good separated and ba was less robust. Therefore, adding intensity as a classification feature does not directly lead to a better classification. However, adding new geometric features could possibly increase the performance of the classifier. At this moment, the plugin is limited to adding one additional scalar field as a feature. Thus, the implementation of a multi-class and multi-attribute (including intensity) classifier is a suggested improvement in order to develop a more powerful classifier in the future.

For 3D change detection, the Multiscale Model to Model Cloud Comparison (M3C2) method was used, which is the current state of the art in geomorphological point cloud-based change analysis. By computing the Level of Detection (LoD) at 95%, changes large enough to distinguish from noise were detected. This resulted in changes, M3C2 distances, and their uncertainties. In the formula for LoD in Equation 4.6, the registration uncertainty r is added as a constant and thus as a systematic influence for the whole point cloud. However, uncertainties on the sensor side are actually point-based. For example, if a point is described by spherical coordinates, then uncertainties in the two angular coordinates are driven by the finite beam divergence of the laser and the angle quantisation (Winiwarter et al., 2021). The ranging uncertainties are coupled to the intensity of the signal, which varies with range, material reflectivity and atmospheric transmittance. If these ranging and angular uncertainties are combined using error propagation, error ellipsoids could be derived per point. Recent studies (DiFrancesco et al., 2020; Winiwarter et al., 2021) noted that the Level of Detection (LoD) predicted by M3C2 may underestimate the actually detectable change. This can happen especially in cases when the roughness of the object at the projection radius is larger than the range uncertainty. Winiwarter et al. (2021) proposed an additional error propagation method to the existing M3C2 method, which refines measurement uncertainties per point. Incorporation of this new method in this study could improve the change detection results.

7.3. Data and Sensitivity Analysis

From the M3C2 distances, erosion zones were identified based on grouped negative distances, sometimes with a group of positive distances nearby and an edge of high terrain ruggedness index (TRI) values. The M3C2 distances indicate change in the terrain model. Accumulation and depletion of material caused by erosion are exposed with the M3C2 distances. The edge of high TRI exposes the scarps of (beginning) landslides. By setting a threshold of TRI $= 0.06$ for the newly defined p_{TRI}, a very distinctive indicator for erosion zones was found.

The mean slope of 39.3° for erosion zones is significantly higher than for non-erosion zones (30.9°). This is in agreement with earlier studies (Alexakis et al., 2014; Lee & Talib, 2005; Yong et al., 2022). The slope angle has a critical value, which is also seen for loose material on a slope with the angle of repose. Every material has a critical slope or angle on which material will remain at rest without rolling down. This critical slope depends among others on morphology of the material and the presence of water in the soil. Furthermore, the distribution of the topographic wetness index (TWI) for erosion zones compared to non-erosion zones was investigated. On catchment scale, spatial patterns of high TWI are used to identify find landslide prone zones (Rózycka et al., 2017). It was unknown how the TWI is related to erosion zones on a cm-scale. Using such a small scale in this study, the TWI was able to reveal water drainage channels and the drainage density, but these channels were not directly related to the location of erosion zones. The statistical analysis even revealed that the erosion zones are characterised by lower TWI values than the non-erosion zones. Although this was not initially expected, a possible explanation is that the slope is a dominating factor for erosion prone zones in this small study area, whereas the local upslope contributing area plays a more insignificant role, thus resulting in low TWI values in erosion zones. An important remark to the process of identifying erosion zones is that the suggested method is subject to human bias. Defining an erosion zone is a delicate process. One should be consistent in including the depletion and accumulation zones. Even though an expert works in a consistent way to identify erosion zones, the zones will always be affected in some sense by human bias and subjectivity.

TRI is a scale-dependent parameter. Therefore, the effect of scale on the TRI outcomes is studied. The TRI map with the default spatial resolution of 5cm is subjected to many abrupt local changes, which in some cases can be seen as noisy. Furthermore, some of the characteristics of the erosion zones, such as the scarps, may have a larger characteristic length than 5cm. This may result in a suboptimal capture of the scarp in the TRI map. To study this effect, the DTM is downsampled to 10cm, 20cm, 50cm and 100cm. From the downsampled DTM, the TRI is calculated. 3 of the erosion zones are displayed in Figure 7.2 with the effect of using a downsampled raster on the TRI. Figure 7.2 shows that by downsampling the original raster the result becomes more smoothened. Especially at the resolution of 20cm, the scarps are more pronounced than with a 5 cm resolution. At a spatial resolution of 100cm the result becomes too coarse to perform an analysis. The 50 cm resolution would be on the boundary of distinguishable scarps. A coarser resolution is not recommended for this study area.

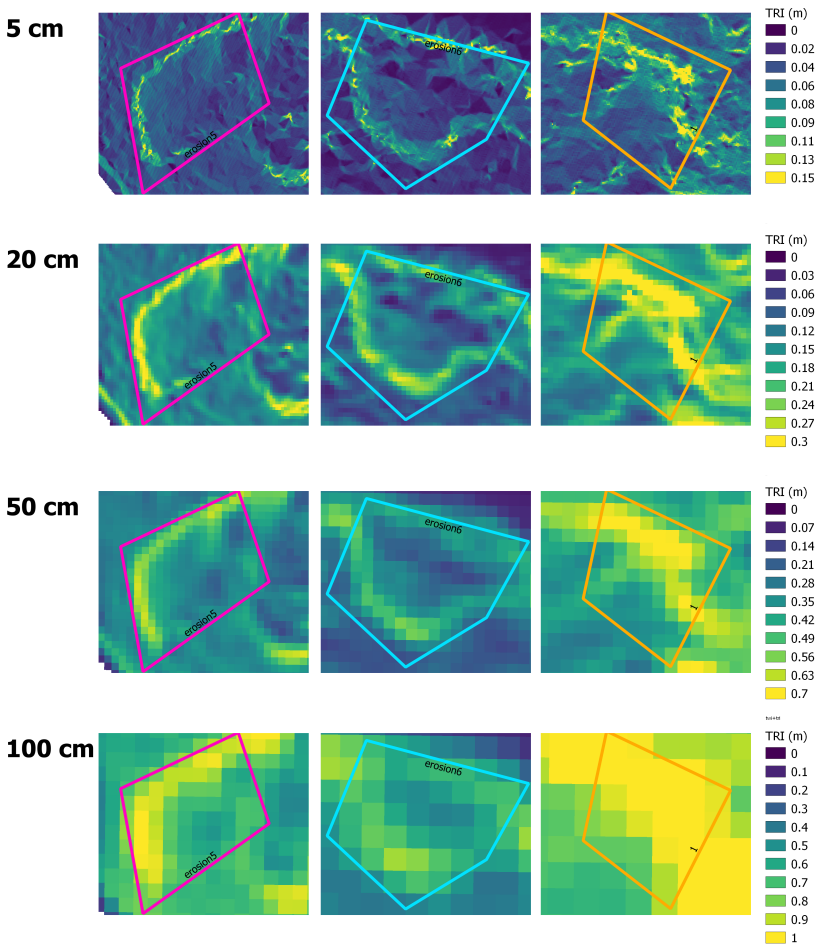

Figure 7.2: TRI at 3 of the erosion zones at different scales.

Changes in vegetation height were also studied. These changes are not directly related to erosion processes, but they are used to assess the status of Nature Based Solutions (NBS). Many NBS in Catterline are focused on the implementation of plants in various ways, among others to increase the soil strength. The approach of incorporating vegetation changes in the analysis was the calculation of cloud-to-mesh distances (distances of the cloud of non-ground points to the mesh of ground points). Comparison of vegetation height in 2019 and 2022 gave some interesting insights. First of all, near the two live cribwalls an increase of presence and height of vegetation was seen. Also the location of the live ground anchors showed a great increase. This is in line with the results from the OPERANDUM deliverable (Zieher et al., 2022).

In the analysis of the different maps, it was important to use photos as a validation tool. From the point cloud or M3C2 result, it is not visible whether a change is caused by the implementation of an NBS, which is human intervention, or of natural origin. To analyse and interpret the results, knowledge of the study area is needed. A drawback of this approach is that human supervision is an important pillar. As discussed in Section 7.1, colourising of the point cloud could be part of a solution to this problem.

7.4. Comparison with other results at Catterline Bay

The depicted erosion zones in Chapter 6 are validated as erosion zones in various ways. First of all, photos from the author confirmed the presence of failure zones and scarps in the erosion zones. Furthermore, the results are also compared with results from optical satellite imagery and results from a study by Gonzalez-Ollauri and Mickovski (2021). This section compares the results from this study with other results from the Catterline Bay.

7.4.1. Results from NDVI

Personal communication with Silvia Alfieri confirmed that optical satellite imagery from WorldView 2 and 3 show a strong decrease in Normalised Difference Vegetation Index (NDVI) in 4 of the 5 identified erosion zones. The change in NDVI was calculated images from 7 June 2019 and 23 June 2022. In Figure 7.3 the relative change is visualised. The green zones are the identified erosion zones from this study. Zones 2, 3 and 5 have a strong decrease in NDVI, whereas zone 1 has only a slight decrease and zone 4 seems to have a small increase. NDVI is often used in remote sensing for monitoring vegetation. Strong changes in NDVI can indicate landslides, because vegetated areas often become bare soil areas in landslide zones (W. Yang et al., 2013). The zones near NBS with an increase in vegetation height from Section 6.5 are highlighted with green boxes. These zones show an overall positive change in NDVI. Next to these indicated areas, there are also some zones with strong negative or positive changes in NDVI at the edges of the road and the beach. These changes are not real changes, but are due to alignment issues.

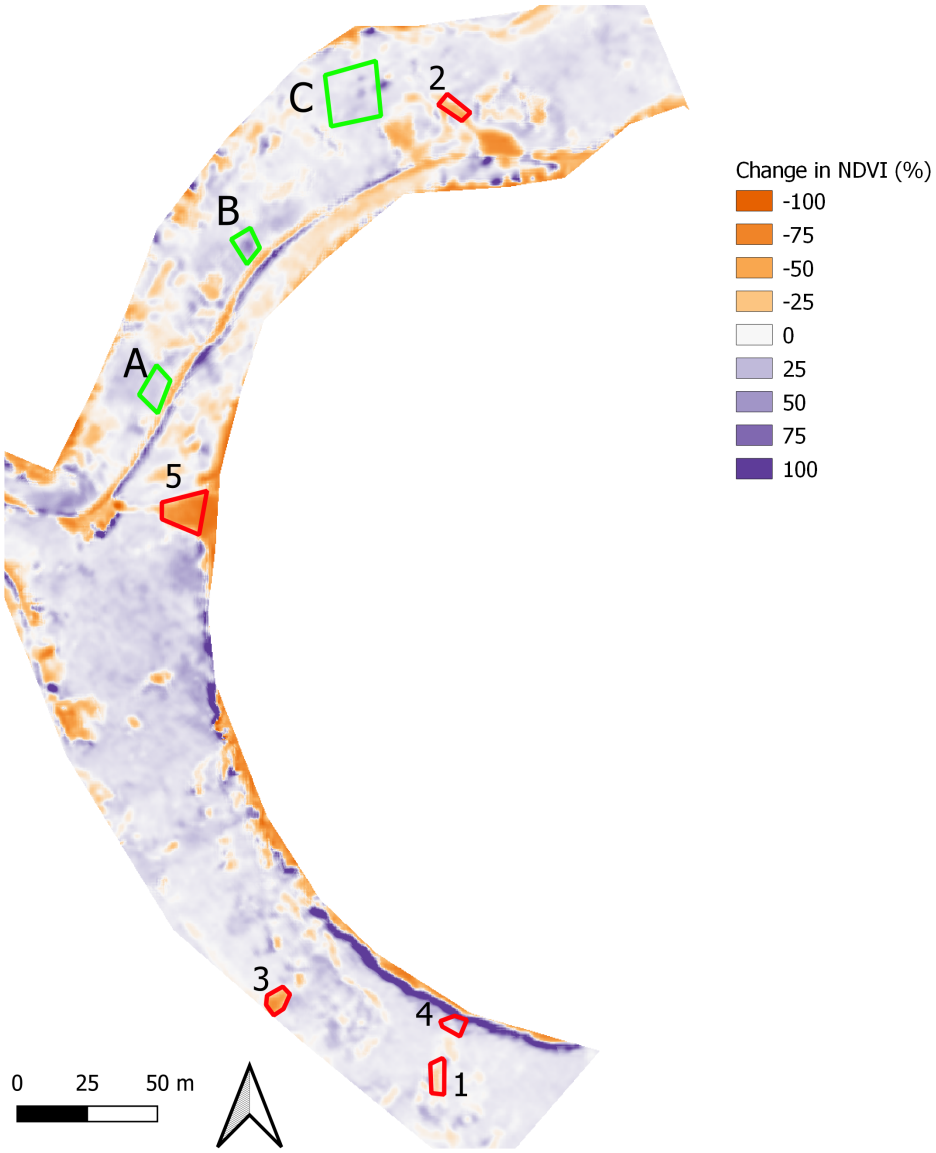

Figure 7.3: Relative change (%) in NDVI, computed from WorldView 2 and 3 optical satellite imagery. Results are obtained by Silvia Alfieri. In red the identified erosion zones are depicted with a negative change in NDVI. Green indicates the locations near NBS, that are discussed in Section 6.5. The green zones have a positive change in NDVI. A is at live cribwall 1, B at live cribwall 2 and C at the live ground anchors.

7.4.2. Results from Gonzalez-Ollauri and Mickovski (2021)

As discussed in Chapter 5, information on landslide zones is available from Gonzalez-Ollauri and Mickovski (2021). Although these zones were available from the start of the project, the zones were not used to identify the erosion zones in this research. In this way, the results from this research are not dependent on results from other sources than the TLS campaigns. Gonzalez-Ollauri and Mickovski (2021) used a Digital Elevation Model (DEM) with a resolution of 2 m. The stream network and slope were derived from the DEM and then used to classify landslide-prone zones. These zones will be used as a validation for the results in this study. To these zones will be referred as 'validation erosion zones'. The characteristic features are extracted for the validation zones and analysed to see if they match with the results in this research.

Qualitatively, most validation zones seem to appear on locations with the described erosion characteristics, such as edges with high TRI values and steep slopes. Some of the validation zones also overlap with the identified erosion zones. In Appendix C a map is included with the locations of the validation erosion zones. The M3C2 distances are extracted from the validation erosion zones and compared with the identified erosion zones in a histogram in Figure 7.4. From Figure 7.4, it becomes clear that the validation zones have a 2 times smaller mean M3C2 distance, although it has a comparable standard deviation.

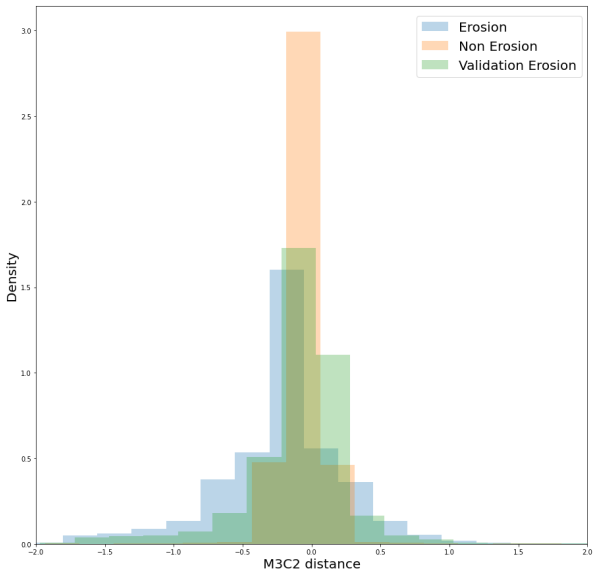

Figure 7.4: Histogram of M3C2 distances of the validation erosion zones (blue) and the erosion zones (orange).

Table 7.1: Statistics from the M3C2 distances of the three zone types.

	Mean (m)	Std (m)
Erosion	-0.21	0.53
Validation Erosion	-0.12	0.46
Non Erosion	-0.08	0.33

From the validation erosion zones, also the statistics of the slope, TWI and TRI are calculated. The slope statistics are summarised in Table 7.2. The mean slope of the validation zones is slightly higher than for the identified erosion zones.

Table 7.2: Slope statistics in three zone types.

	Year	Mean (deg)	Std (deg)
Erosion	2019	39.1	14.9
	2022	39.5	14.1
Validation Erosion	2019	41.4	13.6
	2022	41.4	13.2
Non Erosion	2019	31.3	13.0
	2022	30.6	11.4

Table 7.3 summarises the statistics for the TWI. TWI has very similar statistics for the validation erosion zones and the erosion zones.

Table 7.3: Statistics for the TWI in three zone types in 2022.

	Year	Mean (-)	Std (-)
Erosion	2019	-3.76	1.73
	2022	-3.81	1.65
Validation Erosion	2019	-3.80	1.75
	2022	-3.81	1.67
Non Erosion	2019	-2.93	1.79
	2022	-2.93	1.79

Lastly, Table 7.4 summarises the statistics for the TWI. Although the mean TRI in 2019 is a bit lower for the validation erosion zones, the other values are very comparable for the erosion and validation erosion zones.

Table 7.4: Statistics for the TRI in three zone types in 2022.

	Year	Mean (m)	Std (m)
Erosion	2019	0.042	0.030
	2022	0.041	0.027
Validation Erosion	2019	0.038	0.028
	2022	0.044	0.027
Non Erosion	2019	0.029	0.017
	2022	0.028	0.014

From the comparison of the identified erosion zones with landslide zones from Gonzalez-Ollauri and Mickovski (2021), used as validation zones, it is found that the TWI and TRI characteristics from the identified erosion zones correspond very well with the validation zones. The slope of the validation erosion zones ($41.5°$) is slightly higher than for the erosion zones ($39.3°$). A remarkable difference is the two times smaller mean for M3C2 distances. One possible explanation is that the identified erosion zones in this study strongly depend on groups of negative M3C2 distances and thus on the occurrence of erosion between 2019 and 2022, whereas the landslide zones from Gonzalez-Ollauri and Mickovski (2021) are based on the slope in wet zones. Another explanation is that the identification method in this study is too strict on the selection of group of negative M3C2 distances, such that only very evident and severe erosion zones are identified. This also raises the question whether it is a fair distinction to separate erosion and non-erosion zones. In reality, it will be more a gradual scale of how heavy the erosion is in an area. In conclusion, the derived erosion zones in this study have very similar geomorphological behaviour with the erosion zones from Gonzalez-Ollauri and Mickovski (2021). However, a large advantage of the identification method in this study is that erosion rates are also taken into account in addition to the static geomorphometric quantities.

8

Conclusion & Recommendations

This chapter draws conclusions from this study in Section 8.1 by answering the research questions raised in Section 1.2. Subsequently, Section 8.2 presents some recommendations for future research on monitoring erosion using point clouds from terrestrial laser scanning.

8.1. Conclusions

This section provides answers to the defined subquestions from Section 1.2. Then, the main conclusion of this thesis is presented as an answer on the main research question.

1. How to acquire a TLS data set in complex sloped terrain?
In this research, the Catterline Bay is the area of study. This specific area is characterised by slopes with vegetation. Furthermore, there are only limited possibilities for scan locations: only at the access road and on the cobble beach. The beach has large variations in width due to tides, which should be taken into account. This makes the creation of a complete point cloud without occlusions challenging. It is especially hard to obtain points 'behind' vegetation at the upper part of slopes and points below dense vegetation, because the laser is not able to penetrate through dense vegetation. Because the study area is too big to cover with scans in just one day, scans were performed on multiple consecutive days. To be able to tie these individual scans together, stable reflector targets are placed at various locations overnight. Despite unavoidable occlusions, a satisfying point cloud could be obtained in October 2019 and April 2022 by including enough scanning locations with overlapping areas.

2. How to identify static erosion characteristics from point cloud data?
The area of study Catterline Bay is prone to landslides. A landslide involves movement along a well-defined slippage plane. Characteristics of landslides are among others scarps, accumulation and depletion zones. These characteristics were detected from derivatives of a Digital Terrain Model (DTM) of the study area. Therefore, the point cloud was classified in ground and non-ground points. The local dimensionality of points on various scales was used as feature input to train the LDA classifier. The performance of classification was assessed by calculating the precision on the test data set. The precision was found to be 94.7% for ground points and 94.3% for non-ground points. To obtain the DTM, a raster was created from the classified ground points. Various geomorphometric quantities, such as slope, Terrain Ruggedness Index (TRI) and Topographic Wetness Index (TWI), were calculated from the DTM. Scarps are well exposed by an edge of high TRI values.

3. How to acquire an accurate temporal change detection map of erosion?
To perform change detection, the two point cloud acquisitions from October 2019 and April 2022 were compared. The data sets were aligned using the Iterative Closest Point algorithm. The assessment of cloud-to-cloud distances of various objects, that were used to be stable, such as chimneys, the pier and a lamppost, yielded a root-mean-square error of the registration of 3.3 cm. However, only the northern part of the bay contained stable objects, thus it cannot be guaranteed that this error is global. The classified ground points were used for change detection. An accurate 3D comparison was done

using the well-established method Multiscale Model to Model Cloud Comparison (M3C2). Because of the registration error of 3.3cm, significant change could only be detected if the M3C2 distance was larger than 3.3cm. Furthermore, a distance uncertainty was calculated for each M3C2 distance based on local estimates of the point cloud roughness for both acquisitions. This gave a mean uncertainty in the M3C2 results of 5 cm. However, the uncertainties increased with larger M3C2 distances.

Next to the change detection based on the ground points, also changes in vegetation presence and height were extracted from calculating the cloud-to-mesh distances between non-ground and ground points. Because plants are used in the study area to counteract landslides, changes in vegetation gave insight in the effect of these Nature Based Solutions. Near Live Cribwalls and at the Live Ground Anchors, a strong increase of vegetation presence and height was observed.

4. How to identify erosion zones and assess erosion patterns?
Various erosion zones were detected using notable 'edges' with high Terrain Ruggedness Index values, accompanied with groups of negative M3C2 distances, using photos as a validation tool. Also, stable, non-erosion zones were identified. From both zone types, the geomorphometric quantities and M3C2 distances were statistically analysed. Various conclusions could be drawn from the statistical analysis. Erosion zones had a mean M3C2 distance of -21 cm, whereas the non-erosion zones had a mean of 8cm. p_{TRI} was introduced to capture the pattern of high TRI values in erosion zones. p_{TRI} is about 4 times larger for erosion zones than non-erosion zones. Erosion zones are also characterised by a significantly steeper slope of $39.3°$, compared to $30.9°$ for non-erosion zones. Also the Topographic Wetness Index was analysed for both zone types, but this did not give distinctive statistics. The identified erosion zones were also validated by changes in NDVI from optical satellite imagery. These zones showed a strong decrease in NDVI. Lastly, the identified erosion zones were compared to identified landslide zones from earlier studies. Because of different identification methods, differences were seen in the mean slope and the mean M3C2 distances. However, the characteristics were still distinctive from the non-erosion zones.

5. How to compare results from terrestrial laser scanning data compared to other remote sensing techniques?
Terrestrial Laser Scanning is able to deliver very high spatial resolution data, compared to other remote sensing techniques. The high point density and the 3D component allow for a unique 3D change detection. However, the use of a ground based platform limits the options of scan positions. Especially in a complex sloped terrain, this can lead to inevitable occlusions. A drone with laser scanning equipment overcomes this problems and is able to acquire data 'behind' obstacles. Satellite data sources have often almost daily observations, which allow for trend estimations of the erosion patterns, but this comes at the cost of low spatial resolution.

Main Research Question

With the answers to the subquestions, the main research question can be answered, which is:

> **How can terrestrial laser scanning be used to monitor erosion processes on a coastal slope?**

To answer this question, two terrestrial laser scanning campaigns were performed. The acquired point clouds were processed according to the developed workflow in Chapter 4. The first steps were subsampling, alignment and ground filtering. Ground filtering was done using linear discriminant analysis (LDA) with the local dimensionality of points on various scales as feature input. From the classified ground points, DTMs were created and change detection was done using the method Multiscale Model to Model Cloud Comparison (M3C2). Geomorphometric quantities were derived from the DTM. Based on a combination of the Terrain Ruggedness Index, M3C2 distances and photos, erosion and non-erosion zones were derived. From these identified zones, erosion processes were monitored by analysing the differences in the distributions of various quantities, such as M3C2 distances, slope, TRI and TWI.

8.2. Recommendations

Regarding the proposed workflow in this thesis, there are multiple aspects, which can be further studied in future research. These points are shortly mentioned below.

- **Incorporation of more acquisitions**

  By incorporating more frequent acquisitions the trend in the erosion patterns can be analysed.

- **Inclusion of point clouds of similar areas in the analysis**

  Including other bays with similar erosion patterns enhances the number of erosion zones, which leads to a more generalised description of the distinctive features of erosion zones.

- **Improvement of the ground classification**

  Although visual inspection showed that intensity might be helpful to separate ground and non-ground points, the current binary classifier does not allow for multi-attributes. Therefore, the implementation of a multi-class and multi-attribute (including intensity) classifier is a suggested improvement in order to develop a more powerful classifier in the future.

- **Creation of a multi-source susceptibility map**

  The use of more layers from other sources should improve the predictive power of a susceptibility map. Examples of others sources are geology, weather information, hydrological field experiments (for example runoff and scouring experiments) and also other remote sensing sources, such as satellite optical imagery and (In)SAR.

- **Data-driven susceptibility assessment**

  In this research, a knowledge-driven susceptibility assessment was performed, because the study area and number of erosion events are both too small to perform a full data-driven assessment. However, with more information layers and some supervision, the use of machine learning methods can be explored. This can be a desirable improvement, because it makes the assessment less subjective and biased.

Bibliography

Alexakis, D. D., Agapiou, A., Tzouvaras, M., Themistocleous, K., Neocleous, K., Michaelides, S., & Hadjimitsis, D. G. (2014). Integrated use of GIS and remote sensing for monitoring landslides in transportation pavements: The case study of Paphos area in Cyprus. *Natural Hazards*, *72*(1), 119–141. https://doi.org/10.1007/s11069-013-0770-3

Ambroise, B., Beven, K., & Freer, J. (1996). Toward a generalization of the TOPMODEL concepts: Topographic indices of hydrological similarity. https://doi.org/10.1029/95WR03716

Barnes, N., Luffman, I., & Nandi, A. (2016). Gully erosion and freeze-thaw processes in clay-rich soils, northeast Tennessee, USA. *GeoResJ*, *9-12*, 67–76. https://doi.org/10.1016/j.grj.2016.09.001

Bayer, B., Simoni, A., Schmidt, D., & Bertello, L. (2017). Using advanced InSAR techniques to monitor landslide deformations induced by tunneling in the Northern Apennines, Italy. *Engineering Geology*, *226*, 20–32. https://doi.org/10.1016/j.enggeo.2017.03.026

Besl, P. J., & McKay, N. D. (1992). A Method for Registration of 3-D Shapes. *IEEE Transactions on pattern analysis and machine intelligence*, *14*(2), 239–256.

Bishop, C. M. (2006). *Pattern Recognition and Machine Learning* (M. Jordan, J. Kleinberg, & B. Schölkopf, Eds.; 2nd ed., Vol. 4). Springer.

Bogaard, T. A., & Greco, R. (2016). Landslide hydrology: from hydrology to pore pressure. https://doi.org/10.1002/wat2.1126

Brodu, N., & Lague, D. (2012). 3D terrestrial lidar data classification of complex natural scenes using a multi-scale dimensionality criterion: Applications in geomorphology. *ISPRS Journal of Photogrammetry and Remote Sensing*, *68*(1), 121–134. https://doi.org/10.1016/j.isprsjprs.2012.01.006

Casalí, J., Loizu, J., Campo, M. A., De Santisteban, L. M., & Álvarez-Mozos, J. (2006). Accuracy of methods for field assessment of rill and ephemeral gully erosion. *Catena*, *67*(2), 128–138. https://doi.org/10.1016/j.catena.2006.03.005

Chen, C., Li, Y., Li, W., & Dai, H. (2013). A multiresolution hierarchical classification algorithm for filtering airborne LiDAR data. *ISPRS Journal of Photogrammetry and Remote Sensing*, *82*, 1–9. https://doi.org/10.1016/j.isprsjprs.2013.05.001

Chen, C., Li, Y., Zhao, N., Guo, J., & Liu, G. (2017). A fast and robust interpolation filter for airborne lidar point clouds. *PLoS ONE*, *12*(5). https://doi.org/10.1371/journal.pone.0176954

Cruden, D. (1993). The Multilingual Landslide Glossary.

DiFrancesco, P. M., Bonneau, D., & Hutchinson, D. J. (2020). The implications of M3C2 projection diameter on 3D semi-automated rockfall extraction from sequential terrestrial laser scanning point clouds. *Remote Sensing*, *12*(11). https://doi.org/10.3390/rs12111885

D'Oleire-Oltmanns, S., Marzolff, I., Peter, K. D., & Ries, J. B. (2012). Unmanned aerial vehicle (UAV) for monitoring soil erosion in Morocco. *Remote Sensing*, *4*(11), 3390–3416. https://doi.org/10.3390/rs4113390

Dunkley, R., MacDonell, C., Naylor, L., Muir, F., & Fitton, J. (2021). *Dynamic Coast Mapping Coastal Erosion Disadvantage in Scotland* (tech. rep.). University of Glasgow.

Gao, C., Li, P., Hu, J., Yan, L., Latifi, H., Yao, W., Hao, M., Gao, J., Dang, T., & Zhang, S. (2021). Development of gully erosion processes: A 3D investigation based on field scouring experiments and laser scanning. *Remote Sensing of Environment*, *265*. https://doi.org/10.1016/j.rse.2021.112683

Girardeau-Montaut, D. (2019). CANUPO (plugin). https://www.cloudcompare.org/doc/wiki/index.php/CANUPO_(plugin)

Glira, P., & Pfeifer, N. (2015). A Correspondence Framework for ALS Strip Adjustments based on Variants of the ICP Algorithm. https://doi.org/10.1127/pfg/2015/02701

Gómez-Gutiérrez, Á., & Gonçalves, G. R. (2020). Surveying coastal cliffs using two UAV platforms (multirotor and fixed-wing) and three different approaches for the estimation of volumetric

changes. *International Journal of Remote Sensing*, *41*(21), 8143–8175. https://doi.org/10.1080/01431161.2020.1752950

Gómez-Gutiérrez, Á., Schnabel, S., Berenguer-Sempere, F., Lavado-Contador, F., & Rubio-Delgado, J. (2014). Using 3D photo-reconstruction methods to estimate gully headcut erosion. *Catena*, *120*, 91–101. https://doi.org/10.1016/j.catena.2014.04.004

Gonzalez-Ollauri, A., & Mickovski, S. B. (2016). Using the root spread information of pioneer plants to quantify their mitigation potential against shallow landslides and erosion in temperate humid climates. *Ecological Engineering*, *95*, 302–315. https://doi.org/10.1016/j.ecoleng.2016.06.028

Gonzalez-Ollauri, A., & Mickovski, S. B. (2021). A simple gis-based tool for the detection of landslide-prone zones on a coastal slope in Scotland. *Land*, *10*(7). https://doi.org/10.3390/land10070685

Guerrero-Campo, J., & Fitter, A. H. (2001). *Relationships between root characteristics and seed size in two contrasting floras* (tech. rep.).

Highland, L., & Johnson, M. (2004). Landslide Types and Processes. *USGS*.

Horn, B. K. (1981). Hill Shading and the Reflectance Map. *Proceedings of the IEEE*, *69*(1), 14–47. https://doi.org/10.1109/PROC.1981.11918

Janßen, J., Medic, T., Kuhlmann, H., & Holst, C. (2019). Decreasing the uncertainty of the target center estimation at terrestrial laser scanning by choosing the best algorithm and by improving the target design. *Remote Sensing*, *11*(7). https://doi.org/10.3390/RS11070845

Kenneth Hamblin, W., & Christiansen, E. H. (2004). *Earth's Dynamic Systems* (10th ed.). Prentice Hall, Pearson Education.

King, C., Baghdadi, N., Lecomte, V., & Cerdan, O. (2005). The application of remote-sensing data to monitoring and modelling of soil erosion. *Catena*, *62*(2-3), 79–93. https://doi.org/10.1016/j.catena.2005.05.007

Kuhn, D., & Prüfer, S. (2014). Coastal cliff monitoring and analysis of mass wasting processes with the application of terrestrial laser scanning: A case study of Rügen, Germany. *Geomorphology*, *213*, 153–165. https://doi.org/10.1016/j.geomorph.2014.01.005

Kumar, P., Debele, S. E., Sahani, J., Rawat, N., Marti-Cardona, B., Alfieri, S. M., Basu, B., Basu, A. S., Bowyer, P., Charizopoulos, N., Jaakko, J., Loupis, M., Menenti, M., Mickovski, S. B., Pfeiffer, J., Pilla, F., Pröll, J., Pulvirenti, B., Rutzinger, M., … Zieher, T. (2021). An overview of monitoring methods for assessing the performance of nature-based solutions against natural hazards. https://doi.org/10.1016/j.earscirev.2021.103603

Lague, D., Brodu, N., & Leroux, J. (2013). Accurate 3D comparison of complex topography with terrestrial laser scanner: Application to the Rangitikei canyon (N-Z). *ISPRS Journal of Photogrammetry and Remote Sensing*, *82*, 10–26. https://doi.org/10.1016/j.isprsjprs.2013.04.009

Ledoux, H., Ohori, K. A., & Peters, R. (2021). *Computational modelling of terrains* (tech. rep.). https://github.com/tudelft3d/terrainbook/releases

Lee, S., & Talib, J. A. (2005). Probabilistic landslide susceptibility and factor effect analysis. *Environmental Geology*, *47*(7), 982–990. https://doi.org/10.1007/s00254-005-1228-z

Leica ScanStation P30/P40. (2015). https://leica-geosystems.com/-/media/files/leicageosystems/products/datasheets/leica_scanstation_p30-p40_civil_ds.ashx?la=en-us&hash=3335189492F6A6673DDABBEBF3990281

Li, F. L., & Bao, W. K. (2015). New insights into leaf and fine-root trait relationships: Implications of resource acquisition among 23 xerophytic woody species. *Ecology and Evolution*, *5*(22), 5344–5351. https://doi.org/10.1002/ece3.1794

Longoni, L., Papini, M., Brambilla, D., Barazzetti, L., Roncoroni, F., Scaioni, M., & Ivanov, V. I. (2016). Monitoring riverbank erosion in mountain catchments using terrestrial laser scanning. *Remote Sensing*, *8*(3). https://doi.org/10.3390/rs8030241

Mayr, A., Rutzinger, M., Bremer, M., Oude Elberink, S., Stumpf, F., & Geitner, C. (2017). Object-based classification of terrestrial laser scanning point clouds for landslide monitoring. *Photogrammetric Record*, *32*(160), 377–397. https://doi.org/10.1111/phor.12215

Min, H., Han, K. M., & Kim, Y. J. (2020). Accelerating Probabilistic Volumetric Mapping using Ray-Tracing Graphics Hardware. http://arxiv.org/abs/2011.10348

Mukupa, W., Roberts, G. W., Hancock, C. M., & Al-Manasir, K. (2017). A review of the use of terrestrial laser scanning application for change detection and deformation monitoring of structures. https://doi.org/10.1080/00396265.2015.1133039

Myers, D. T., Rediske, R. R., & McNair, J. N. (2019). Measuring streambank erosion: A comparison of erosion pins, total station, and terrestrial laser scanner. *Water (Switzerland)*, *11*(9). https://doi.org/10.3390/w11091846

Nurunnabi, A., Teferle, F. N., Laefer, D. F., Lindenbergh, R. C., & Hunegnaw, A. (2022). A Two-Step Feature Extraction Algorithm Application to deep learning for point cloud classification. *International Archives of the Photogrammetry, Remote Sensing and Spatial Information Sciences - ISPRS Archives*, *46*(2/W1-2022), 401–408. https://doi.org/10.5194/isprs-archives-XLVI-2-W1-2022-401-2022

Operandum Project. (2022). Open Air Laboratory Scotland. https://geoikp.operandum-project.eu/oal/explorer/scotland

Pauly, M., Gross, M., & Kobbelt, L. P. (2002). Efficient simplification of point-sampled surfaces. *Proceedings of the IEEE Visualization Conference*, 163–170. https://doi.org/10.1109/visual.2002.1183771

Platt, J. C. (1999). Probabilistic Outputs for Support Vector Machines and Comparisons to Regularized Likelihood Methods. *MIT Press*, 61–74.

Polster, D. F. (2003). Soil Bioengineering for Slope Stabilization and Site Restoration.

Riley, S. J., & Degloria, S. D. (1999). *A Terrain Ruggedness Index that Quantifies Topographic Heterogeneity* (tech. rep.). https://www.researchgate.net/publication/259011943

Rózycka, M., Migoń, P., & Michniewicz, A. (2017). Topographic Wetness Index and Terrain Ruggedness Index in geomorphic characterisation of landslide terrains, on examples from the Sudetes, SW Poland. *Zeitschrift fur Geomorphologie*, *61*, 61–80. https://doi.org/10.1127/zfg{_}suppl/2016/0328

Sarkar, S., & Kanungo, D. (2004). *An Integrated Approach for Landslide Susceptibility Mapping Using Remote Sensing and GIS* (tech. rep.). https://doi.org/https://doi.org/10.14358/PERS.70.5.617

Šašak, J., Gallay, M., Kaňuk, J., Hofierka, J., & Minár, J. (2019). Combined use of terrestrial laser scanning and UAV photogrammetry in mapping alpine terrain. *Remote Sensing*, *11*(18). https://doi.org/10.3390/rs11182154

Sidle, R. C., & Bogaard, T. A. (2016). Dynamic earth system and ecological controls of rainfall-initiated landslides. https://doi.org/10.1016/j.earscirev.2016.05.013

Sithole, G., & Vosselman, G. (2004). Experimental comparison of filter algorithms for bare-Earth extraction from airborne laser scanning point clouds. *ISPRS Journal of Photogrammetry and Remote Sensing*, *59*(1-2), 85–101. https://doi.org/10.1016/j.isprsjprs.2004.05.004

Sørensen, R., Zinko, U., & Seibert, J. (2006). *Hydrology and Earth System Sciences Discussions* (tech. rep. No. 1). https://hal.archives-ouvertes.fr/hal-00304825

Soudarissanane, S. (2016). *The geometry of terrestrial laser scanning; identification of errors, modeling and mitigation of scanning geometry*. https://doi.org/https://doi.org/10.4233/uuid:b7ae0bd3-23b8-4a8a-9b7d-5e494ebb54e5

Stal, C., Verbeurgt, J., De Sloover, L., & De Wulf, A. (2021). Assessment of handheld mobile terrestrial laser scanning for estimating tree parameters. *Journal of Forestry Research*, *32*(4), 1503–1513. https://doi.org/10.1007/s11676-020-01214-7

Tardío, G., & Mickovski, S. B. (2016). Implementation of eco-engineering design into existing slope stability design practices. *Ecological Engineering*, *92*, 138–147. https://doi.org/10.1016/j.ecoleng.2016.03.036

Travelletti, J., Delacourt, C., Allemand, P., Malet, J. P., Schmittbuhl, J., Toussaint, R., & Bastard, M. (2012). Correlation of multi-temporal ground-based optical images for landslide monitoring: Application, potential and limitations. *ISPRS Journal of Photogrammetry and Remote Sensing*, *70*, 39–55. https://doi.org/10.1016/j.isprsjprs.2012.03.007

van Natijne, A., Bogaard, T., van Leijen, F., Hanssen, R., & Lindenbergh, R. (2022). World-wide InSAR sensitivity index for landslide deformation tracking. *International Journal of Applied Earth Observation and Geoinformation*, *111*, 102829. https://doi.org/10.1016/j.jag.2022.102829

Weinmann, M., Jutzi, B., Mallet, C., & Weinmann, M. (2017). Geometric Features and Their Relevance for 3D Point Cloud Classification. *ISPRS Annals of the Photogrammetry, Remote Sensing and Spatial Information Sciences*, *4*(1W1), 157–164. https://doi.org/10.5194/isprs-annals-IV-1-W1-157-2017

Winiwarter, L., Anders, K., & Höfle, B. (2021). M3C2-EP: Pushing the limits of 3D topographic point cloud change detection by error propagation. *ISPRS Journal of Photogrammetry and Remote Sensing*, *178*, 240–258. https://doi.org/10.1016/j.isprsjprs.2021.06.011

Wu, Y., & Cheng, H. (2005). Monitoring of gully erosion on the Loess Plateau of China using a global positioning system. *Catena*, *63*(2-3), 154–166. https://doi.org/10.1016/j.catena.2005.06.002

Yang, J., Li, H., & Jia, Y. (2013). Go-ICP: Solving 3D Registration Efficiently and Globally Optimally. *Proceedings of the IEEE International Conference on Computer Vision*, 1457–1464.

Yang, W., Wang, M., & Shi, P. (2013). Using MODIS NDVI Time Series to Identify Geographic Patterns of Landslides in Vegetated Regions. *IEEE Geoscience and Remote Sensing Letters*, *10*(4), 707–710. https://doi.org/10.1109/LGRS.2012.2219576

Yilmaz, I. (2009). GIS based statistical and physical approaches to landslide susceptibility mapping (Sebinkarahisar, Turkey). *Bulletin of Engineering Geology and the Environment*, *68*(4), 459–471. https://doi.org/10.1007/s10064-009-0188-z

Yin, Y., Zheng, W., Liu, Y., Zhang, J., & Li, X. (2010). Integration of GPS with InSAR to monitoring of the Jiaju landslide in Sichuan, China. *Landslides*, *7*(3), 359–365. https://doi.org/10.1007/s10346-010-0225-9

Yong, C., Jinlong, D., Fei, G., Bin, T., Tao, Z., Hao, F., Li, W., & Qinghua, Z. (2022). Review of landslide susceptibility assessment based on knowledge mapping. https://doi.org/10.1007/s00477-021-02165-z

Zhang, W., Qi, J., Wan, P., Wang, H., Xie, D., Wang, X., & Yan, G. (2016). An easy-to-use airborne LiDAR data filtering method based on cloth simulation. *Remote Sensing*, *8*(6). https://doi.org/10.3390/rs8060501

Zhu, T. X. (2012). Gully and tunnel erosion in the hilly Loess Plateau region, China. *Geomorphology*, *153-154*, 144–155. https://doi.org/10.1016/j.geomorph.2012.02.019

Zieher, T., Polderman, A., & Alfieri, S. (2022). *OPEn-air laboRAtories for Nature baseD solUtions to Manage hydro-meteo risks* (tech. rep.).

A

Photographs

The author took photographs during the fieldwork in April 2022. Some of them are included in the main part of this thesis. Additional ones are displayed in this appendix. These photos may help to grasp a better understanding of how the Catterline Bay looks like.

(a) Scan from the parking lot.

(b) Scan on the road

(c) Scan on the southern part of the beach.

(d) Scan on a former sea defence wall.

Figure A.1: Four scanning positions. Photos by the author, April 2022.

(a) View from the lower part of the access road towards the pier.

(b) View from halfway the access road towards the parking lot.

Figure A.2: Two views from the access road. Photos by the author, April 2022.

(a) View from halfway the beach towards the northern part of the bay.

(b) View from halfway the road towards the southern part of the bay.

Figure A.3: Views on the bay from different standing points. Photos by the author, April 2022.

(a) Large part of the vegetation consists of willows.

(b) View on the location of the live ground anchors

(c) Former pumping station.

Figure A.4: Other details from the Catterline Bay. Photos by the author, April 2022.

B

Results from Ground Filtering Methods

B.1. Cloth Simulation Filter

In Figure B.1 the Cloth Simulation Filter (CSF) gives good results from visual inspection. The ground and non-ground is well separated. However, Figure B.2 shows an example why CSF has difficulties with full 3D data, instead of 2.5D airborne laser scanning data. In this section, the outcrop with very steep slopes and overhanging parts is shown. Here, it is not possible to find a suitable cloth to fit with the overhanging outcrop.

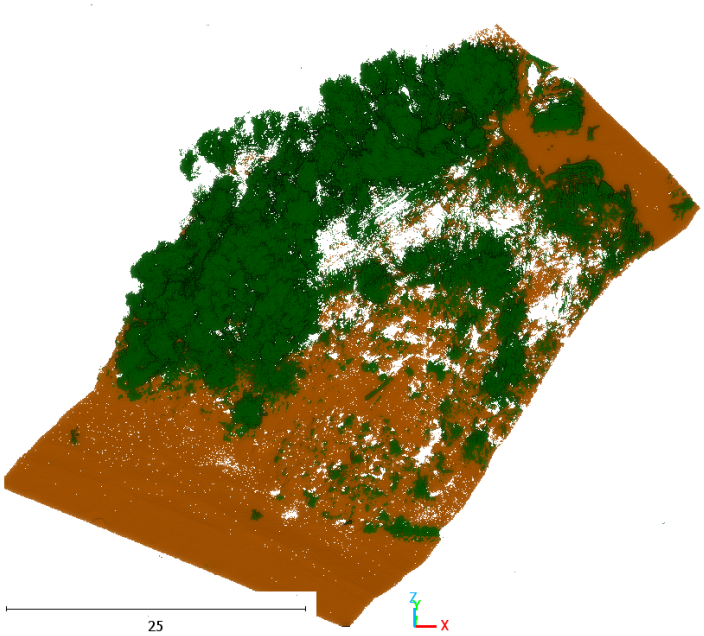

Figure B.1: First section from the results of CSF with the 2022 point cloud

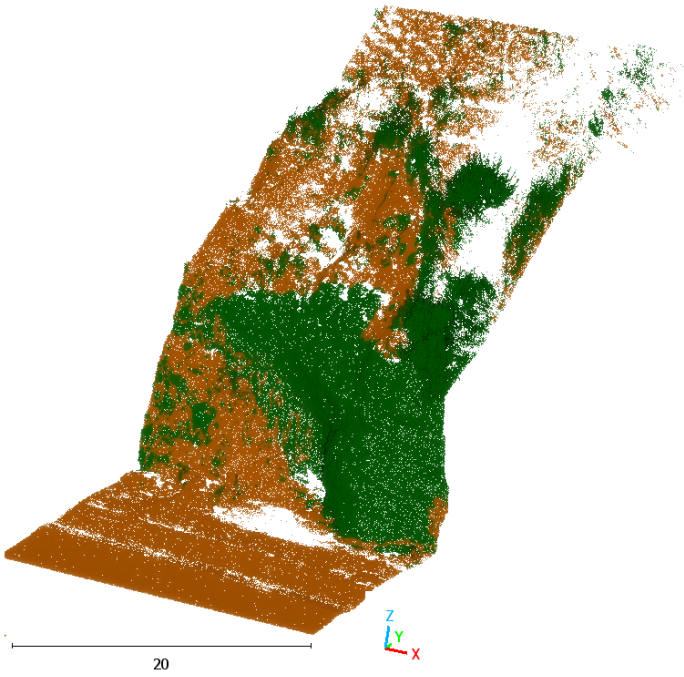

Figure B.2: Second section from the results of CSF with the 2022 point cloud.

B.2. Ray Tracing Voxel Method

Figure B.3 shows a section of filtering ground points with the ray tracing voxel method. Because of the limited laser beam width, the road does not appear in the data as ground or non-ground. In some scans, a voxel containing road points is identified as an end points and in some scans as an intersection voxel. Furthermore, not all points corresponding to vegetation are identified as non-ground points.

Figure B.3: Section from the results of the ray tracing voxel method with the 2022 point cloud.

B.3. Multi-resolution Hierarchical Classification

Figure B.4 shows a section of the point cloud after applying the Multi-resolution Hierarchical Classification (MHC) algorithm. In general, MHC is capable of correctly classifying ground and non-ground points. However, there are some strange lines of triangles, where the points belonging to the ground are not classified as ground points. Figure B.5 shows another section of the point cloud after applying MHC, where MHC is inadequate with handling full 3D data. In this section, the outcrop with very steep slopes and overhanging parts is shown. The interpolation based method has difficulties with these characteristics and classifies the outcrop completely as non-ground.

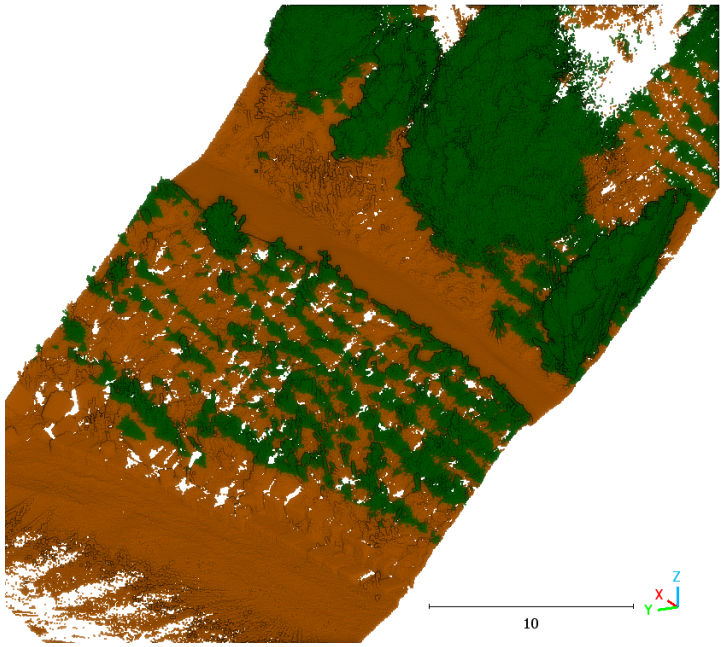

Figure B.4: First section from the MHC result with the 2022 point cloud.

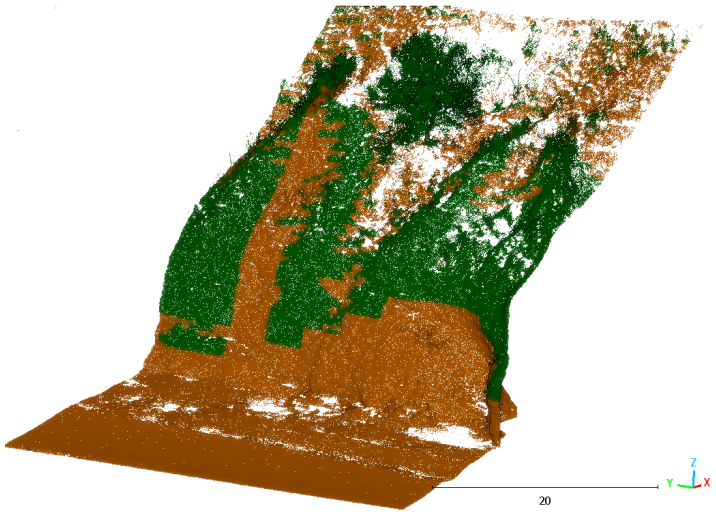

Figure B.5: Second section from the MHC result with the 2022 point cloud.

C

Maps

C.1. Maps 2019

In the main part of this thesis, full maps of the 2022 data are visualised. To give a complete view on the results, this appendix also shows the 2019 maps.

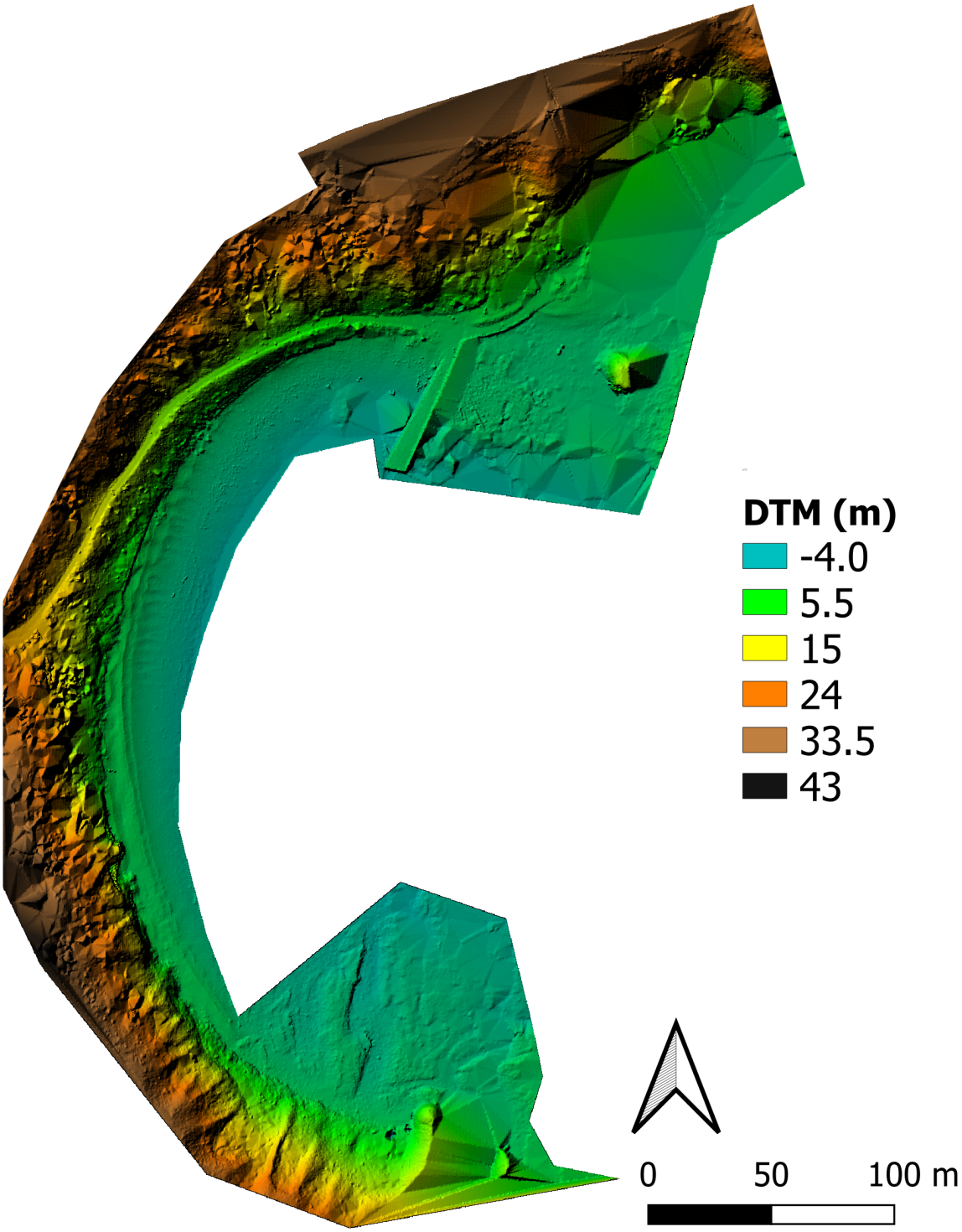

Figure C.1: Digital Terrain Model 2019

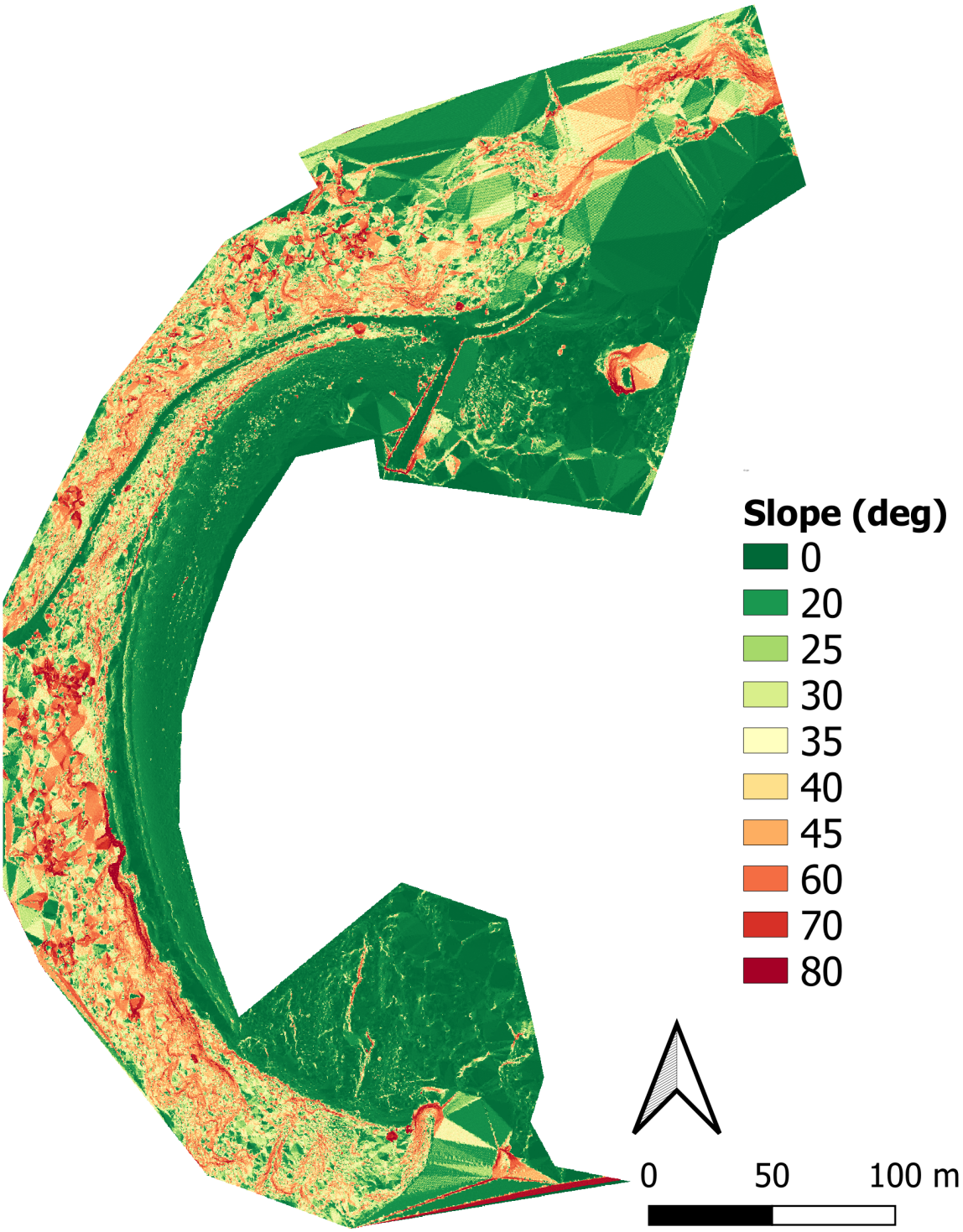

Figure C.2: Slope 2019

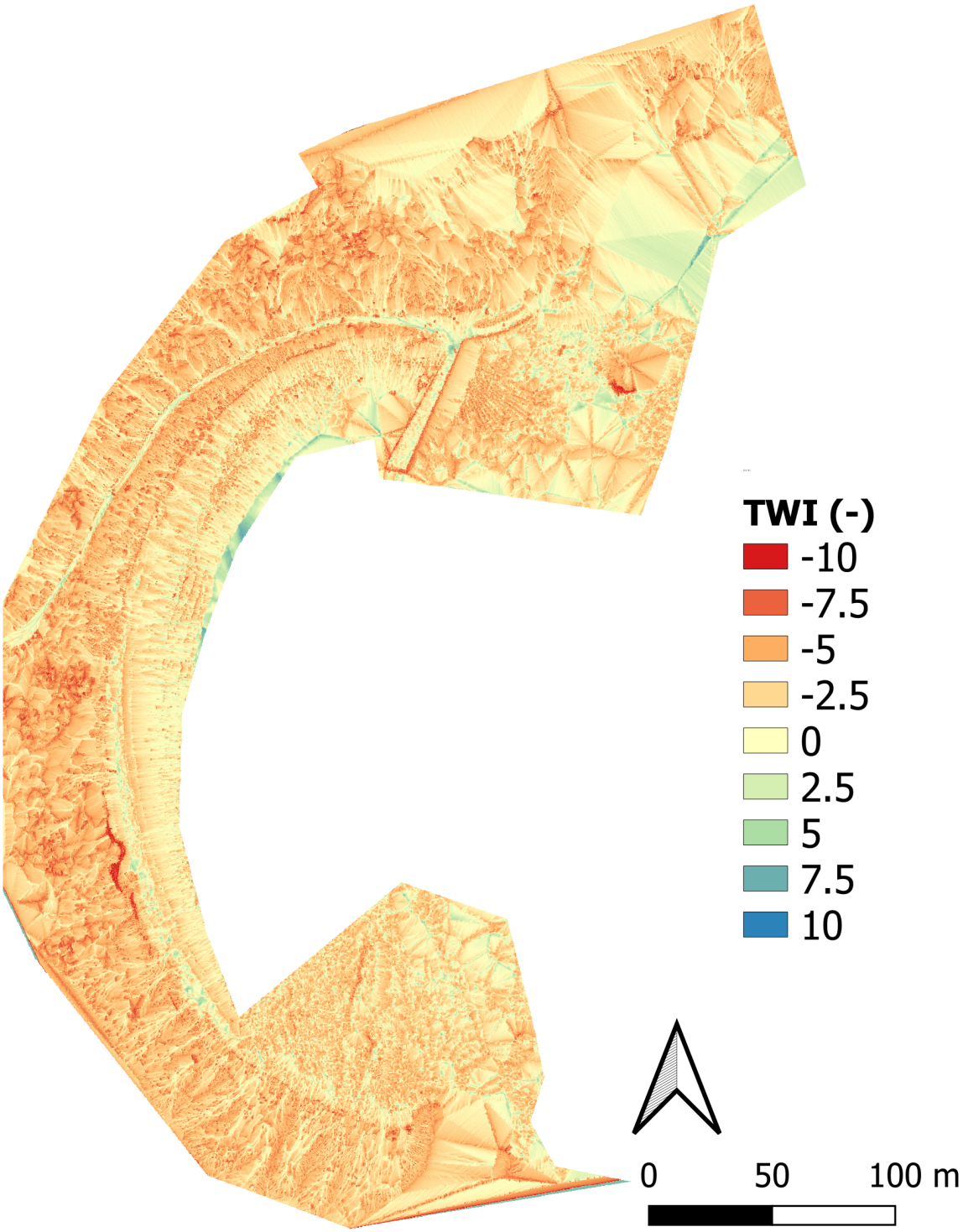

Figure C.3: Topographic Wetness Index 2019

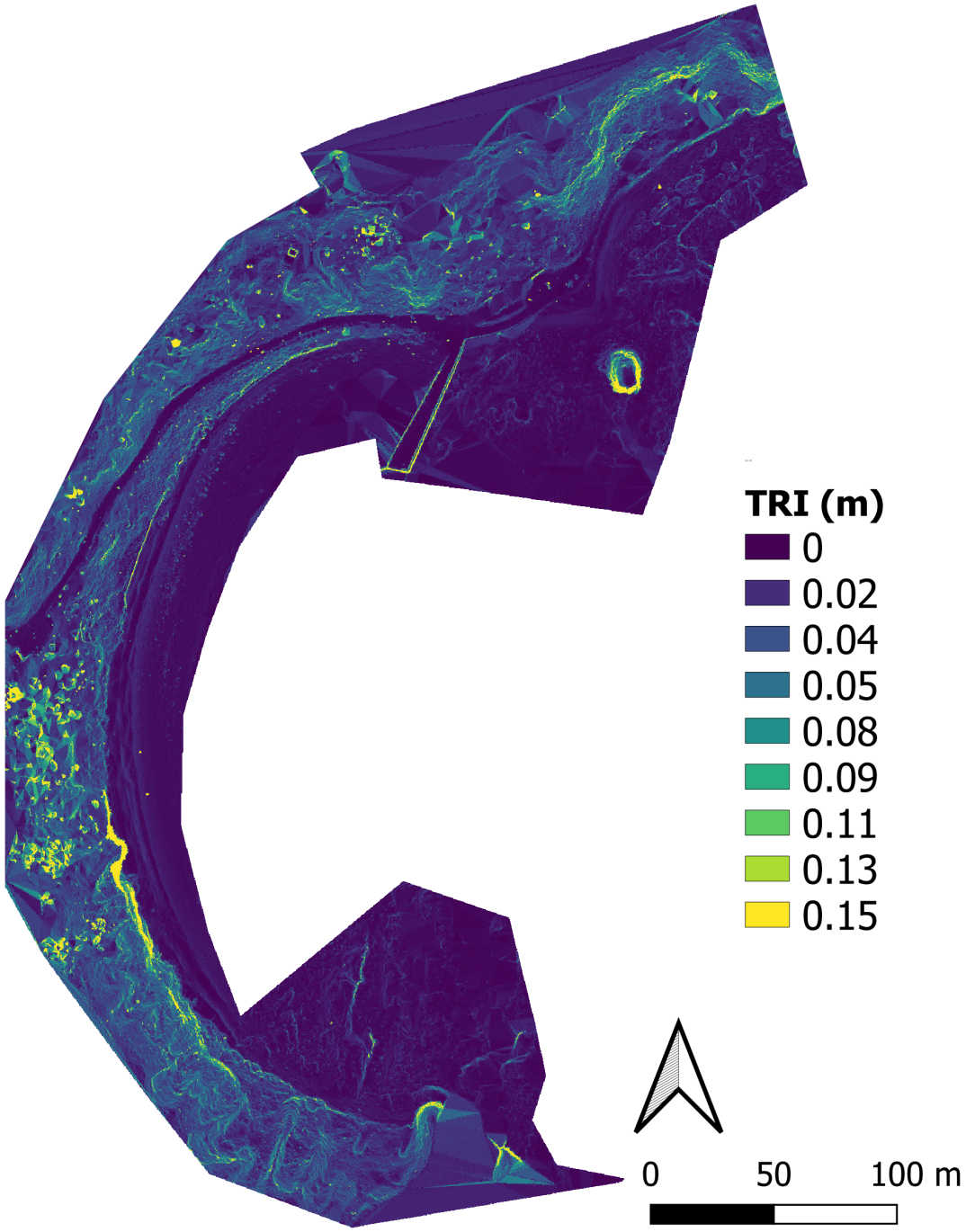

Figure C.4: Terrain Ruggedness Index 2019

C.2. Locations Validation Zones

Figure C.5 shows the validation erosion zones together with the identified erosion zones in this research.

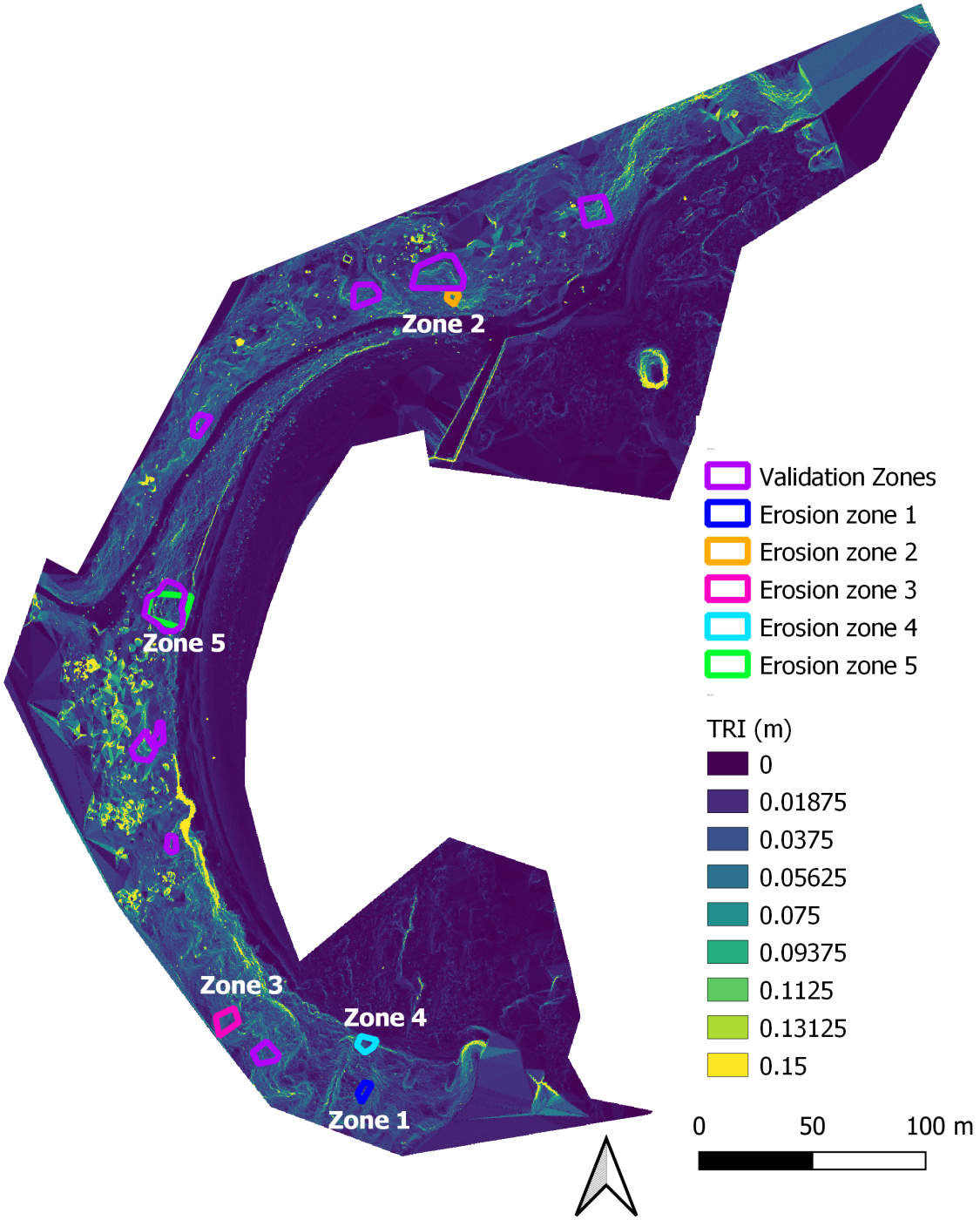

Figure C.5: Map with the identified erosion zones and the validation erosion zones. The Terrain Ruggedness Index of 2022 is also displayed.

D

Statistics of individual erosion zones

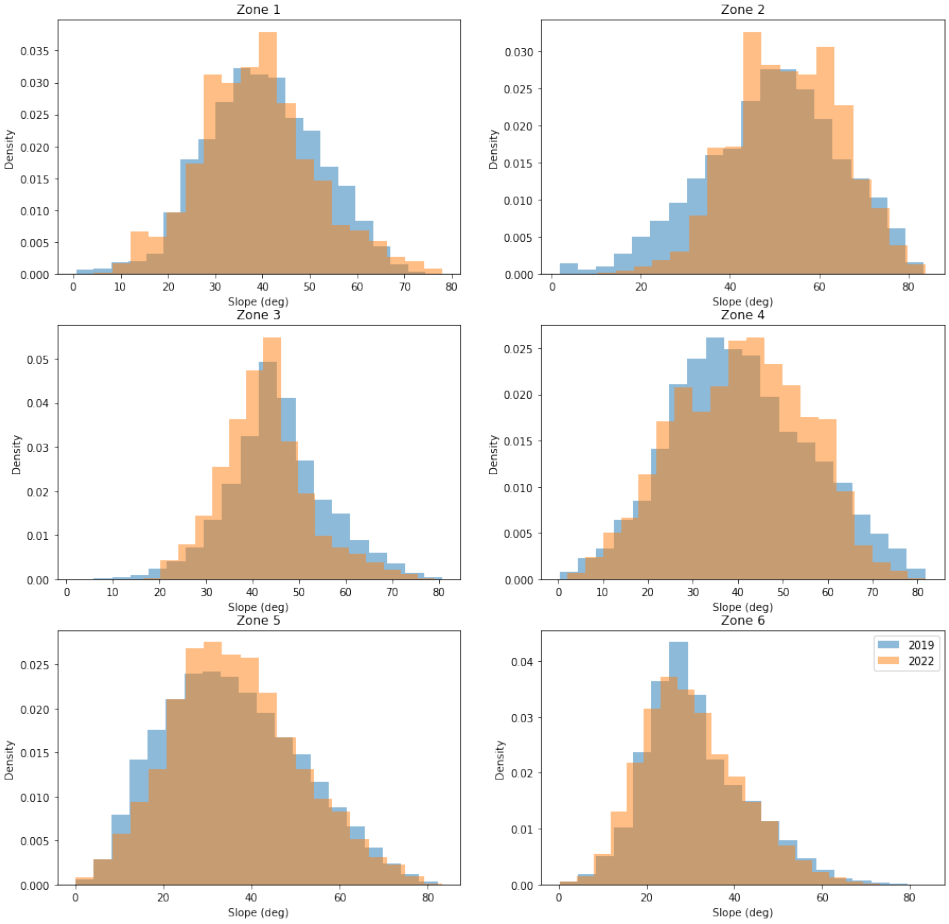

Figure D.1: Histogram of the six zones. Zones 1 to 5 are erosion zones and in zone 6 multiple stable zones are combined.

Table D.1: Statistics for the slope in six zones.

		Mean (deg)	Maximum (deg)	Std (deg)
Zone 1	2019	40.0	74.5	12.0
	2022	38.8	78.0	12.2
Zone 2	2019	49.6	83.5	15.1
	2022	53.0	84.0	12.0
Zone 3	2019	45.5	80.7	10.6
	2022	42.7	79.2	9.4
Zone 4	2019	40.7	81.7	15.4
	2022	40.8	81.9	15.4
Zone 5	2019	35.8	82.2	14.4
	2022	36.4	83.2	17.0
Zone 6	2019	31.3	83.7	11.6
	2022	30.6	77.0	11.4

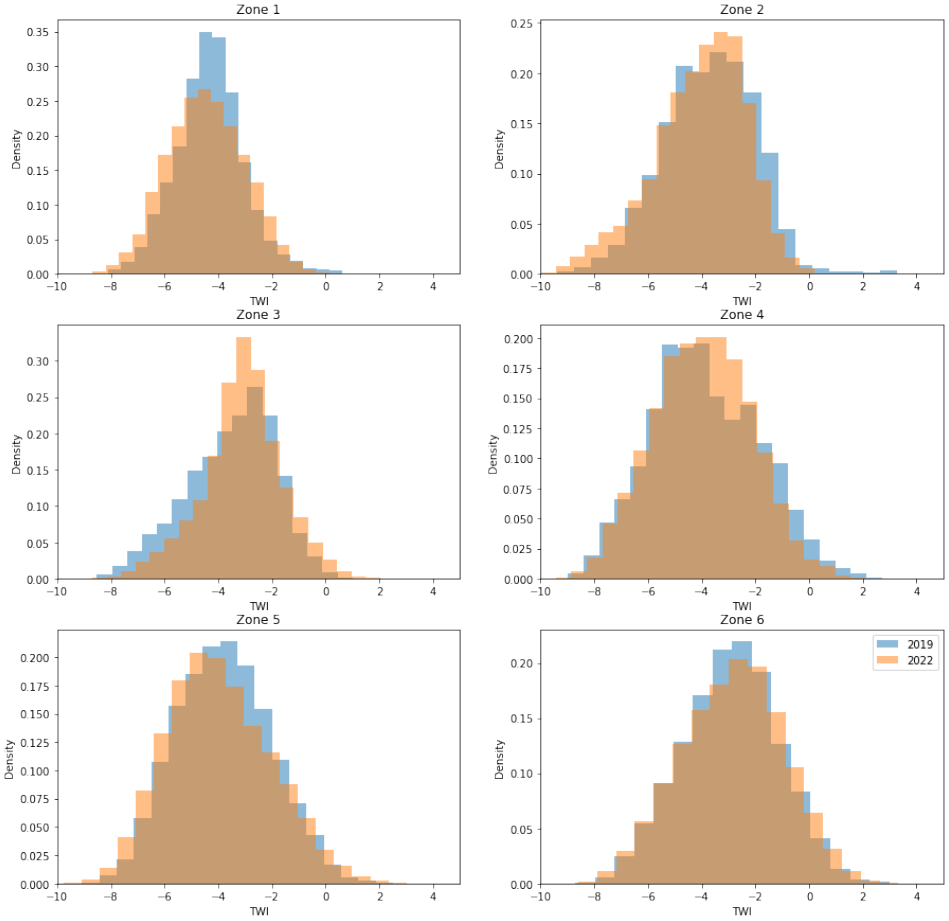

Figure D.2: Histogram of the six zones. Zones 1 to 5 are erosion zones and in zone 6 multiple stable zones are combined.

Table D.2: Statistics for the TWI in six zones.

		Mean (deg)	Maximum (deg)	Std (deg)
Zone 1	2019	-4.30	1.59	1.27
	2022	-4.44	0.61	1.44
Zone 2	2019	-3.73	3.27	1.69
	2022	-4.07	0.71	1.70
Zone 3	2019	-3.52	2.12	1.65
	2022	-3.09	2.04	1.48
Zone 4	2019	-3.87	2.73	2.01
	2022	-3.97	2.13	1.80
Zone 5	2019	-3.80	3.79	1.75
	2022	-3.96	3.68	1.93
Zone 6	2019	-2.93	5.17	1.79
	2022	-2.86	4.72	1.90

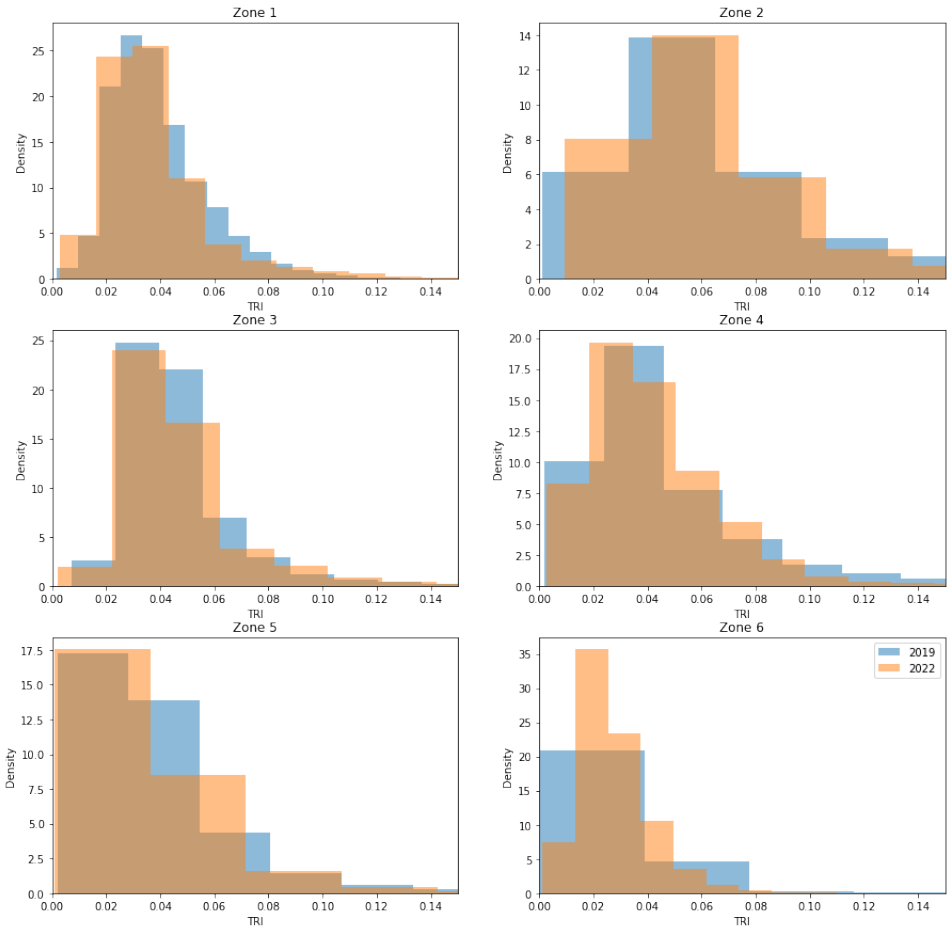

Figure D.3: Histogram of the six zones. Zones 1 to 5 are erosion zones and in zone 6 multiple stable zones are combined

Table D.3: Statistics for the TRI in six zones.

		Mean	Maximum	Std
Zone 1	2019	0.040	0.16	0.018
	2022	0.038	0.27	0.021
Zone 2	2019	0.067	0.64	0.051
	2022	0.066	0.65	0.041
Zone 3	2019	0.046	0.33	0.021
	2022	0.047	0.40	0.022
Zone 4	2019	0.048	0.44	0.038
	2022	0.043	0.32	0.026
Zone 5	2019	0.038	0.53	0.028
	2022	0.037	0.71	0.026
Zone 6	2019	0.029	0.77	0.017
	2022	0.028	0.24	0.013